THE INTERACTION BETWEEN GAS JETS AND THE SURFACES OF LIQUIDS, INCLUDING MOLTEN METALS

A Thesis
presented for the degree of
Doctor of Philosophy
in the
University of London
by
DAVID HERBERT WAKELIN

John Percy Research Group
May 1966

ABSTRACT

The size and shape of the depression, formed in the liquid surface by subsonic jets of air and carbon dioxide impinging on water and mercury, have been measured for ranges of nozzle-water distance from 4.0 to 40cm. and of jet momentum up to 56,000 dynes. Results obtained for the depression dimensions are consistent with previous work. The shape of the depression has been approximated to a paraboloid of revolution, enabling the effect of interfacial tension on the depth of the depression to be estimated.

The magnitude and direction of the velocities in the water bath have been measured using a photographic technique, and the influence of the nozzle-water distance and jet momentum on the circulation pattern has been studied.

Rates of mass transfer of carbon dioxide between the gas and liquid phases have been measured, using a pH technique. Results are compared with theory based on quasi-steady state diffusion in a radial flow model. Measured mass transfer coefficients vary between .003 and .025 cm/sec., and are shown to be dependant on liquid surface velocity. Rates of absorption and desorption are observed to be similar.

An electrochemical meter was used to measure rates of mass transfer of oxygen into molten silver at 1000°C. Measured mass transfer coefficients of .015 to .048 cm/sec. are also dependant on liquid surface velocity.

TABLE OF CONTENTS

1.0 INTRODUCTION

Gas-liquid interactions are of considerable metallurgical interest, with special reference to their application in extractive and refining processes. For example, bubbles play an important role in open hearth steelmaking[1]. Oxygen is supplied to the metal from an oxidising flame, via the slag layer, and reacts with carbon to produce carbon monoxide bubbles at favoured nucleation sites, when a sufficient gas over-pressure is reached. The stirring of the bath is largely due to the rising bubbles. Vacuum de-gassing and the purging of hydrogen from aluminium or steel by argon are further examples of the importance of bubbles. Experimental investigations have covered bubble shapes, their velocity of rise and rates of mass transfer to the surrounding liquid.

Metallurgical interest in the action of gas jets on liquid surfaces is of more recent origin, stimulated mainly by the development of oxygen steelmaking, in which a supersonic jet of oxygen is blown on to the surface of the steel bath. Compared with the open-hearth process, this leads to vastly increased rates of transfer of carbon, silicon, manganese etc. from the pig iron. The fluid dynamics in the bath are considerably altered. Prior to the carbon boil, the jet promotes agitation of the metal, and hence rapid diffusion of the oxygen to the nucleation sites on the refractories and unmelted scrap. Droplets thrown out of the surface may be entrained into the gas jet. In some processes, for example the LDAC and OLP, material such as powdered lime is introduced into the jet and is blown directly into the bath.

Other applications of jetting gases on to liquid metal surfaces include the jet degassing of molten steel to remove undesirable dissolved gases, present in atomic form. An inert gas, such as argon, is blown under closely controlled conditions to sweep the slag layer away from the impingement area, without causing intermixing of slag and metal. Elements such as hydrogen and oxygen are removed from the steel by the argon at the impingement interface.

The rate of transfer of gas to metal at the cathode during consumable electrode welding is also of interest.[2] The absorption of hydrogen by copper in such a system can cause marked decreases in the density of the weld metal.

1.1 The Investigation

In view of the industrial importance of the interaction of gas jets and the surfaces of liquid metals, the influence of the jet parameters on the size and shape of the depression formed in the liquid, on the bath circulation, and on the rate of transfer of gas to the liquid, has been studied. As there is only a limited amount of information available in the literature on this type of system, especially on mass transfer rates, the investigation has been confined to relatively simple systems.

A circular convergent nozzle was employed, the jet being subsonic throughout. Only one diameter was used, as the jet momentum was the major jet variable. The lance could be moved vertically along the centre axis of the circular tank containing the liquid, and the gas jet impinged normally on the liquid surface. The general system is shown in Figure 1.1-1.

The characteristics of the nozzle and free jet were first determined, notably the coefficient of discharge of the nozzle and the velocity decay of the jet.

a) Room Temperature Systems

The dimensions of the depression, formed in water by air and CO_2 jets, were measured visually over wide ranges of jet momentum and nozzle-water distance. The shape of the depression was also investigated, to enable surface areas to be calculated for later mass transfer work.

The dimensions of the depression were also measured, in P.V.A.and mercury, visually for a 40 centipoise aqueous solution of P.V.A., and using an electrical probe in mercury.

Using a photographic technique, the velocities and flow pattern in the water bath were determined for a range of jet momentum and nozzle-water distance.

Mass transfer work was carried out with a CO_2 jet impinging on tap water. .The concentration of dissolved CO_2 was determined by pH measurement, having first made a calibration for pH versus CO_2 partial pressure and solution temperature. The relative contributions of mass transfer to the depression and to the remaining surface were studied, by varying the total surface area for transfer. Measured mass transfer coefficients were compared with those predicted by a mathematical model of the system (Chap. 3). By controlling the gas supply temperature, the jet was adjusted to the same temperature as the liquid.

b) High Temperature System

Rates of transfer from an oxygen jet to molten silver at 1000°C were investigated, using an electrochemical technique to continuously determine the oxygen pressure in the silver. Mass transfer coefficients obtained for this system were compared with those from the room temperature work. The jet temperature was again adjusted to be approximately the same as that of the liquid bath.

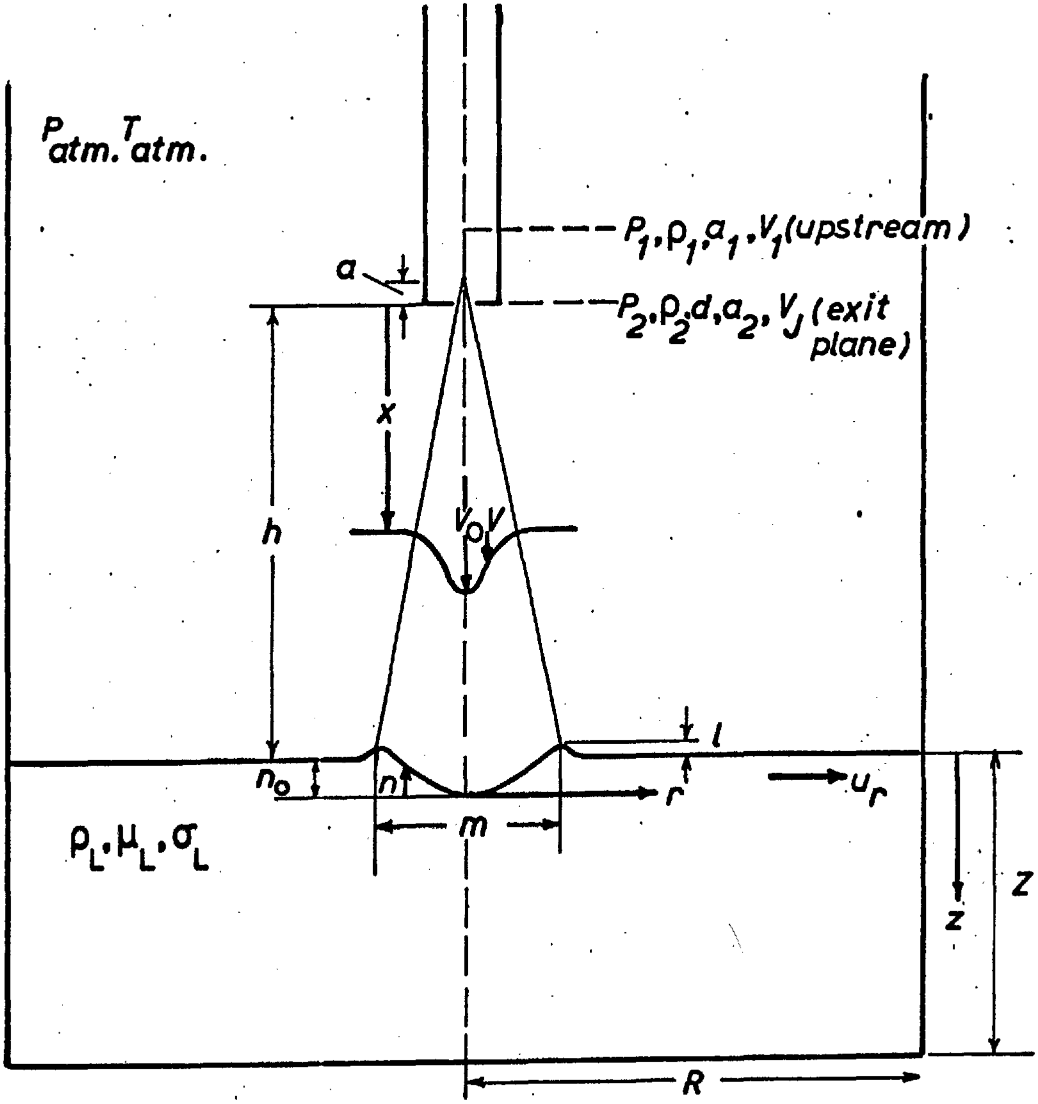

FIG.1.1–1 GENERAL SYSTEM SHOWING SYMBOLS USED

2.0 PREVIOUS WORK

2.1 Oxygen Steelmaking Process.

At steelmaking temperatures, chemical rate control of the decarburization reaction is unlikely in the open hearth process. In this system, the rate controlling steps may be diffusion of carbon and oxygen atoms through the metal as suggested by Darken[3], or of O_2, CO_2 or H_2O through air above the slag surface. From experiments, Larsen and Sordahl[4] found that by displacing the air above the slag by a stream of oxygen a ten times increase in the rate of carbon boil was produced. ..

In comparison the agitation of the bath in the top-blown oxygen process is much more vigorous, and transport of oxygen may no longer be rate limiting. Also, unlike the open-hearth, dephosphorisation may not occur until after the carbon boil has begun. This was pointed out by Kootz[5], who related it to the effect of the jet. When there is deep jet penetration into the metal, reactions proceed much as in the basic Bessemer, but for non-penetration of the jet into the metal, the conditions resemble the open hearth. Kootz and Neuhaus[6] have postulated that decarburisation and dephosphorisation occur in separate reaction zones. This may explain the non interference of the decarburisation reaction with other refining reactions. From laboratory scale experiments KunLi, Dukelow and Smith[7] interpreted their result that overall oxygen efficiency was within the range of commercial oxygen efficiency for decarburisation, as indicating that the oxygen transfer is primarily controlled by the de - carburisation reaction. In further work[8] they showed that unless the jet penetrated through the slag, large oxygen concentrations could be built up in the slag, and decarburisation retarded. When the carbon boil finally began, and mixing of the metal and slag by CO bubbles occurred, the reaction was extremely violent. With jet penetration into the metal the carbon boil occurred sooner and was more uniform.

Besides the stirring action of the jet on the bath, under some conditions droplets are torn out of the metal surface and pass through the oxidising gas phase. The bursting of CO bubbles at the surface may also cause droplet formation. As pointed out by Kootz[5], these droplets provide an additional means of oxygen transfer to the bath, as well as the direct transfer across the impingement area. However, Holden and Hogg[9] have suggested that if the turbulence within the bath is sufficient to bring fresh unoxidised metal continuously to the impingement surface, then the bath has by far the greater potential absorbing capacity.

Szekely[10] has suggested that, for the LD, in view of the larger rate of oxygen transfer into metal required for carbon removal, as compared with the rate required for silicon and manganese removal, a region of high oxygen concentration exists in the vicinity of the slag metal interface. Bubbles of CO travelling through this region may act as a sink for oxygen, and steepen the oxygen concentration ~~oxygen~~ gradient, therefore increasing the net rate of oxygen transfer from the slag to metal.

2.2 Model Studies.

From the preceeding section it can be seen that the oxygen steelmaking process is extremely complex. Although the precise mechanism of overall oxygen transfer into the metal has not been fully resolved, it is obvious that the mode of deformation of the surface by the oxygen jet, the circulation imparted to the bath, and the formation of droplets are of great importance.

Owing to the difficulty of making accurate measurements on a full scale converter vessels most of the work related directly to steelmaking has been carried out on models. The problems involved in establishing precise similarity have been dealt with by Holmes and Thring[11]. They suggested the use of a modified Froude number $\left(\rho_g/\rho_L\right)\left(V_J^2/d_g\right)$ for the impinging jet. Holden and Hogg[9] stated that complete similarity was impossible. However, in order to make quantitative measurements on the interaction of a gas jet and a liquid surface it is not necessary to have similarity with a steelmaking vessel.

a) Circulation of Bath

Qualitative measurements on the gas flow and liquid circulation have been made by Hasimoto[12,13], using a submerged water jet impinging on to mercury. He noted changes in liquid flow patterns with angle of inclination of the lance, as did Holden and Hogg[9], using air impinging on water. The latter also studied the effects of a lighter phase on the water surface to simulate a slag layer, and of immersing the lance below the water surface, both of which caused some downward water flow in the vicinity of the lance.

Further studies of the circulation induced in the liquid bath include those by Maatsch[14], Baptizmanskii[15] and Mathieu[16]. The first two investigators showed that the liquid upflow under the area of impingement caused by the drag of non-absorbed gas departing from the cavity could be reversed by a highly absorbed gas, such as ammonia in water. Mathieu measured the average period of rotation T of particles in a water bath stirred by an air jet. He found T decreased for increasing values of $V_J^2/2gd$ and that for a constant value of this parameter there was a minimum in the value of T as h/d increased. He also showed that the injection into the bath of particles carried in the air jet tended to cause reversed bath circulation.

b) Splashing

Chedaille and Horvais[17] conducted experiments blowing air on to water. They measured the quantity of liquid splashed out of the container. For a given lance height they reported an increase in liquid splashed out, for increasing gas flow rate up to a certain point. For further increase in flow rate, the quantity splashed out decreased. The position of the maximum moved progressively to higher values of gas flow rate for increasing lance heights. However, further analysis of their blowing rate and lance height, using the relation between these factors and jet penetration developed by Banks[18], indicates that the depth of depression was of the order of the bath depth at the conditions of the maximum. The authors in fact show a dependence of splashing on the depth of the bath.

Kun Li[19] made a qualitative study of splashing with air impinging on fluidised baths. He found that the presence of a foam layer on the surface reduced splashing considerable. In this context Kluth and Maatsch[20] have shown that if the lance is immersed in a foam layer on the water surface, it acts as a pump and circulates the foam.

c) Mass Transfer

Only a few model investigations into mass transfer have been carried out. van Langen[21] qualitatively investigated the effect of lance slant angle, and hence change in circulation pattern, on a 1/26 scale model of an LD converter. The absorption of dry HCl gas blown onto saturated $NaHCO_3$ solution covered by paraffin oil, was followed using methyl orange indicator. Stirring was improved by decreasing the oil thickness, the bath depth, or the lance height, or by increasing the jet momentum.

Dubrawka[22] studied the absorption of CO_2 blown at 1 cfm through an 1/8" nozzle into a bath of sodium hydroxide for 2 minutes. He found that percentage absorption increased for increasing bath diameter up to 15 in.and for increasing bath depth up to 4 in., for a bath diameter of 5½ in. For increasing lance height he found a maximum at 1", beyond which percentage absorption again decreased.

Hoyle[23] measured rates of hydrogen desorption from EN 24 steel by jet degassing with argon. Results were treated by assuming the partial pressure of hydrogen in the gas phase above the interface to be in equilibrium with the partial pressure of hydrogen in the metal. Quantities of argon required to degas from .10 ml/g. to.02ml./g. predicted in this manner were approximately 10 times too low. An alternative approach to these results is presented in Chap. 6.

2.3 The Free Turbulent Circular Jet

For a subsonic jet issuing from a nozzle into a fluid of similar density, spreading of the jet occurs by shearing at its boundaries, where otherwise a large velocity discontinuity would exist. A lateral mixing process occurs and the jet spreads. The energy of the jet decreases with distance from the nozzle, as does its velocity. A zone of establishment of flow exists before velocity profiles across the jet become similar for succeeding downstream planes. Numerous investigators[24,25,26] have experimentally measured the decay of the centre line velocity and the velocity distribution across a plane. The most common formulae used to describe the results are:

$$V_o/V_J = K\, d/x \qquad \ldots\ 2.3\text{-}1$$

with values of K from 6.2 (Albertson[24]) to 7.7 (Poreh & Cermak[26] - water jet) and
$$\frac{V}{V_o} = \exp\left\{-2K^2\left(\frac{r}{x}\right)^2\right\} \ldots\ 2.3\text{-}2$$

Combination of the two equations satisfies the conservation of momentum. The latter equation, however, predicts V approaches zero as r approaches infinity, i.e. it does not fix the jet boundary.

Albertson et al[24] measured jet velocities over large distances of x/d, up to 250, and found good agreement with Equation 2.3-1 after the potential core had been passed. In their results, they assumed the vertex of the diffusion cone to lie in plane of the orifice. This is not necessarily so, as pointed out by Citrini[27], who also found that the decay of the centre line velocity is described by the empirical equation $V_o/V_J = 6.6\, d/x - 0.49$ for $x < 40d$. In his treatment of the subject, Hinze[28] suggested that distances from the nozzle should be measured from the geometric origin of the jet.

The variation of K with nozzle Reynolds number has been investigated by Baines[29]. He found the K decreased from 6.8 at $R_e = 7\text{x}10^4$ down to 5.7 at $R_e = 2.1\text{x}10^4$. His results only extend to values of $^x/d$ of up to 60. Above $^x/d = 30$ his results at high R_e tend to converge towards the values at lower R_e, but no mention of this is made in the text. Ricou and Spalding[30] used a different technique to measure the jet constants. As they pointed out, the use of a pitot tube to determine velocity profiles becomes inaccurate for small velocities at large values of x. Instead they measured mass entrainment rates into the jet, and extended their measurements to $^x/d$ equal to 400. They obtained a value of K of 6.25 for R_e greater than $3x10^4$. They noted an increase in the entrainment rate, i.e. a decrease in K, for lower Reynolds numbers, down to K = 5.0 for $R_e = 5x10^3$. They discussed the effect of gas buoyancy which is also dealt with by Bosanquet et al[31] and Abraham[32].

Maatsch[33] has investigated the velocity profiles for sonic flow through Laval nozzles, and has concluded that the decay of centre line velocity is not dependant on the upstream pressure or shape of the nozzle.

2.4 Impingement of Jets on Surfaces

a) Solid Surfaces.

Measurements around the stagnation point of a normally impinging jet on a flat surface, the pressure distribution on the surface, and the velocity profiles in the resulting radial wall jet have been made by Poreh and Cermak[26] (on a submerged water jet), and Bradshaw and Love[34] on an air jet. Poreh and

Cermak concluded that in the neighbourhood of the stagnation point, flow was irrotational, and the pressure distribution on the boundary was given by

$$\frac{P}{\frac{\dot{M}}{\rho . g . h^2}} = 38.5 - 4800 \left(\frac{r}{h}\right)^2$$

where P is the additional pressure head. Banks[18] has suggested that the equation

$$\frac{P}{\frac{38.5\dot{M}}{\rho g h^2}} = \exp \left\{ - \frac{4800}{38.5} \left(\frac{r}{h}\right)^2 \right\}$$

fits their results over a much wider range. The static pressure contours measured by Bradshaw and Love fit a very similar notmal error curve.

An investigation of the heat transfer coefficient to a solid surface at the centre line of an impinging jet has been conducted by Huang[35], who proposed empirical relations of the form

$$Nu = .02\, R_e^{0.87}\, Pr^{0.33}$$

b) Liquid Surfaces

One of the first experimental investigations of the penetration of a gas jet into a liquid was that of Segawa et al[36] who blew an air jet onto water in a 1/10 scale model of a 5 ton LD. Their depth of depression results showed a large scatter but followed approximately the relationship

$$V_J \propto \sqrt{n_o}\, (h+n_o)\, d$$

i.e. $n_o \propto \frac{\dot{M}}{(n_o+h)^2}$

Baptizmanskii[15] has developed an empirical relation between blowing pressure P and depth of penetration for a non-absorbed gas of the form:

$$n_o = \frac{P^{0.5}\, d^{0.6}}{\rho_L^{\;0.4}}$$

Further investigators have used dimensional analysis to determine the more important controlling parameters. Mathieu[37] chose as his main groups n_o/d, h/d and $V_J^2/2gd$. He investigated subsonic air jets impinging on to water, and the relation between these parameters. He noted the phenomena of formation of intumescences at low blowing rates and small nozzle heights, and of bath rotation at large nozzle heights. This latter effect was directly related to the small size of vessel used. He also noted the decrease in depression depth at which splashing began, with increase in nozzle height. Later work[16] extended the investigation to higher viscosity oils (up to 770 centistokes) but no significant change in depression depth occurred.

Collins and Lubanska[38] also used dimensional analysis to determine the controlling parameters. They took the maximum depth n_o as the principal criterion. Their results yielded

$$n_o = 53\dot{M}/\left(\rho_L g h^2 + 19(\rho_L g \dot{M}^2)^{1/3}\right)$$

for normal impingement of an air jet on water.

Other investigators have sought solutions relating the jet momentum to the weight of displaced liquid. Amongst these were Maatsch[39] who blew CO_2 on to molten tin and on to a bath of oil. He found for vertical impingement that the volume of the depression was equal to $1.3\ \dot{M}/\rho_L g$.

Denis[40] made measurements on supersonic flow from Laval nozzles impinging on a variety of liquids, ranging from water to mercury. He related the volume of displaced liquid to the jet momentum and found it equal to up to $1.4\ \dot{M}/\rho_L g$. It must be noted that in these experiments jet momentum was measured by impingement on a balance, a technique subject to some error, as discussed in section 4.3.. Denis approximated the shape of the depression to a spherical bottom and the trunk of a cone. Comparison of stagnation velocity from the observed depth of depression agreed well with the velocity of a free jet having travelled a similar distance from the nozzle.

van der Lingen[41] has recently studied the impingement of inclined air jets onto the surface of water and mercury. His treatment neglects the reaction of the jet fluid leaving the liquid. However, for cavities which have a depth comparable to their diameters, the reversal of gas flow must exert an additional force on the surface, especially for inclined jets. This fact is brought out by the work of Maatsch and Denis noted above.

More reliable results can be obtained by considering the forces acting at the stagnation point. This is the basis of the work of Banks and Chandrasekhara[18], whose results for air impinging on water agree well with stagnation pressure analysis and show

$$n_o = \frac{125}{\pi} \frac{\dot{M}}{\rho_L g(h+n_o)^2}$$

The agreement is further improved by taking interfacial surface tension into account. To present their experimental results, however, the graph of n_o/h versus $\dot{M}/\rho_L g n_o^3$ was chosen, a method which conceals slight trends away from the given equation. Banks also analysed his results by equating the change in jet momentum to the weight of displaced liquid. He assumed a normal error curve for the shape of the depression, which leads to the result that the depression profile follows the velocity profile in the jet. Later extension of the work[42] showed the analysis could describe the case of an oil jet impinging on water, and of a water jet impinging on carbon tetrachloride, provided that interfacial tension was taken into account.

Olmstead and Raynor[43] have made an analytical solution of the plane free-streamline jet impinging on a deformable surface, which predicted the formation of a lip around the edge of the cavity. It also showed some agreement at low jet velocities and large nozzle heights, with the results of Banks for the diameter of the cavity. The increase in cavity depth and width with increasing jet velocity, as observed in practice, can also be predicted from this treatment.

3.0 THEORETICAL TREATMENT OF MASS TRANSFER

For the transfer of a species "a" in a two phase system from an interface into a liquid phase, a mass transfer coefficient may be defined as:

$$\dot{n}_a = k_L A (C_a^{iL} - C_a^{bL}) \quad .... \ 3.0\text{-}1$$

where $\dot{n}_a$ = rate of mass transfer of species "a" (moles/sec.).

A = area of contact of interface (cm^2).

C_a = concentration of species "a" ($moles/cm^3$).

L , liquid phase; i, interface; b, bulk.

k_L = interface liquid side mass transfer coefficient.

Similarly, for transfer to an interface from a gaseous phase

$$\dot{n}_a = k_g A (C_a^{bg} - C_a^{ig})$$

where k_g = interface gas side mass transfer coefficient.

g, gaseous phase.

In simple solutions, if equilibrium conditions exist at the interface then the partition coefficient m_e is defined as:

$$m_e = \left(\frac{C_a^{iL}}{C_a^{ig}} \right)_{\text{equilibrium}}$$

The two interface coefficients may be combined, to enable the rate of mass transfer to be related to the bulk concentration in either phase:

$$\dot{n}_a = k_o A (m_e C_a^{bg} - C_a^{bL}) \quad .... \ 3.0\text{-}2$$

where the overall coefficient $k_o = \dfrac{1}{(1/k_L)+(m_e/kg)}$

The case of non-equilibrium conditions at the interface when a single molecule a* in the gaseous phase reacts to produce a single molecule a in the liquid phase, may be treated[44] by considering the forward and backward surface reaction rate constants k_f^* and k_b^* (cm/sec). Equation 3.0-2 then becomes:

$$\dot{n}_a = \frac{1}{(1/k_L + k^*_b/k^*_f \cdot k_g + 1/k^*_f)} \cdot A \cdot \left(\frac{k_b^*}{k_f^*} C_{a^*}^{bg} - C_a^{bL} \right)$$

3.1 Previous Models

i). Two-film theory.

For two phases in contact, Whitman[45,46] assumed the existence of a film on either side of the interface. The concentration gradients are contained in these boundary films, beyond which each fluid has uniform bulk properties. Transfer across the interface is by diffusion only. Quasi-steady state conditions are assumed, neglecting concentration changes within the films. This approach leads to equations of the form:

$$\dot{n}_a = \frac{D_L}{\delta_L} A \left(C_a^{iL} - C_a^{bL}\right)$$

where D_L = Diffusion coefficient of species "a" in the liquid phase (cm^2/sec).

δ_L = film thickness (cm.)

However, it has shown subsequently that δ_L is not independant of D_L, and the equation is more conveniently written as 3.0-1.

ii). Penetration Theories.

The theory originally developed by Higbie[47] for transfer in wetted wall columns, considered unsteady state diffusion into a non-turbulent semi-infinite liquid. The theory, based on Fick's law of unsteady state diffusion, may be expressed in one dimension by the equation:

$$\frac{\partial C_a}{\partial t} = - \frac{D \partial^2 C_a}{\partial x^2}$$

The solution of this equation leads to a mass transfer coefficient of the form in Equation 3.0-1.

with $$k_L = \left(\frac{2 D_L}{\pi t_e} \right)^{1/2}$$

where t_e = time of exposure at the interface.

For transfer in turbulently mixed systems, Danckwerts[48] adapted the Higbie model by considering elements of fluid swept randomly to the surface as eddies. While the element of fluid remains at the surface, concentration gradients develop by unsteady state transfer. Subsequently the element is swept back to the bulk of the fluid, where the concentration gradients are destroyed. This theory leads to a mass transfer coefficient of the form:

$$k_L = (D_L . S)^{1/2}$$

where S = mean rate of surface renewal.

3.2 Present Model for Radial Flow System

The system consists of liquid flowing radially from a vertical axial source, with transfer occuring across the gas-liquid interface.

Let the concentration of species "a" at point (r,z) be C. Mass flux of species "a" into liquid at interface

$$\dot{n}_a = \int_0^{r_1} 2\pi r \left(D. \frac{dC}{dz} \right)_{z=o} dr \quad .... \; 3.2\text{-}1$$

In order to evaluate this flux, the term D $(dC/dz)_{z=o}$ must be evaluated in terms of r. Neglecting any variation of D with r or z, consider an element a distance r from the vertical axis, depth z below the interface:

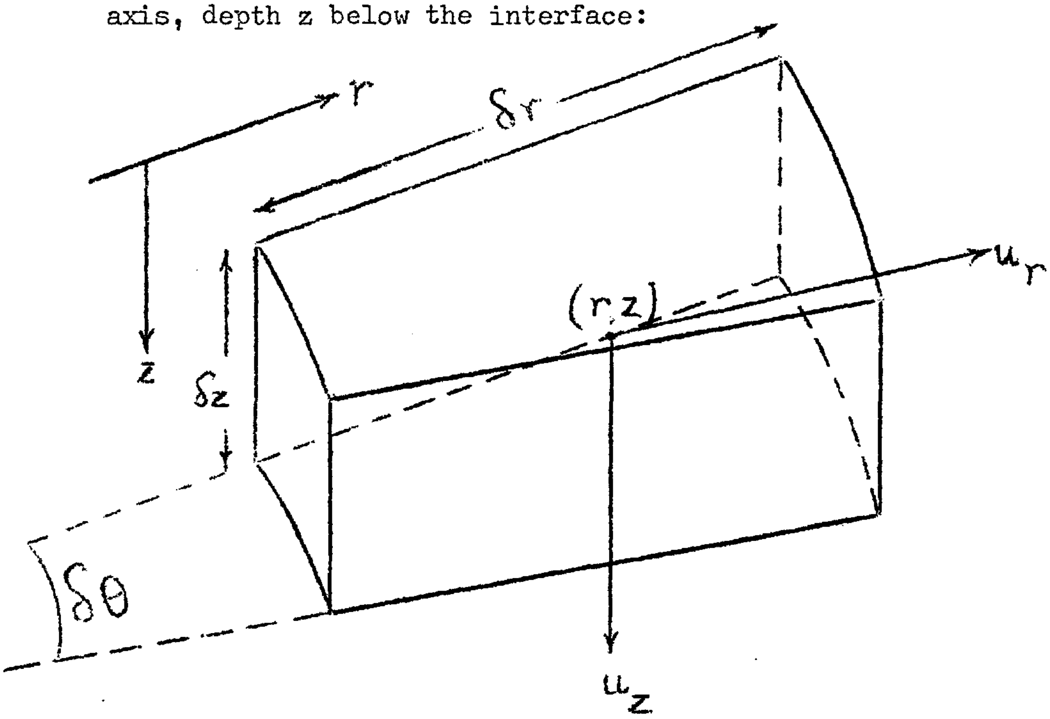

Flux of species "a" out of element:

i). by diffusion $-\left(\frac{D\,\partial C}{\partial z}\right)_{z+\frac{\delta z}{2}} \cdot r.\delta\theta.\delta r$

ii). by convection in r direction $+\left(u_r.C\right)_{r+\frac{\delta r}{2}} \cdot\left(r+\frac{\delta r}{2}\right).\delta\theta.\delta z$

iii). by convection in z direction $+\left(u_z.C\right)_{z+\frac{\delta z}{2}} .r.\delta\theta.\delta r$

Flux of species "a" in to element:

i). by diffusion $-\left(\frac{D\,\partial C}{\partial z}\right)_{z-\frac{\delta z}{2}} .r.\delta\theta.\delta r$

ii). by convection in r direction $+\left(u_r.C\right)_{r-\frac{\delta r}{2}} \cdot\left(r-\frac{\delta r}{2}\right).\delta\theta.\delta z$

iii). by convection in z direction $+\left(u_z.C\right)_{z-\frac{\delta z}{2}} \cdot r.\delta\theta.\delta r$

Assuming quasi-steady state conditions, there will be no net accumulation of species "a" in the element during the time period considered. Hence:

$$-\frac{\partial}{\partial z}\left(\frac{D\,\partial C}{\partial z}\right).\delta z.r.\delta\theta.\delta r+\frac{\partial}{\partial r}(u_r.C.r).\delta r.\delta\theta.\delta z+\frac{\partial}{\partial z}(u_z.C).\delta z.r.\delta\theta.\delta r=0$$

Assuming D to be independant of concentration:

$$-D.\frac{\partial^2 C}{\partial z^2}+\frac{C}{r}.\frac{\partial}{\partial r}(u_r.r)+\frac{(u_r.r)}{r}\frac{\partial C}{\partial r}+u_z\frac{\partial C}{\partial z}+C.\frac{\partial u_z}{\partial z}=0 \quad \ldots.\ 3.2\text{-}1$$

If mass flux of species "a" is small compared with bulk mass flux

$$\frac{1}{r}\frac{\partial}{\partial r}(u_r.r)+\frac{\partial u_z}{\partial z}=0 \quad \ldots.\ 3.2\text{-}2$$

$$\therefore \quad - \frac{D\,\partial^2 C}{\partial z^2} + \frac{(u_r . r)}{r} \cdot \frac{\partial C}{\partial r} + u_z . \frac{\partial C}{\partial z} = 0 \quad \ldots\ldots 3.2\text{-}3$$

Define $C^* = \dfrac{C^i - C}{C^i - C^b}$

The boundary conditions for the system are:

$r > 0, \quad z = 0, \quad C^* = 0$

$r > 0, \quad z = \infty, \quad C^* = 1$

$r = 0, \quad z > 0, \quad C^* = 1$

Solution for u_r = constant

Integration of Equation 3.2-2 gives

$$u_z = - \frac{u_r . z}{r} + \text{constant.}$$

At $z = 0$, $u_z = 0$ $\quad\therefore$ constant = 0

$\therefore$ Equation 3.2-3 becomes

$$\frac{\partial^2 C^*}{\partial z^2} - \frac{u_r}{D} \cdot \frac{\partial C^*}{\partial r} + \frac{u_r . z}{r \;\; D} \cdot \frac{\partial C^*}{\partial z} = 0$$

Let $y = \left(\dfrac{u_r}{D}\right) \cdot \dfrac{z}{r^{1/2}}$

$$\therefore \quad \frac{d^2 C^*}{dy^2} + \frac{3}{2} \left(\frac{D}{u_r}\right) y \frac{dC^*}{dy} = 0$$

Put $\dfrac{dC^*}{dy} = \emptyset$

$$\therefore \quad \frac{d\emptyset}{dy} + \frac{3}{2} \left(\frac{D}{u_r}\right) y\, \emptyset = 0$$

$$\therefore \ln \phi = \frac{-3}{4}\left(\frac{D}{u_r}\right) y^2 + \ln B_1$$

$$\therefore \frac{dC^*}{dy} = B_1 \exp\left\{- \frac{3}{4}\left(\frac{D}{u_r}\right) y^2\right\}$$

whence $C^* = B_1 \left(\frac{\pi}{3} \cdot \frac{u_r}{D}\right)^{1/2} \operatorname{erf}\left\{\frac{\sqrt{3}}{2}\left(\frac{D}{u_r}\right)^{1/2} . y\right\}$

when $y = \infty$, $C^* = 1$, $B_1 = \left(\frac{3}{\pi} \cdot \frac{D}{u_r}\right)^{1/2}$

$$\therefore C^* = \operatorname{erf}\left\{\frac{\sqrt{3}}{2}\left(\frac{D}{u_r}\right)^{1/2} y\right\}$$

$$\therefore C^i - C = (C^i - C^b) \operatorname{erf}\left\{\frac{\sqrt{3}}{2}\left(\frac{D}{u_r}\right)^{1/2} y\right\}$$

Diff. w.r.to y: $- \frac{dC}{dy} = (C^i - C^b)\left(\frac{3}{\pi} \cdot \frac{D}{u_r}\right)^{1/2} \exp\left\{- \frac{3}{4}\left(\frac{D}{u_r}\right) y^2\right\}$

$$\therefore - \frac{dC}{dz} = (C^i - C^b)\left(\frac{3}{\pi} \cdot \frac{u_r}{D} \frac{1}{r}\right)^{1/2} \exp\left\{- \frac{3}{4} \cdot \frac{u_r}{D} \cdot \frac{z^2}{r}\right\}$$

$$\therefore - \left(\frac{dC}{dz}\right)_{z=o} = (C^i - C^b)\left(\frac{3}{\pi} \cdot \frac{u_r}{D} \cdot \frac{1}{r}\right)^{1/2}$$

From Equation 3.2-1:

$$\dot{n}_a = \int_o^{r_1} 2\pi r . D . (C^i - C^b)\left(\frac{3}{\pi} \cdot \frac{u_r}{D} \cdot \frac{1}{r}\right)^{1/2} dr$$

$$\therefore \dot{n}_a = 4\left(\frac{\pi}{3} \cdot u_r . D\right)^{1/2} r_1^{3/2} (C^i - C^b)$$

Comparing $\dot{n}_a = k_{mean} . \pi r_1^2 (C^i - C^b)$

$$k_{mean} = \frac{4}{(3\pi)^{1/2}}\left(\frac{u_r . D}{r_1}\right)^{1/2} \quad .... \; 3.2\text{-}4$$

Alternatively the local mass transfer coefficient, k_{local} at radius r_1 may be evaluated:

$$\dot{n}_a'' = -D\left(\frac{dC}{dz}\right)_{z=o} = k_{local}\,(C^i - C^b)$$

$$\text{whence } k_{local} = \left(\frac{3}{\pi}\right)^{1/2}\left(\frac{u_r}{r_1}D\right)^{1/2} \qquad \ldots.\ 3.2\text{-}5$$

<u>Solution for $u_r.r$ = constant</u>

Integration of Equation 3.2-2 gives

$$u_z = \text{constant}$$

$$\text{but } (u_z)_{z=o} = 0$$

$\therefore$ Equation 3.2-3 becomes:- $\dfrac{\partial^2 C^*}{\partial z^2} + \dfrac{(u_r.r)}{D.r}\cdot\dfrac{\partial C^*}{\partial r} = 0$

$$\text{Let } y = \left(\frac{u_r.r}{D}\right)^{1/2}\cdot\frac{z}{r}$$

$$\frac{d^2C^*}{dy^2} + y\,\frac{dC^*}{dy} = 0$$

$$\text{Put } \frac{dC^*}{dy} = \emptyset$$

$$\frac{d\emptyset}{dy} + y\,\emptyset = 0$$

$$\ln\emptyset = -\frac{y^2}{2} + \ln B_2$$

$$\frac{dC^*}{dy} = B_2 \exp\left(-\frac{y^2}{2}\right)$$

$$\text{whence } C^* = B_2\left(\frac{\pi}{2}\right)^{1/2}.\mathrm{erf}\left(\frac{y}{\sqrt{2}}\right)$$

when $y = \infty$, $C^* = 1$

$$\therefore B_2 = \left(\frac{2}{\pi}\right)^{1/2}$$

$$\therefore C^* = \text{erf}\left(\frac{y}{\sqrt{2}}\right)$$

$$\therefore C^i - C = (C^i - C^b)\ \text{erf}\left(\frac{y}{\sqrt{2}}\right)$$

Diff. w.r.to y: $-\frac{dC}{dy} = (C^i-C^b).\left(\frac{2}{\pi}\right)^{1/2}.\ \exp\left\{-\frac{y^2}{2}\right\}$

$$\therefore\ -\frac{dC}{dz} = (C^i-C^b)\left(\frac{u_r.r.}{D}\ \ \frac{2}{\pi}\right)^{1/2}.\ \frac{1}{r}\ .\ \exp\left\{-\ \frac{u_r.r}{2D}\ .\ \frac{z}{r}\right\}^2$$

$$-\left(\frac{dC}{dz}\right)_{z=o} = (C^i-C^b)\ \left(\frac{u_r.r.}{D}\ \ \frac{2}{\pi}\right)^{1/2}\ .\ \frac{1}{r}\ .$$

From Equation 3.2-1:

$$\dot{n}_a = \int_o^{r_1} 2\pi r.\ D.\ (C^i-C^b)\left(\frac{u_r.r}{D}\ .\ \frac{2}{\pi}\right)^{1/2}\ .\ \frac{1}{r}\ .\ dr$$

$$\therefore\ \dot{n}_a = 2\ (2\pi\ D.u_r.r.)^{1/2}\ .r_1.(C^i-C^b)$$

Comparing $\dot{n}_a = k_{mean}\ .\pi r_1^{\ 2}.\ (C^i-C^b)$

$$k_{mean} = 2\left(\frac{2}{\pi}\right)^{1/2}\left(D.u_r.r\right)^{1/2}\ .\ \frac{1}{r_1}\quad \ldots\ldots\ 3.2\text{-}6$$

Again the local mass transfer coefficient, k_{local}, at radius r_1 may be evaluated:

$$\dot{n}_a'' = -D\left(\frac{dC}{dz}\right)_{z=o} = k_{local}\ \ (C^i-C^b)$$

whence $k_{local} = \left(\frac{2}{\pi}\right)^{1/2}.\ \left(D.u_r.r\right)^{1/2}.\ \frac{1}{r_1}$ 3.2-7

Thus it may be seen that the solutions given by Equation 3.2-4, 5, 6 and 7 all anticipate mass transfer coefficients of the form

$$k \propto \left(\frac{D.u_{r_1}}{r_1} \right)^{1/2}$$

The same system has been treated by Beek and Kramers[49], using a slightly different technique, which anticipates a similar solution, for $u_r.r$ = constant, as that given above. However, the solution for the case where u_r = constant was not treated.

4.0 ROOM TEMPERATURE INVESTIGATION

The room temperature investigation consisted of studies of a gas jet impinging normally on a liquid surface. Measurements were made on the depression formed, the circulation within the liquid, and the rate of transfer of gas into the liquid. Both the jet velocity and momentum and the liquid properties were varied over a wide range. The investigation has been divided into four main sections:

a). The nozzle characteristics, including the correlation of exit velocity and momentum flux with mass flow, and the velocity profiles within the jet.

b). The dimensions and shape of the depression formed in liquids of varying properties, including mercury.

c). The circulation patterns and velocities within the liquid bath. Liquid surface velocities.

d). Mass transfer from the gas to the liquid, including the determination of mass transfer coefficients.

4.1 Experimental Apparatus

The main room temperature apparatus consisted of a 73cm internal diameter perspex cylinder on a 91.5cm square perspex base. This was supported in a framework, to which three traversing systems were attached. The first of these allowed vertical motion of the lance along the axis of the cylinder, the second, horizontal and vertical movement of a pitot tube, and the third formed a support for a Griffin and George vernier telescope, type S31-925. The arrangement is shown in Figures 4.1-1 and 4.1-2.

The quadrant shaped converging nozzle, throat diameter .253cm., was situated at the end of a 1.27cm. internal diameter pipe. There was no divergence, so the gas flow was subsonic throughout. The air was supplied through a reservoir tank from a Holman reciprocating two stage compressor. Carbon dioxide was supplied from cylinders. The gas flow was regulated by two valves, one to bleed to atmosphere and the other to throttle the flow. The temperature of the gas was adjusted by passing it through a copper spiral immersed in a thermostatically controlled water bath. In the case of CO_2, a heater was also attached to the cylinder head. The gas flow was metered by a rotameter, with suitable correction made for the gas temperature and pressure.

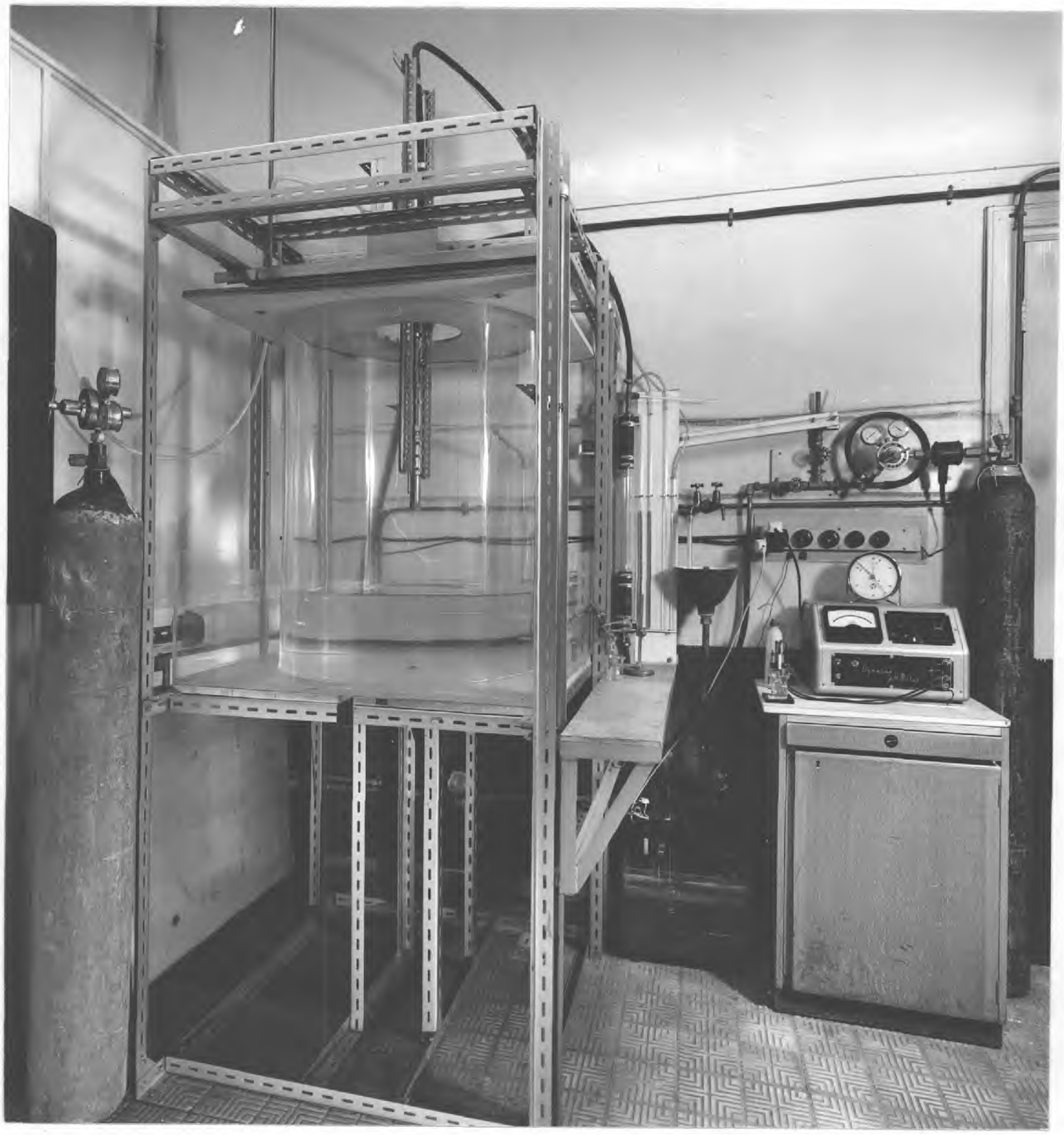

FIGURE 4.1-1 PHOTOGRAPH SHOWING GENERAL LAYOUT OF ROOM TEMPERATURE APPARATUS.

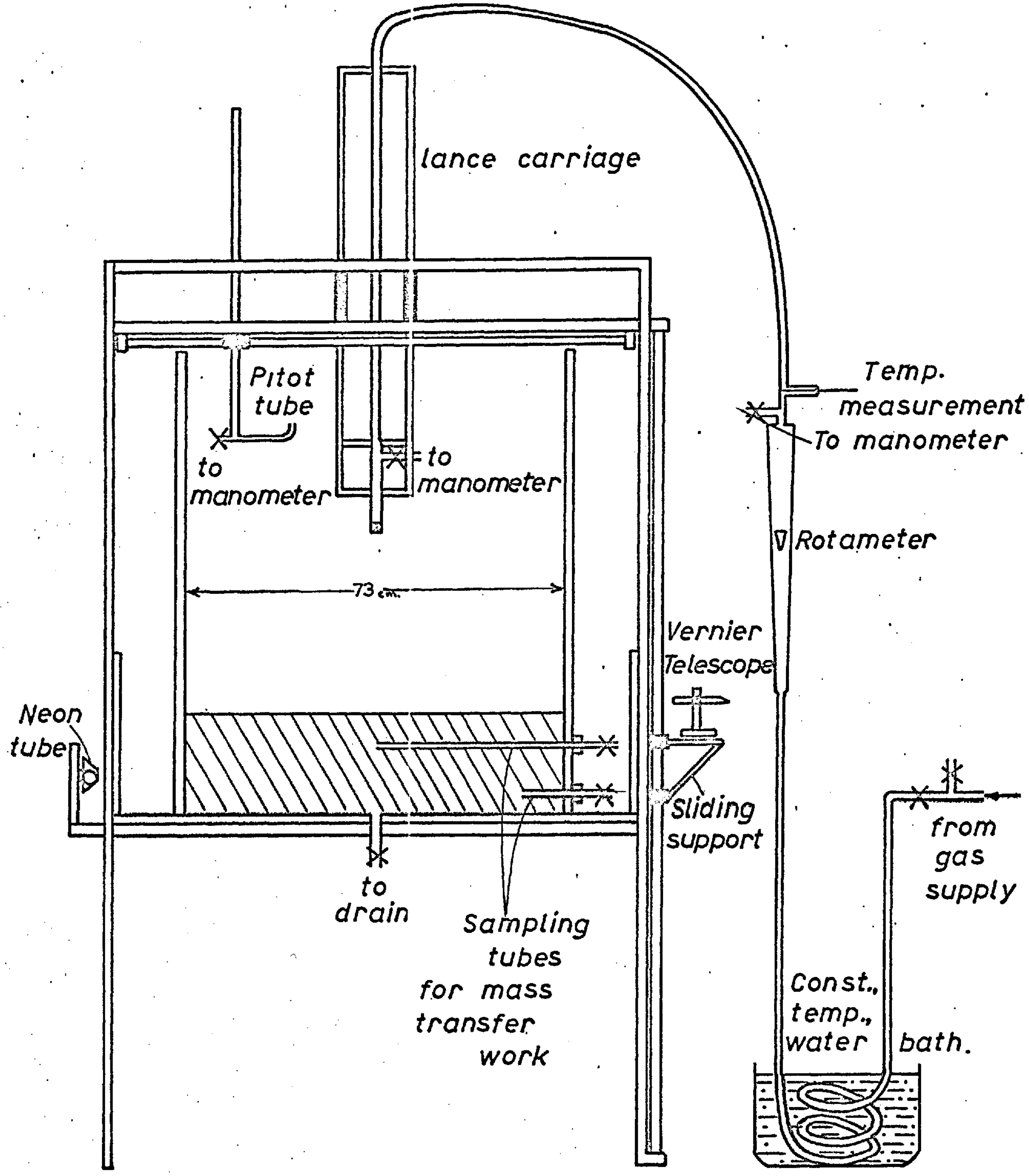

FIG.4.1-2 EXPERIMENTAL APPARATUS FOR ROOM TEMPERATURE INVESTIGATION

4.2 Materials

The purities of the cylinder gases used were specified as follows: carbon dioxide, less than 10 p.p.m. impurities (mainly oxygen and nitrogen); nitrogen, less than 10 p.p.m. residual oxygen.

The main impurities in the tap water (after Thresh et al[50]) were as follows: $CaCO_3$, 60 p.p.m; $MgCO_3$, 30 p.p.m; Na_2CO_3, 170 p.p.m; Na_2SO_4, 200 p.p.m. and NaCl, 250 p.p.m.

The polyvinyl alcohol solution used was a 4% solution of "Alcotex" 88-40 powder in distilled water, with a viscosity of 40 centipoise and surface tension of 47 dynes/cm at 18°C[44].

Other properties of the liquids used were:

	Tap Water	Mercury
Density ($g./cm^3$)	1.00	13.56
Surface Tension (dynes/cm)	73	487
Viscosity (centipoise)	1.11 (16°C)	1.55
CO_2 solubility ($moles/cm^3$)	4.395×10^{-5} (16°C) to 3.700×10^{-5} (22°C)	- -
CO_2 diffusivity (cm^2/sec)[51]	1.4×10^{-5} (16°C) to 1.7×10^{-5} (22°C)	- -

Values taken from reference 52 except where otherwise stated.

4.3 Measurements on the Nozzle

Firstly, the relationships between pressure drop across the nozzle, and the mass flow $\dot{m}$, exit velocity V_J and momentum of jet $\dot{M}$ were investigated. The following assumptions were made:

i). The flow through the nozzle was isentropic:

$$\int \frac{1}{\rho}\, dP + \frac{\Delta\, v^2}{2} = 0$$

ii). The gas expanded adiabatically:

$$\frac{P}{\rho^{\gamma}} = \text{constant}$$

iii). The pressure at the exit plane of the nozzle was atmospheric.

iv). The velocity was uniform across the exit plane, which gives:

$$\dot{m} = \rho_2\, a_2\, V_J$$

These assumptions lead to the following expression for subsonic mass flow through the convergent nozzle:

$$\dot{m} = a_2 \left[\frac{\frac{2\gamma}{\gamma - 1} \cdot P_2\, \rho_1 \left\{ \left(\frac{P_2}{P_1}\right)^{\frac{2-\gamma}{\gamma}} - \left(\frac{P_2}{P_1}\right)^{\frac{1}{\gamma}} \right\}}{1 - \left\{ \left(\frac{P_2}{P_1}\right)^{\frac{1}{\gamma}} \cdot \frac{a_2}{a_1} \right\}^2} \right]^{\frac{1}{2}} \qquad \ldots .4.3\text{-}1$$

The upstream density ρ_1 was calculated assuming the temperature of the gas to be that measured at the rotameter exit.

The value of $\dot{m}$ calculated from Equation 4.3-1 was compared with the value obtained from the corrected rotameter reading. A coefficient of discharge Cd, to correlate the two sets of values, was introduced into Equation 4.3-1, which then becomes:

$$\dot{m} = C_d \cdot a_2 \left[\frac{\frac{2\gamma}{\gamma-1} \cdot P_2 \quad \rho_1 \left\{ \left(\frac{P_2}{P_1}\right)^{\frac{2-\gamma}{\gamma}} - \left(\frac{P_2}{P_1}\right)^{\frac{1}{\gamma}} \right\}}{1 - \left\{ \left(\frac{P_2}{P_1}\right)^{\frac{1}{\gamma}} \cdot \frac{a_2}{a_1} \right\}^2} \right]^{\frac{1}{2}} \quad \ldots.4.3\text{-}2$$

The variation of C_d with mass flow and throat Reynolds Number is shown in Figure 4.3-1 for air and CO_2. The values are similar to those obtained by Kastner et al.[53]

The momentum Flux $\dot{M}$ was calculated thus:

$$\dot{M} = \dot{m} \, V_J$$

$$= C_d^2 \cdot a_2 \left[\frac{\frac{2\gamma}{\gamma-1} \cdot P_2 \quad \left\{ \left(\frac{P_1}{P_2}\right)^{\frac{\gamma-1}{\gamma}} -1 \right\}}{1 - \left\{ \left(\frac{P_2}{P_1}\right)^{\frac{1}{\gamma}} \cdot \frac{a_2}{a_1} \right\}^2} \right] \quad \ldots.4.3\text{-}3$$

The variation of $\dot{M}$ with mas flow for both air and CO_2 is also shown in Figure 4.3-1. Additional measurements of $\dot{M}$, obtained by impinging the jet on a 30cm. dia. flat plate, supported on a Mettler K7 single pan balance, resulted in momentum fluxes from 5 to 10% in excess of those from Equation 4.3-3. As the accuracy

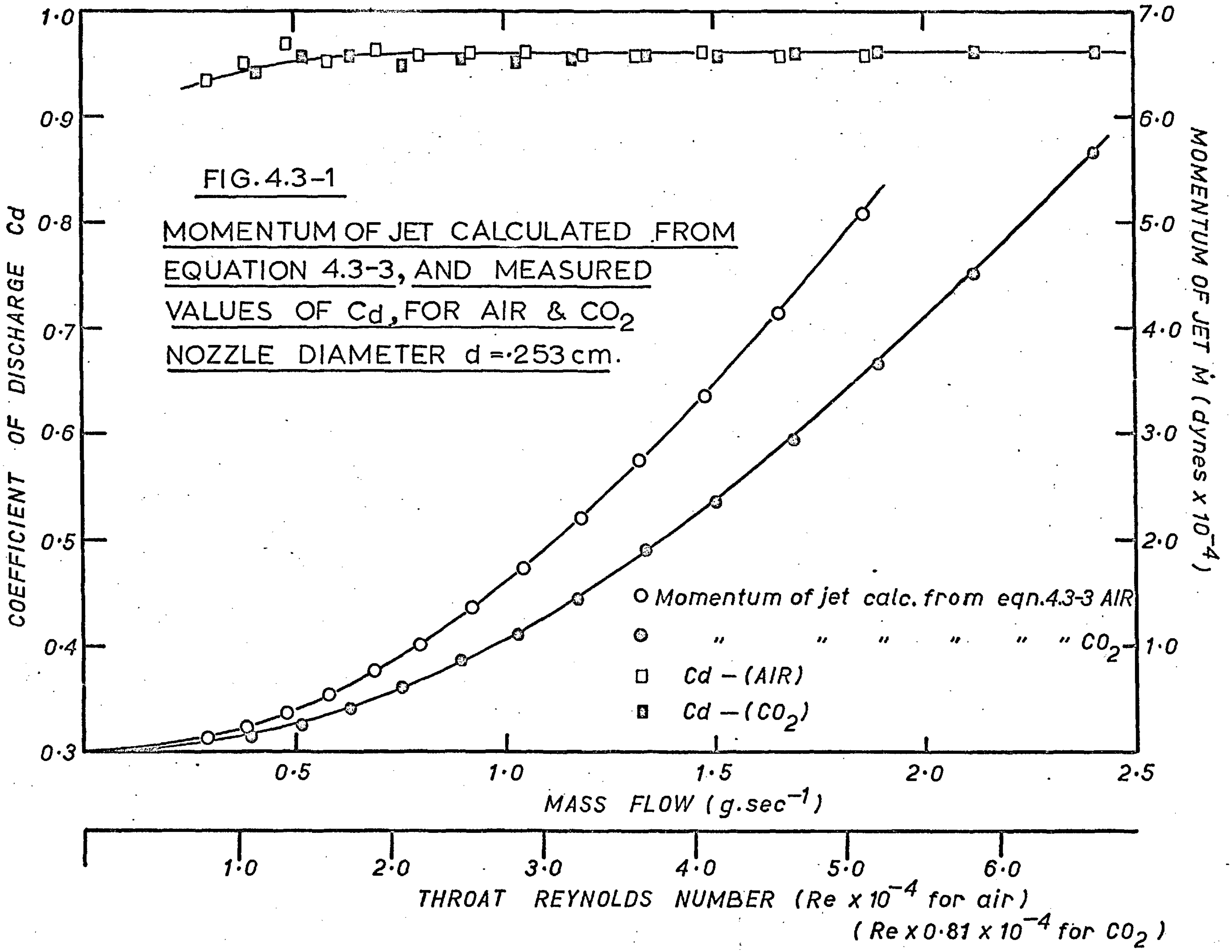

FIG. 4.3-1

MOMENTUM OF JET CALCULATED FROM EQUATION 4.3-3, AND MEASURED VALUES OF Cd, FOR AIR & CO_2 NOZZLE DIAMETER d = ·253 cm.

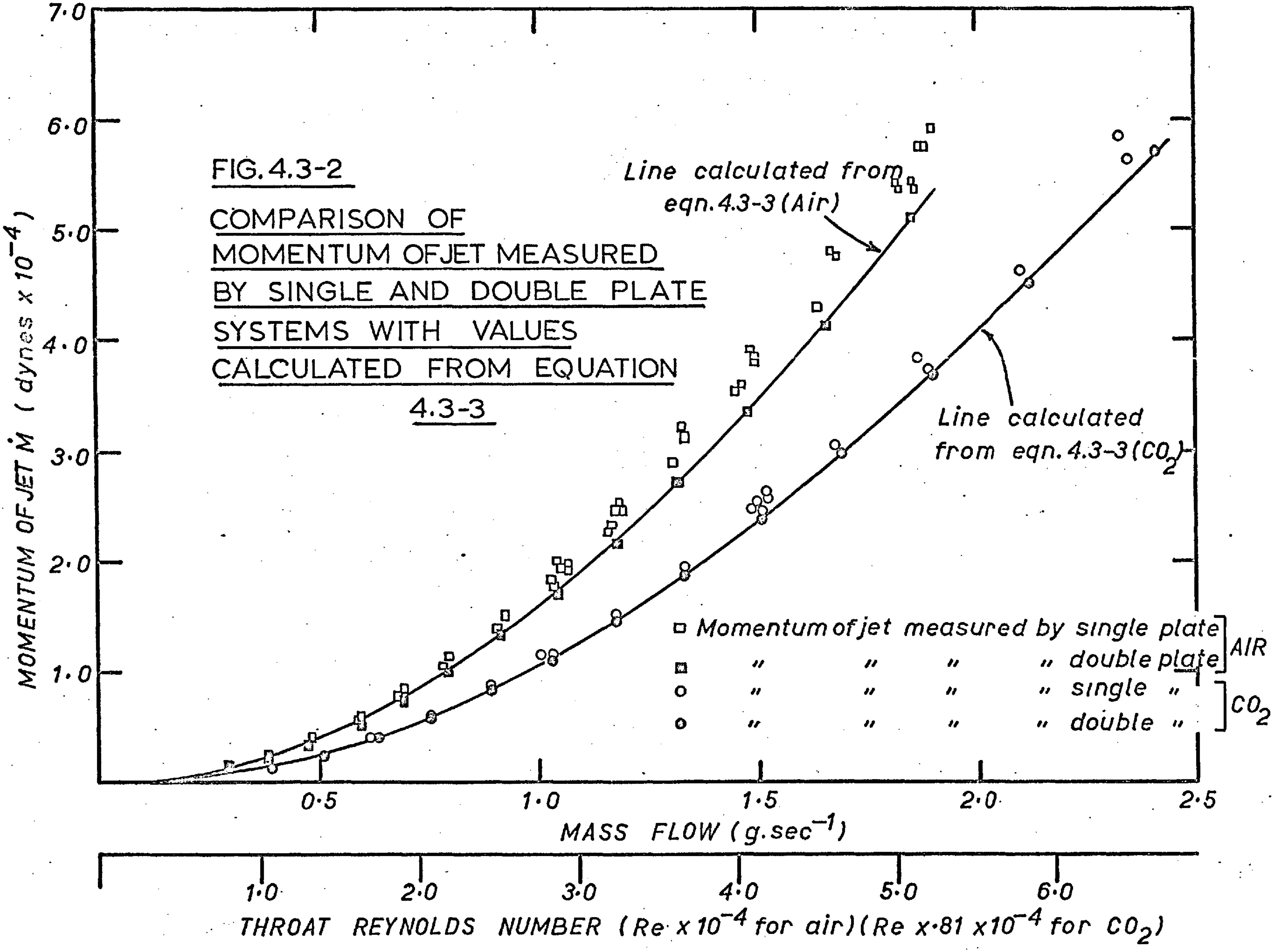

FIG. 4.3-2

COMPARISON OF MOMENTUM OF JET MEASURED BY SINGLE AND DOUBLE PLATE SYSTEMS WITH VALUES CALCULATED FROM EQUATION 4.3-3 of the impingement method was estimated to be ± 1%, the discrepancy was probably due to either the gas leaving the plate with a small upward velocity, as indicated by Bradshaw and Love,[34] ~~or to the additional momentum of the gas entrained into the radial wall jet produced on the plate.~~ Further tests were made with a second 30cm. dia. plate, with a 10cm. hole in the centre, supported by spacers on top of the first one, so that the jet passed between the two plates. The distance between the plates was sufficient to contain the entire jet, but small enough to prevent any entrainment or vertical velocity in the radial wall jet.

In practice a separation of 0.5cm. was used, and momentum fluxes measured with this system, Figure 4.3-2, agreed within ± 1% of those from Equation 4.3-3.

4.4 Velocity Profiles in the Free Jet

As discussed in section 2.3, the decrease in the centre line velocity Vo with the distance from the nozzle x, has been found by several investigators to be in reasonable agreement with the equation:

$$\frac{V_o}{V_J} = K \frac{d}{x} \qquad \text{———} \qquad 4.4-1$$

$$\text{for } x > 9d$$

Also, for a given distance x, the velocity profile approximates to a normal error curve of the form:

$$\frac{V}{V_o} = \exp \left\{ -\beta \left(\frac{r}{x} \right)^2 \right\}$$

The momentum is given by:

$$\dot{M} = \int_0^{\infty} 2\pi r \rho V^2 \, dr$$

$$= \int_0^{\infty} 2\pi r \rho V_o^2 \exp\left\{ -2\beta\left(\frac{r}{x}\right)^2 \right\} \, dr$$

Now at the nozzle:

$$\dot{M} = \frac{\pi}{4} d^2 \rho V_J^2$$

Using equation 4.4-1 it can be shown that:

$$\beta = 2 K^2$$

A pitot tube was used to investigate the variation of velocity within the jet. The decrease in centre line velocity with distance from the nozzle, for various throat Reynolds Numbers, is shown in Figure 4.4-1. At the lowest value of Re (8.0×10^3) there is good agreement between measured values of V_o/V_J and Equation 4.4-1, with K = 6.2. With increasing Re, up to 5.1×10^4, there is a steady increase in the value of K, up to 8.6, providing measurements are confined to the region $9 < x/d < 30$. For $x/d > 30$ the experimental values of V_o/V_J approach the line $V_o/V_J = 6.2\ d/x$. A similar effect on K for increasing Re was also noted by Baines.[29]

The geometric origin of the jet was obtained by extrapolating back to the jet axis the lines connecting the radial positions $r_{0.5}$ and $r_{0.1}$, where the jet velocities V were equal to 1/2 and 1/10 of the centre line velocity respectively. From Figure 4.4-2 it will be seen that the distance of the origin behind the plane of the nozzle (a) was 0.5cm.

The measured velocity profiles across a given plane fit normal error curves satisfactorily. It has been found preferable to plot V/V_o against $r/x+a$ (Figure 4.4-3). An increase in the value of β with increasing Re, was noted, from $\beta = 80$ ($Re = 8 \times 10^3$) to 100 ($Re = 3 \times 10^4$). This increase is consistent with the variation noted in the value of K.

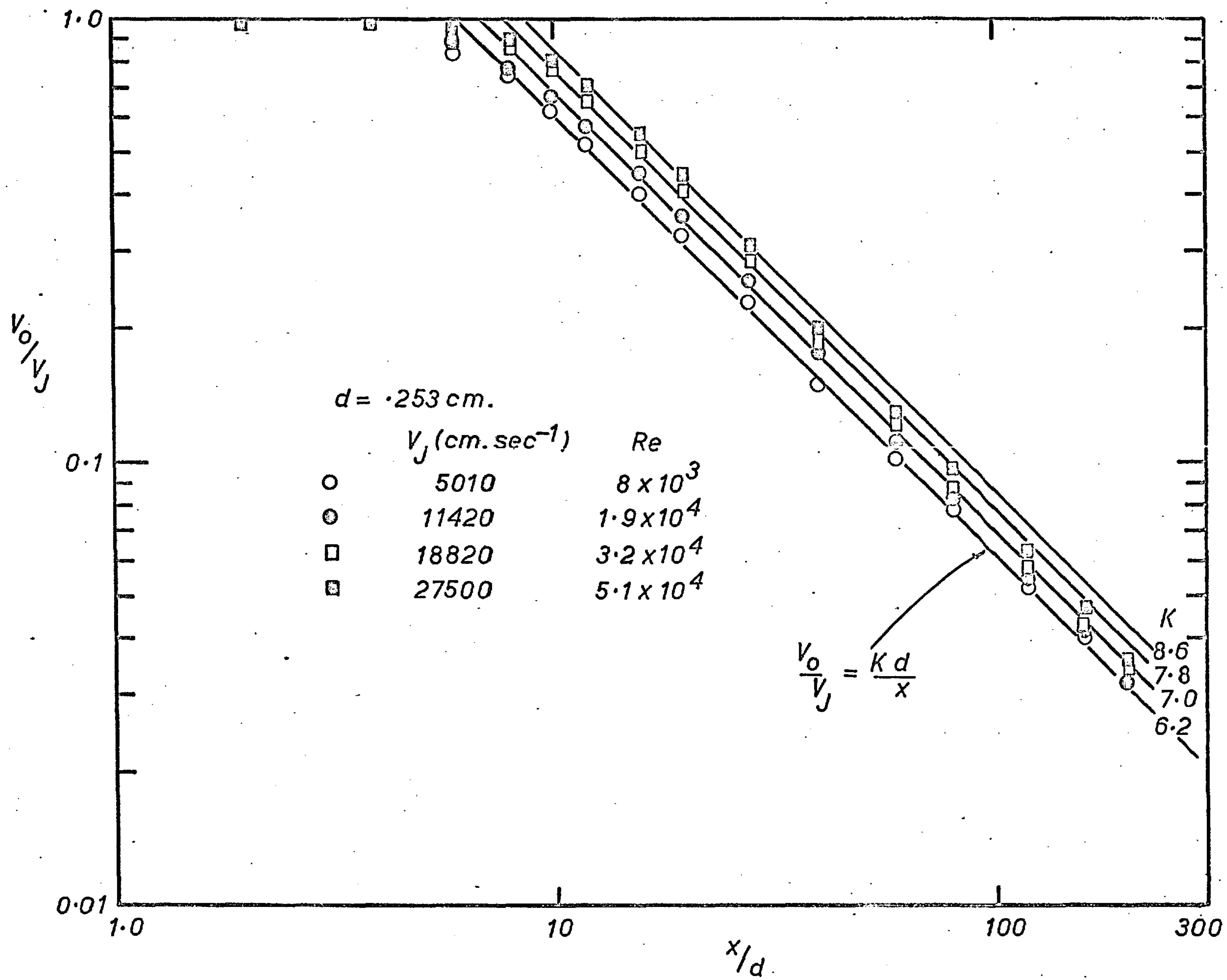

FIG. 4.4-1 DECREASE IN JET CENTRE LINE VELOCITY V_o WITH DISTANCE FROM NOZZLE x (AIR)

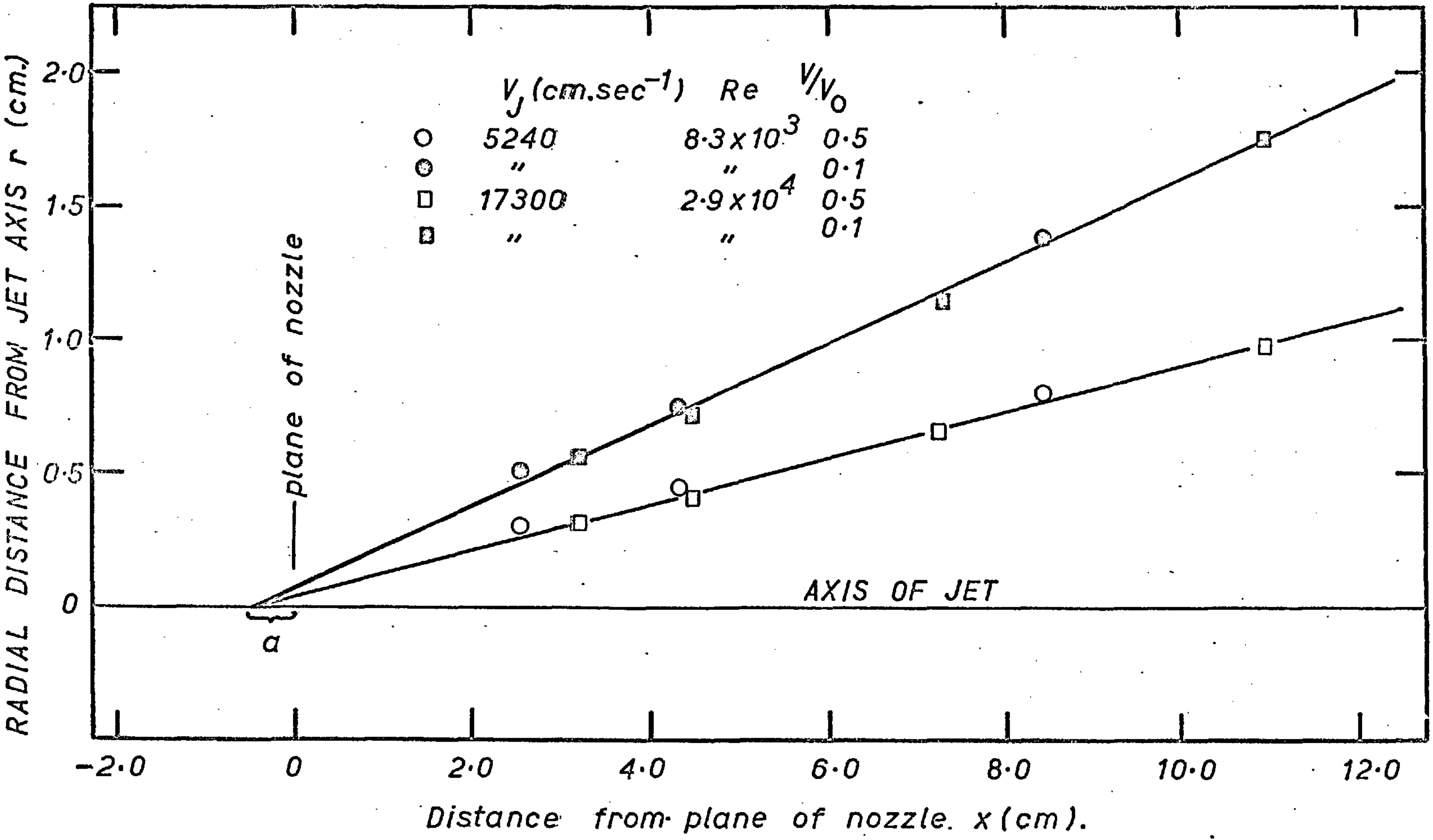

FIG. 4.4-2 RADIAL DISTANCES FROM JET AXIS AT WHICH $V=0{\cdot}5V_0$ AND $V=0{\cdot}1V_0$, versus DISTANCE FROM PLANE OF NOZZLE

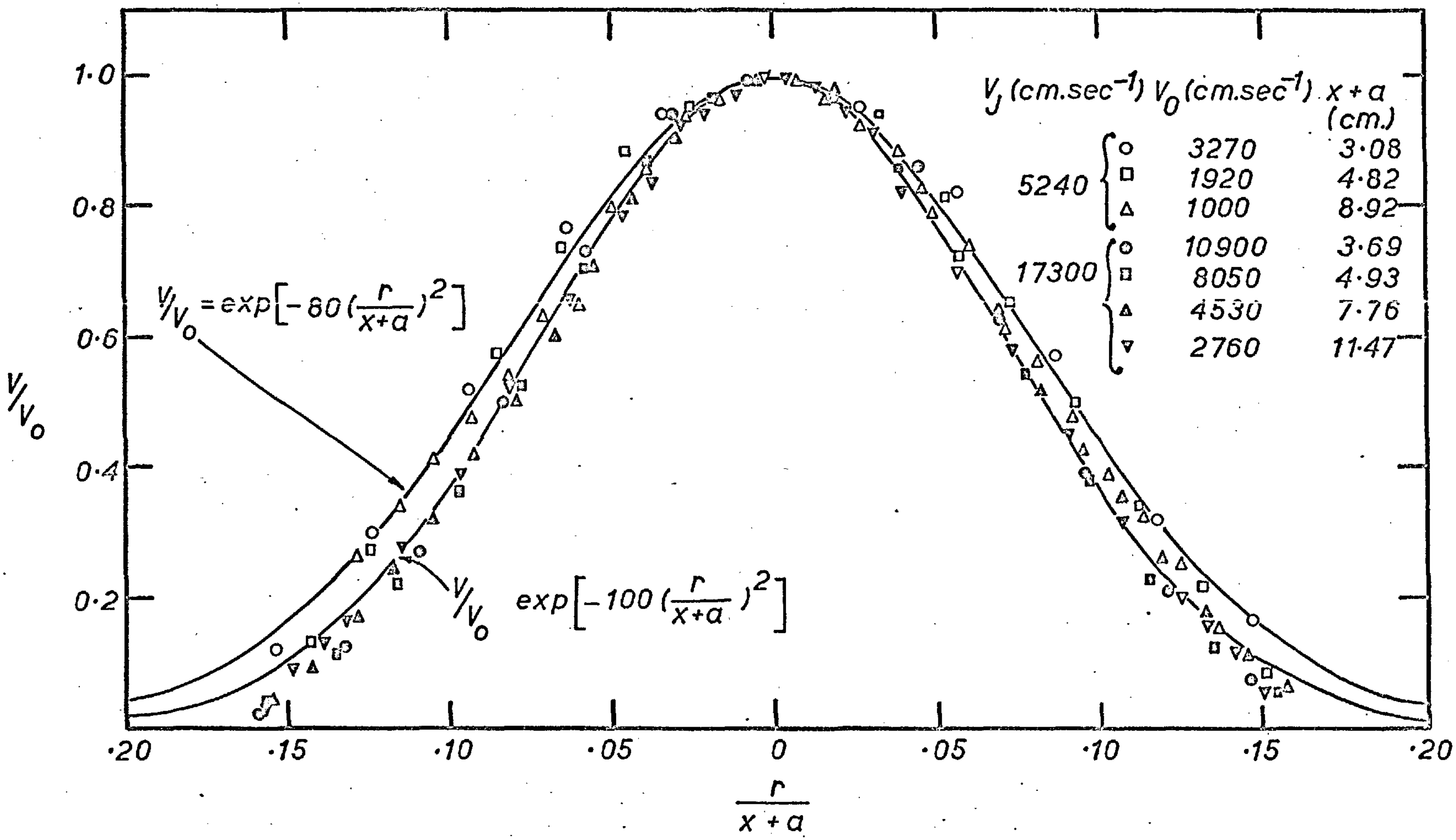

FIG. 4.4-3 MEASURED VELOCITY PROFILES IN FREE JET, COMPARED WITH NORMAL ERROR CURVES

4.5 Measurements on the Depression in Aqueous Solutions

At the point of impingement, the jet produced a depression or shallow cavity, in the liquid surface. Except at very low blowing rates, this depression was somewhat unstable, and the surface oscillated in both a lateral and a vertical direction. The gas jet produced a tangential drag on the surface of the liquid, resulting in the circulation of the liquid bath and also in the formation of a raised lip around the edge of the depression. Ripples originating in the depression surface spread out over the remaining liquid surface. For large distances between the nozzle and liquid the depression was wide and shallow, with illdefined edges owing to the rippling. At a definite cavity depth, liquid was torn from the tips of the ripples, forming a spray of droplets issuing from the depression. When the drops fell back to the liquid surface, they gave rise to small gas bubbles. Only when the nozzle was very close to the liquid surface were bubbles of gas forced directly from the jet into the liquid.

The vernier telescope, capable of measurement to an accuracy of ± 0.01cm, was used in conjuction with a fixed metre rule behind the tank to measure the following:

i). The depth of the cavity below the free liquid surface (n_0)

ii). The height of the surrounding lip above the free liquid surface (l)

iii). The diameter of the cavity at the top of the lip (m)

In all cases maximum, minimum and the arithmetic mean values were recorded. The liquid meniscus at the edge of the tank caused the liquid surface to be obscured, and a pointer with a fixed mark was used to determine its exact position.

Stagnation pressure analysis at the centre of the depression leads to the expression:

$$\rho_L g n_o + \frac{2\sigma}{R_o} = \frac{1}{2} \rho_g V_o^2$$

Using Equation 4.4-1:

$$\rho_L g n_o + \frac{2\sigma}{R_o} = \frac{1}{2} \rho_g V_J^2 K^2 \frac{d^2}{x^2}$$

whence:

$$n_o \left(1 + \frac{2\sigma}{\rho_L g R_o n_o} \right) = \frac{\beta}{\pi} \cdot \frac{\dot{M}}{\rho_L g x^2}$$

Substituting h + n_o as the distance of the stagnation point from the nozzle:

$$\frac{n_o}{h} \left(1 + \frac{n_o}{h} \right)^2 \left(1 + \frac{2\sigma}{\rho_L g R_o n_o} \right) = \frac{\beta}{\pi} \cdot \frac{\dot{M}}{\rho_L g h^3} \quad \text{....4.5-1}$$

Neglecting surface tension this reduces to:

$$\frac{n_o}{h} \left(1 + \frac{n_o}{h} \right)^2 = \frac{\beta}{\pi} \cdot \frac{\dot{M}}{\rho_L g h^3} \quad \text{....4.5-2}$$

Values of n_o/h are tabulated in Appendix 1 for values of $\dot{M}/\rho_L g h^3$ in the range 0.0002 to 0.025.

At the same time, for subsequent calculations of surface area and radius of curvature (see pages 54, 55), the values of $(n_o+1)/h$ and m/h have also been shown for values of $\dot{M}/\rho_L gh^3$ greater than 0.0005. Below this value, the depression was shallow and the lip was obscured by the meniscus at the edge of the tank. In some cases, measurements of the diameter of the depression were made at the level of the free surface. These values, which have been included in the appendix, have been identified by an asterisk.

The oscillation of the bottom of depression about its mean position increased with the nozzle-liquid distance. The variation due to the oscillation of n_o about the arithmetic mean values shown was between ± 7% at h = 4cm, and ± 20% at h = 40cm. Similar results were obtained for total depth of cavity n_o+1. The variation in the diameter of the cavity m was ± 10%, except at values of h less than 10cm, when the cavity began to rotate about the jet axis, resulting in apparent variations of up to ± 40%.

Figure 4.5-1, showing the variation of n_o/d with $\dot{M}/\rho_L gd^3$ for given values of h/d for the air-water system, is included for comparison with the work of Mathieu[37] on the commencement of splashing. The broken line indicates the values of n_o/d for the beginning of splashing. These show a slight decrease, corresponding to values of n_o from 1.35cm. to 1.10cm., for h/d increasing from 16 to 165. A similar decrease with increasing h/d was also noted by Mathieu.

The variations of n_o/h, $(n_o+1)/h$ and m/h with $\dot{M}/\rho_L g h^3$ are shown in Figures 4.5-2 to 4.5-4 respectively. Results obtained for CO_2 impinging on water and air on 4% polyvinyl alcohol solution are included with the air-water system. The curve on Figure 4.5-2 represents Equation 4.5-2 (neglecting surface tension) with $\beta = 115$. Above the range $\dot{M}/\rho_L g h^3$ equals 0.001 to 0.002 the results fall within 20% below the given curve. Below this range the results fall up to 40% above the given curve. In Figures 4.5-3 and 4.5-4 the curves drawn represent the experimental results within ± 15% and ± 10% respectively.

In order to calculate the effect of surface tension on the depth of the depression, it was necessary to measure the radius of curvature of the cavity at the stagnation point. It was also necessary to determine the surface area of the depression at fixed values of jet momentum and nozzle-liquid distance, for later determinations of mass transfer coefficients. Therefore the shape of a range of depressions was measured, using the vernier telescope and correcting for refraction. Typical results are shown in Figures 4.5-5a and 4.5-5b. Superimposed upon the measured shapes are quadratic curves of the general form:

$$n = 4\alpha r^2 \qquad \ldots . 4.5\text{-}3$$

where:

$$\alpha = \frac{n_o + 1}{m^2}$$

Birkhoff and Zarantonello[54] have outlined one approximate solution to axially-symmetrical flow problems which is relevant to the present problem, and anticipates a paraboloidal cavity. Figures 4.5-5a and 4.5-5b show the shapes can be adequately described by paraboloids of revolutions, the fit being better the smaller $(n_o+1)/m^2$ becomes. The surface area of these paraboloids of revolution (S), of the form of Equation 4.5-3, is given by:

$$S = \frac{\pi \cdot m^4}{96(n_o+1)^2}\left[\left\{1+\frac{16(n_o+1)^2}{m^2}\right\}^{3/2} -1\right] \quad \text{....4.5-4}$$

Values of S/h^2 are shown in Appendix 1, and are plotted in Figure 4.5-6 versus $\dot{M}/\rho_L g h^3$. A comparison of the area given by this equation with that computed by numerical integration of the measured shape is shown in Table 4.5-1, and on Figure 4.5-6. Since the two values agree within 7.5%, Equation 4.5-4 has been used to calculate the areas of all depressions, and these are given in the Appendix 1, and are shown on Figure 4.5-6. In this figure the curve drawn represents the experimental data to ± 15%.

The radius of curvature of the liquid at the stagnation point, calculated using Equation 4.5-3, is given by:

$$R_o = \frac{1}{8\alpha} = \frac{m^2}{8(n_o+1)} \quad \text{....4.5-5}$$

Allowance for the effect of surface tension on the relationship between n_o, and $\dot{M}$ and h has been made by calculation of the term $1 + (2\sigma/\rho_L g R_o n_o)$, which is shown in Appendix 1.Figure 4.5-7 shows:

$$\frac{n_o}{h}\left(1+\frac{n_o}{h}\right)^2\left(1+\frac{2\sigma}{\rho_L g R_o n_o}\right) \text{versus } \frac{\dot{M}}{\rho_L g h^3}$$

and also Equation 4.5-1 with $\beta = 115$.

Table 4.5-1

Comparison of Area of Depression computed from measured shape with that predicted from paraboloid of revolution

h (cm)	$\dot{M}$ (dynes)	$\frac{\dot{M}}{\rho_L g h^3}$	Numerically Computed Area (cm^2)	Area Calculated from Eqn.4.5-4 (cm^2)	% Variation in calculated from measured area
4.00	1450	.0231	13.1	12.5	-4.5
6.01	1450	.00685	10.3	10.3	0
8.09	1450	.00280	12.6	11.8	-6.5
"	3800	.00732	22.6	20.9	-6.5
"	7850	.0151	50.6	46.8	-7.5
11.50	3850	.00258	21.4	21.0	-2.0
"	7950	.00534	39.1	38.3	-2.0
"	13800	.00925	67.9	65.0	-4.5
17.12	7950	.00162	42.3	42.6	+0.5
"	13800	.00281	67.0	65.0	-3.0
"	22200	.00451	91.2	87.4	-4.0
23.97	13650	.00101	78.7	75.6	-4.0
"	21850	.00162	98.0	97.0	-1.0
"	33250	.00247	118.5	112.0	-5.5

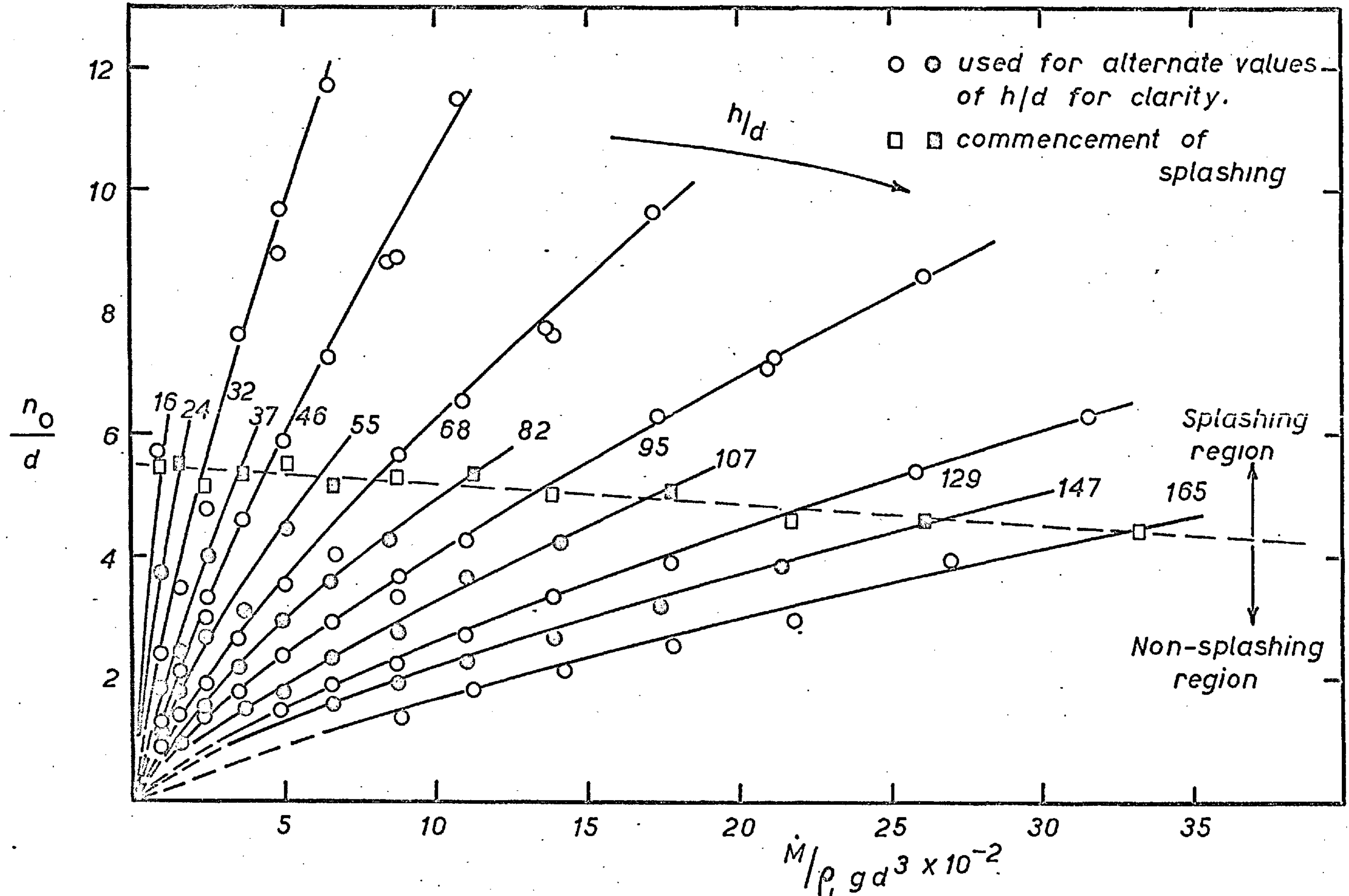

FIG. 4.5-1 VARIATION OF DEPTH OF DEPRESSION BELOW FREE LIQUID SURFACE n_o, WITH JET MOMENTUM $\dot{M}$, FOR GIVEN VALUES OF NOZZLE LIQUID DISTANCE h. AIR WATER SYSTEM, SHOWING COMMENCEMENT OF SPLASHING

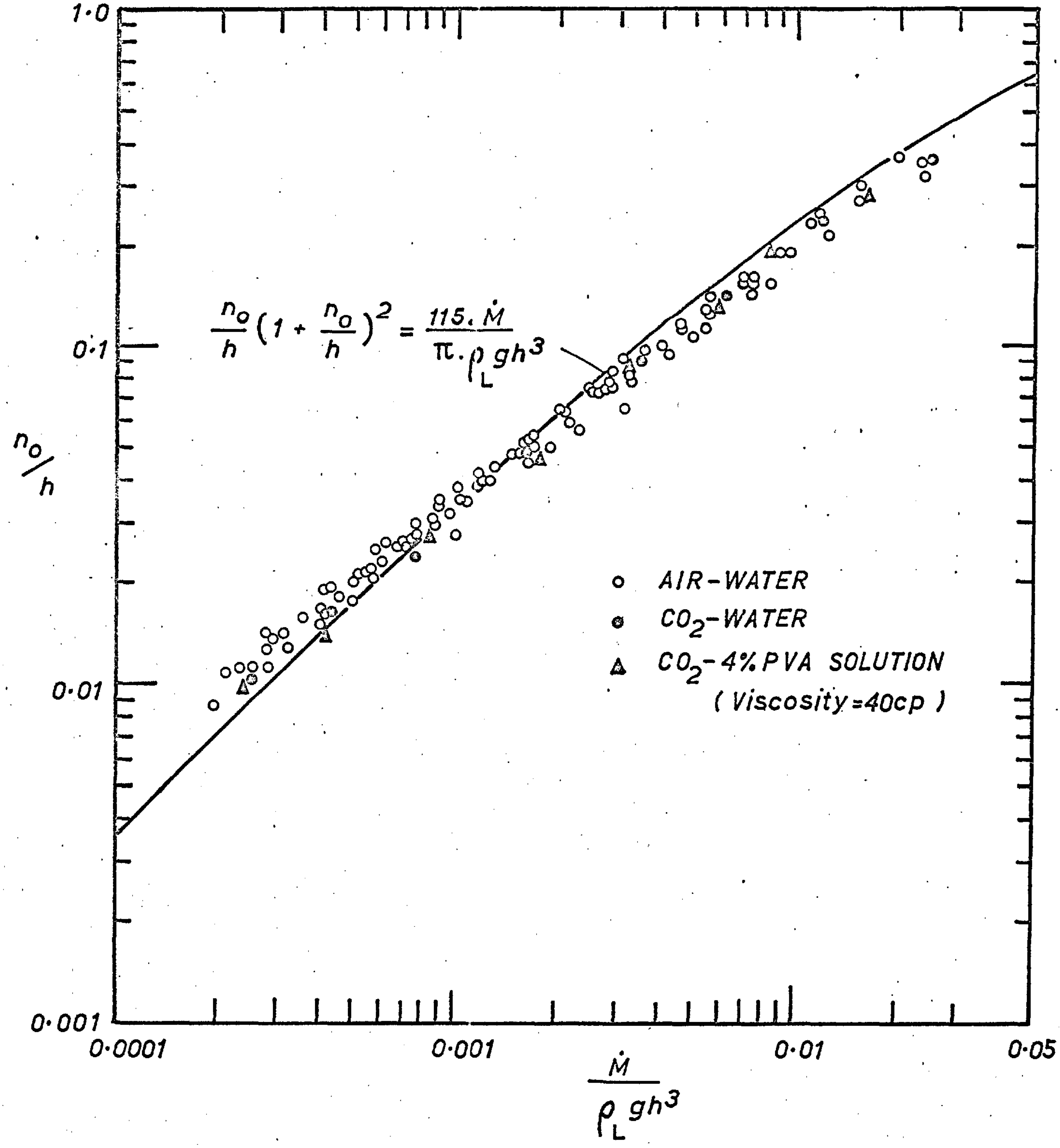

FIG. 4.5-2 VARIATION OF DEPTH OF DEPRESSION BELOW FREE LIQUID SURFACE n_o, WITH JET MOMENTUM $\dot{M}$, AND NOZZLE-LIQUID DISTANCE h, (AQUEOUS SOLUTIONS.)

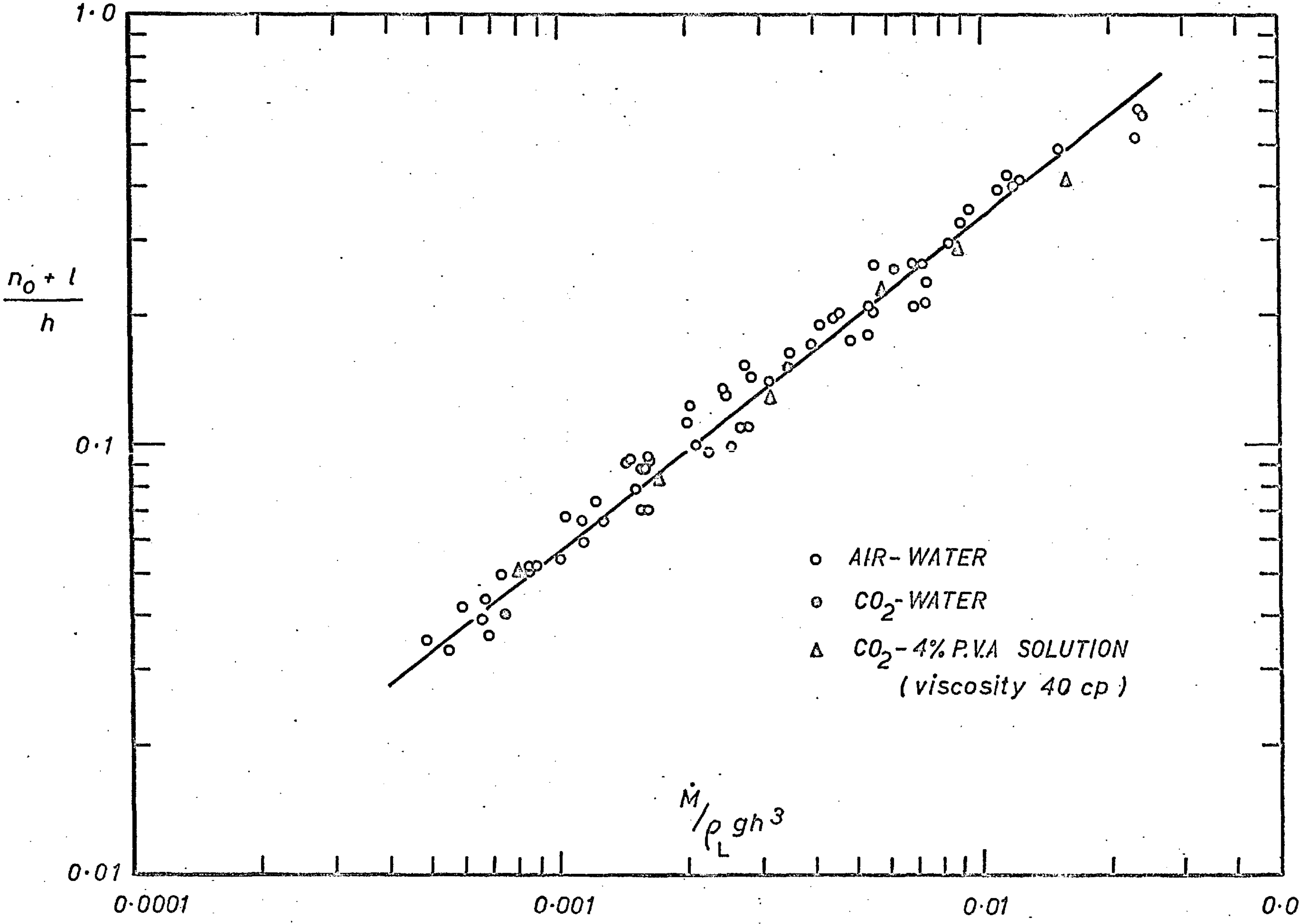

FIG. 4.5-3 VARIATION OF TOTAL DEPTH OF DEPRESSION$(n_o + l)$, WITH JET MOMENTUM $\dot{M}$ AND NOZZLE-LIQUID DISTANCE h,(AQUEOUS SOLUTIONS)

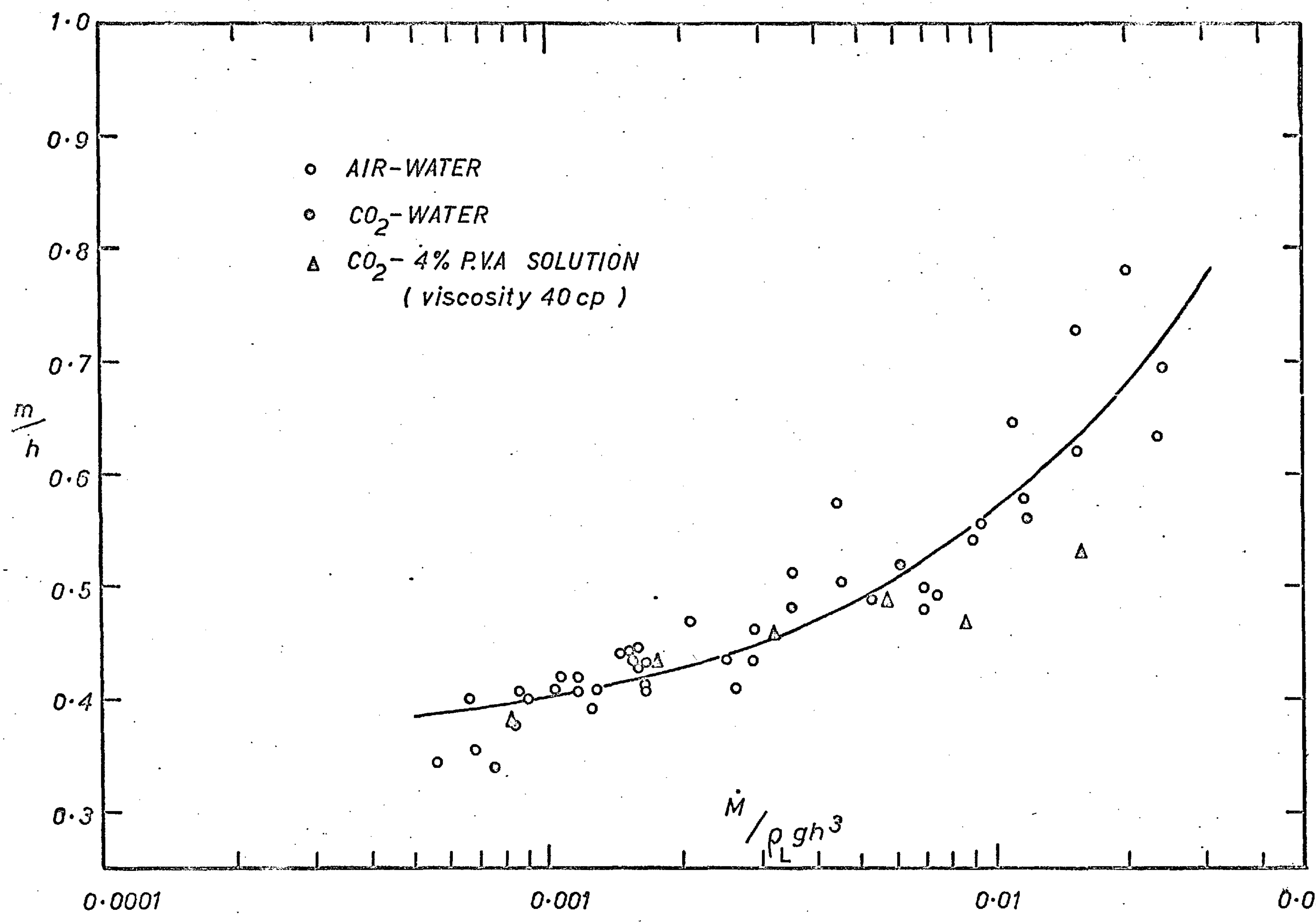

FIG. 4.5-4 VARIATION OF DIAMETER OF DEPRESSION ACROSS LIP m, WITH JET MOMENTUM $\dot{M}$, AND NOZZLE-LIQUID DISTANCE h, (AQUEOUS SOLUTIONS)

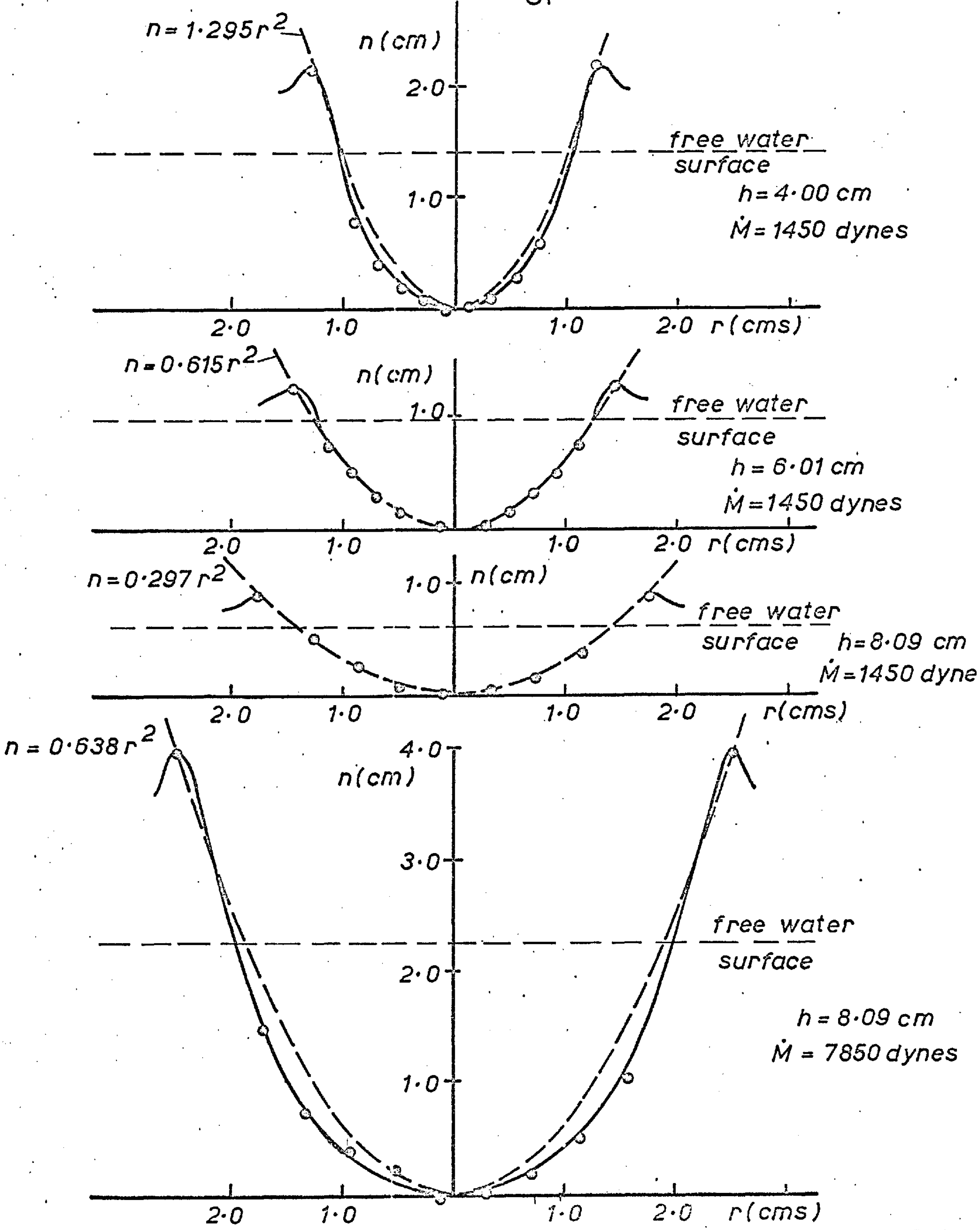

FIG. 4.5-5a MEASURED POINTS ON THE SECTION THROUGH THE DIAMETER OF EACH DEPRESSION, COMPARED WITH A PARABOLA FITTED TO THE CENTRE OF THE DEPRESSION AND THE TOP OF THE LIP (AIR-WATER SYSTEM)

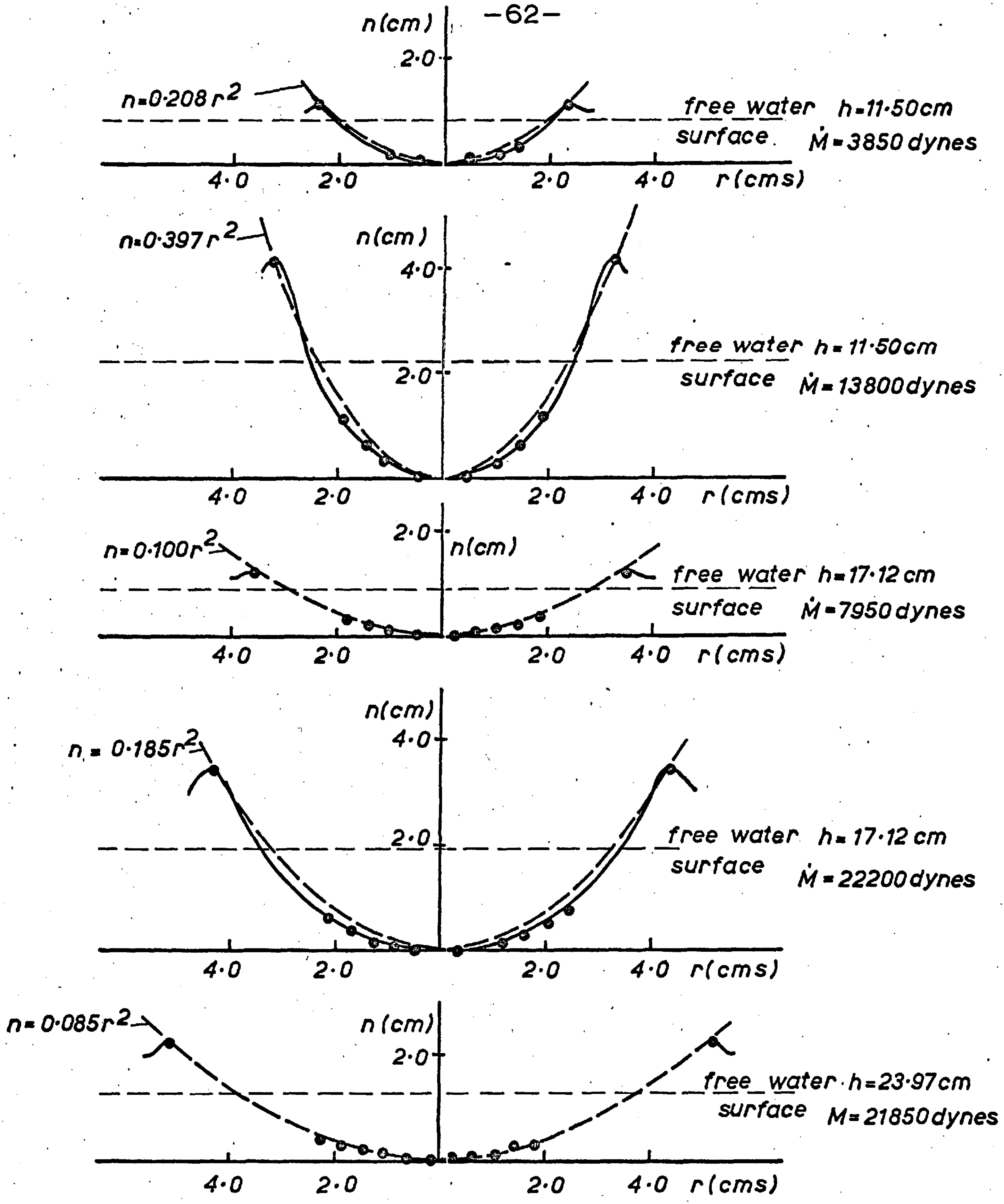

<u>FIG. 4.5-5b</u> MEASURED POINTS ON THE SECTION THROUGH THE DIAMETER OF EACH DEPRESSION, COMPARED WITH A PARABOLA FITTED TO THE CENTRE OF THE DEPRESSION AND THE TOP OF THE LIP (AIR-WATER SYSTEM)

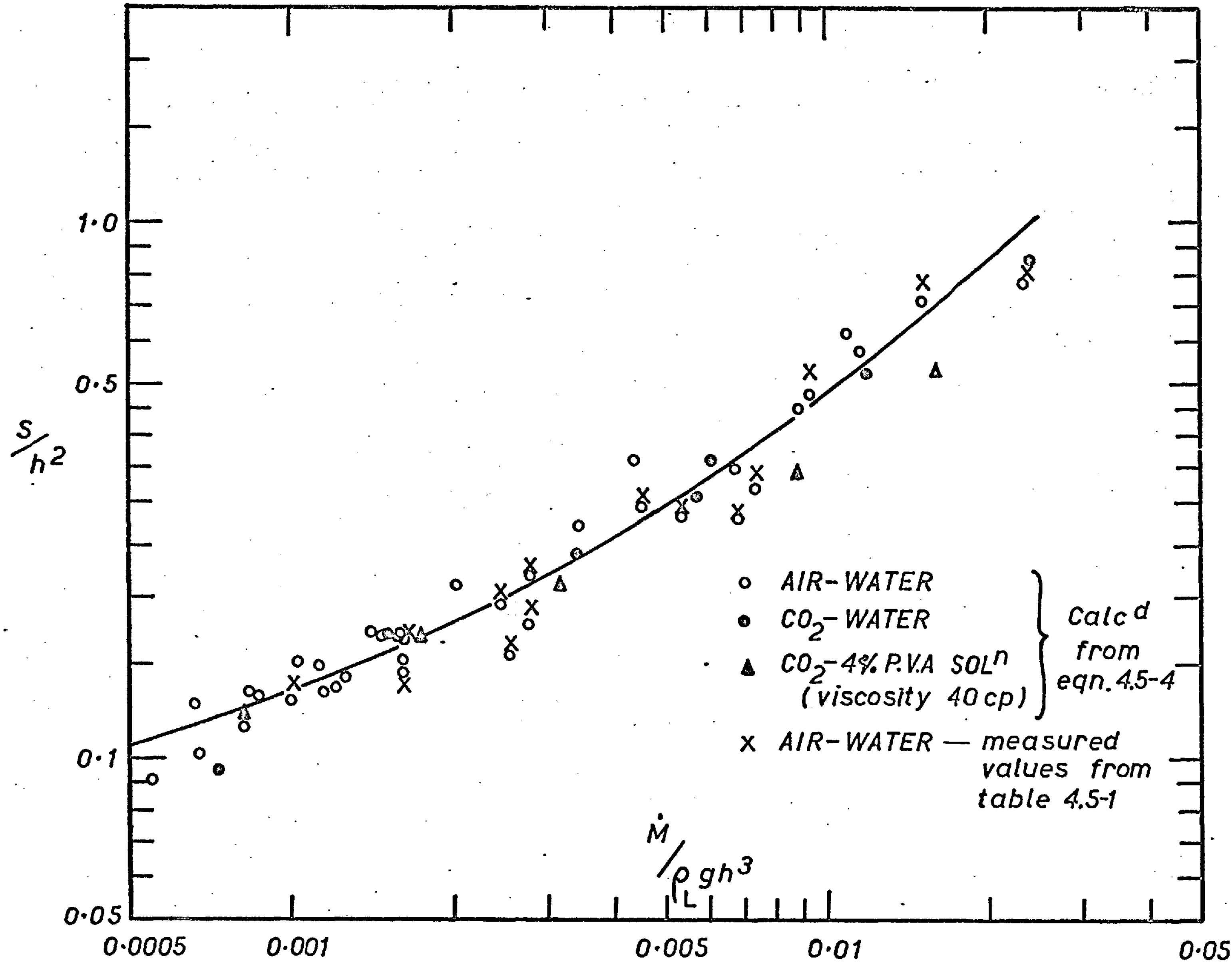

<u>FIG.4.5-6</u> VARIATION OF SURFACE AREA OF DEPRESSION S, WITH JET MOMENTUM $\dot{M}$, AND NOZZLE-LIQUID DISTANCE h, (AQUEOUS SOLUTIONS)

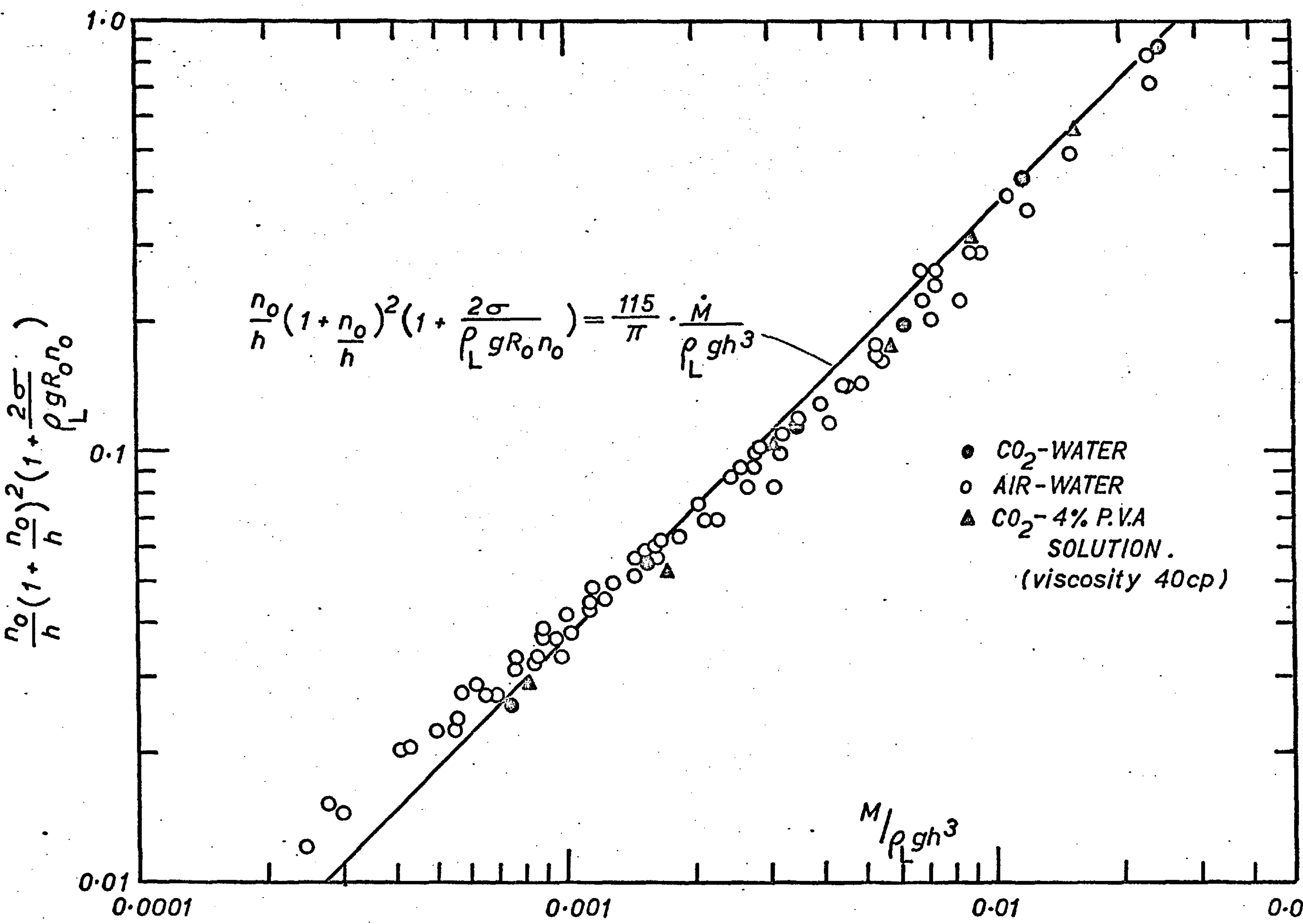

FIG. 4.5-7 VARIATION OF DEPTH OF DEPRESSION BELOW FREE LIQUID SURFACE n_o WITH JET MOMENTUM $\dot{M}$ AND NOZZLE-LIQUID DISTANCE h, INCLUDING EFFECT OF SURFACE TENSION σ (AQUEOUS SOLUTIONS)

4.6 Measurements on the Depression in Mercury

The measurements on mercury were carried out in a 30.5cm. diameter x 30.5cm. high perspex cylinder, using a probe to determine the position of the mercury surface. The probe, made from stiffened enamelled wire, .054cm. in dia. and insulated electrically, apart from its tip, was supported from a carriage which could be moved horizontally or vertically, as shown in Figure 4.6-1. When the tip was in contact with mercury, an indicator lamp in series with the probe was illuminated. Using a vernier on the scales, dimensions were measured to ± 0.005cm. In the measurement of each depression, the probe was initially positioned on the jet axis, and was then traversed across a diameter of the depression. At consecutive radii the probe was raised until the first break in contact occured. This reading was the maximum oscillation of the depression at that point. A second measurement was made, lowering the probe with the uninsulated tip above the surface, until the first contact was obtained. This reading overestimated the minimum oscillation by approx. .04cm., owing to the mercury not wetting the probe. This discrepancy was compensated for by measuring the position of the free surface in the same manner. The values of n_o are the differences between arithmetic means of the depth and surface measurements.

Both air and CO_2 were used, but some difficulty was experienced with the former, owing to the formation of an oxide skin, which had to be cleaned off frequently. Except at large blowing rates, no lip was observed in the mercury system. This was due to the combined effect of high specific gravity (13.56g./cm^3) and high surface tension (487 dynes/cm.).

Values of n_o/h and $m/_h$ are tabulated in Appendix 1 for values of $\dot{M}/\rho_L gh^3$ in the range 0.00015 to 0.04. The oscillation of the bottom of the depression was small for shallow depressions, increasing to ± 15% for $n_o = .75$cm. Owing to the absence of a marked lip, values of m were estimated to ± .05cm. from the measured profiles.

Figure 4.6-2 shows the variation of n_o/h versus $\dot{M}/\rho_L gh^3$. The solid line represents Equation 4.5-2 (neglecting surface tension), with $\beta = 115$. In general the experimental results fall within 30% below the given line.

Figure 4.6-3 shows the variation of m/h versus $\dot{M}/\rho_L gh^3$. The solid curve represents the experimental values to ± 10%.

To calculate the effect of surface tension on the depth of the depression, paraboloids of revolution were fitted to the measured cavity shapes. As there was no distinct lip, the curves were drawn through the centre of the depression and the point of inflection in the cavity wall, as shown in Figure 4.6-4. The radius of curvature at the stagnation point R_o was calculated from Equation 4.5-5. Values of R_o and $1+ 2\sigma/\rho_L g R_o n_o$ are shown in Appendix 1. The term $n_o/h\ (1+n_o/h)^2\ (1+(2\sigma/\rho_L g R_o n_o)$ is plotted in Figure 4.6-5, and the correction for surface tension improves the agreement of the experimental results with stagnation pressure analysis. The values lie within ± 10% of the line representing Equation 4.5-1 with $\beta = 115$, except the four valves for $\dot{M}/\rho_L g h^3 > .02$. This condition corresponds to nozzle throat Reynolds Number $> 1\text{x}10^4$ and $x/d < 9$. This region corresponds to the potential core of the jet (see Figure 4.4-1) and thus Equation 4.4-1 does not apply.

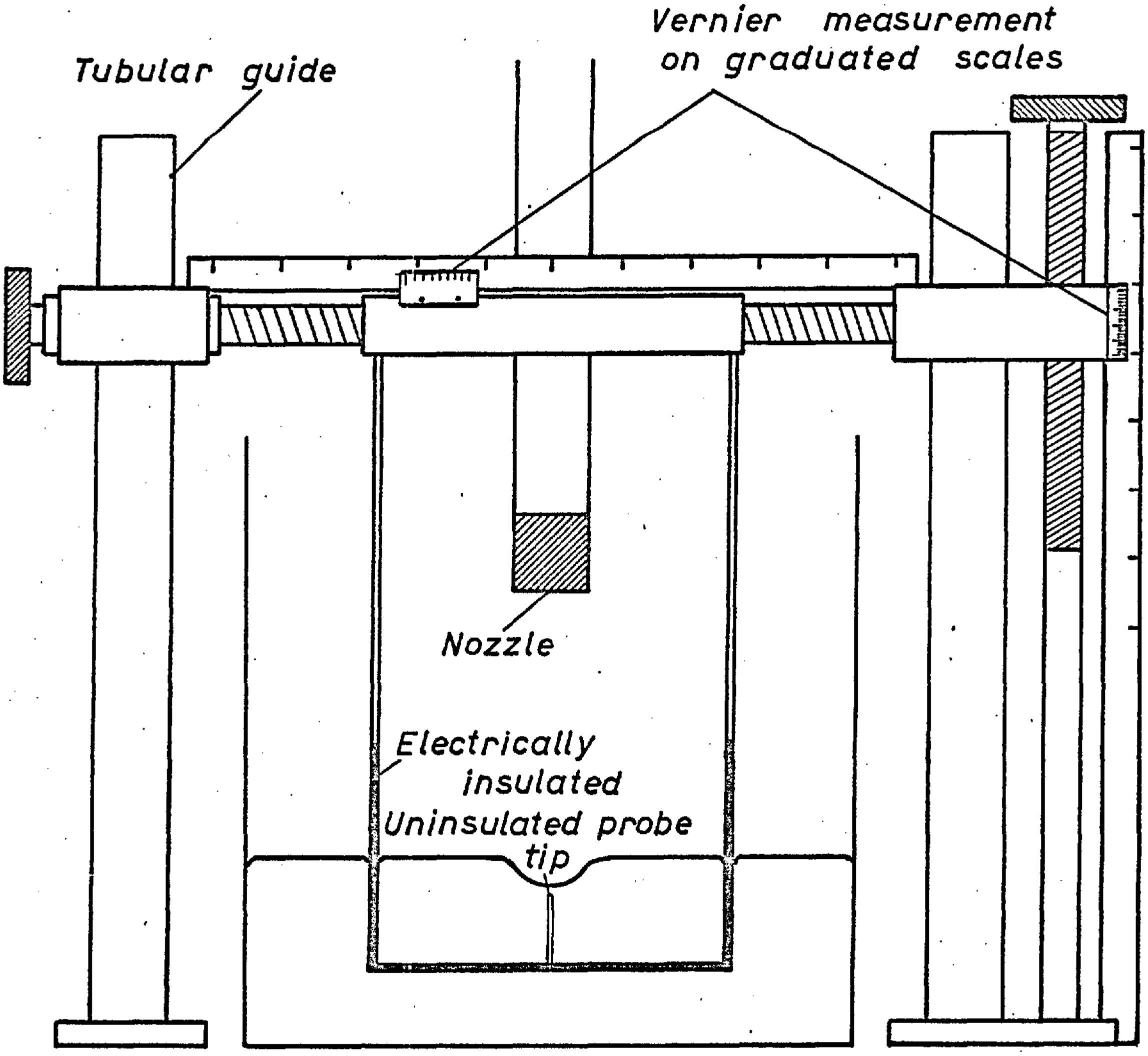

FIG. 4.6-1 PROBE TRAVERSING SYSTEM FOR MEASUREMENTS ON DEPRESSION IN MERCURY

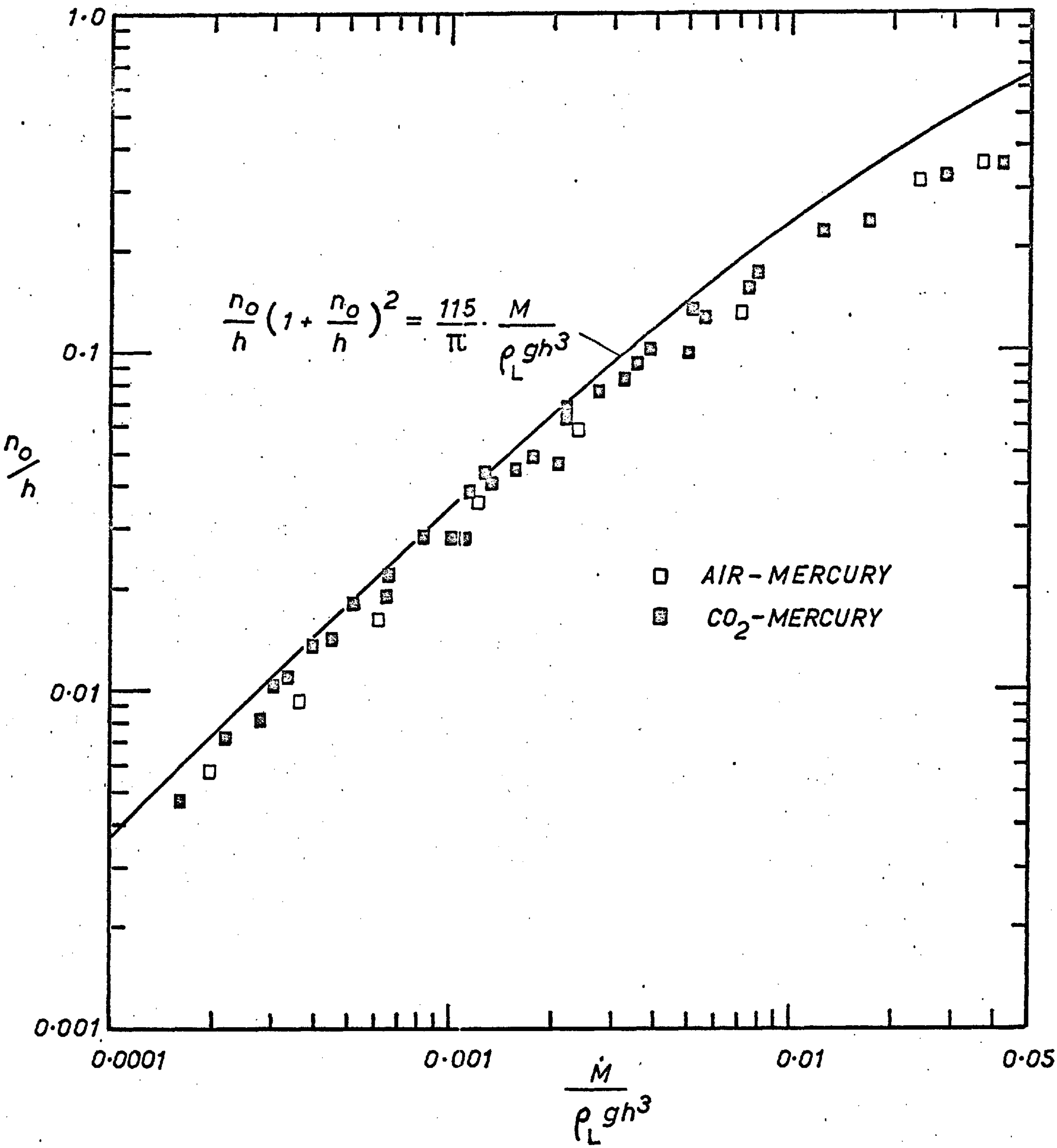

FIG. 4.6-2 VARIATION OF DEPTH OF DEPRESSION BELOW FREE LIQUID SURFACE n_o, WITH JET MOMENTUM $\dot{M}$, AND NOZZLE-LIQUID DISTANCE h, (MERCURY).

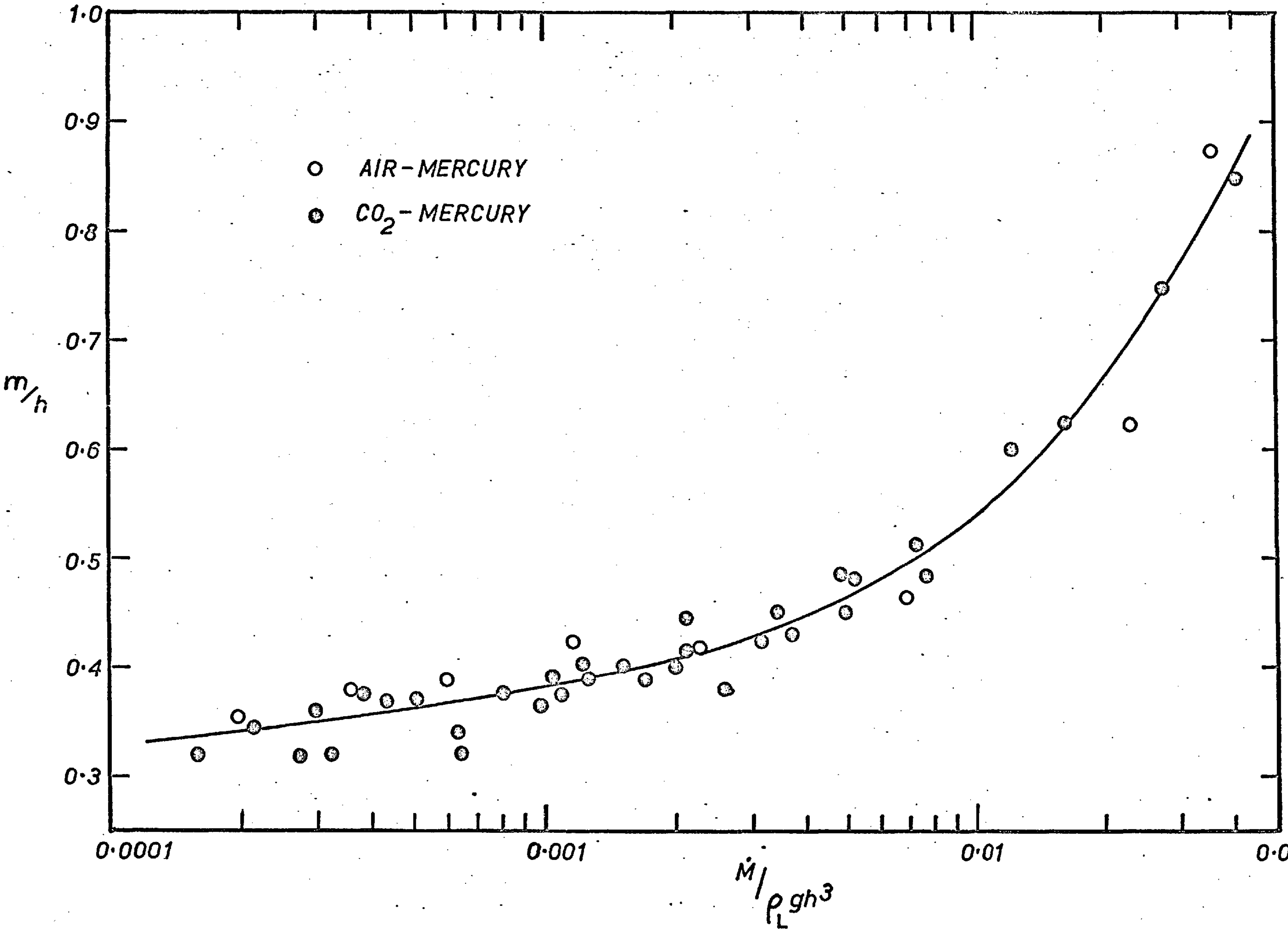

FIG.4.6-3 VARIATION OF DIAMETER OF DEPRESSION ACROSS LIP m, WITH JET MOMENTUM Ṁ AND NOZZLE-LIQUID DISTANCE h (MERCURY)

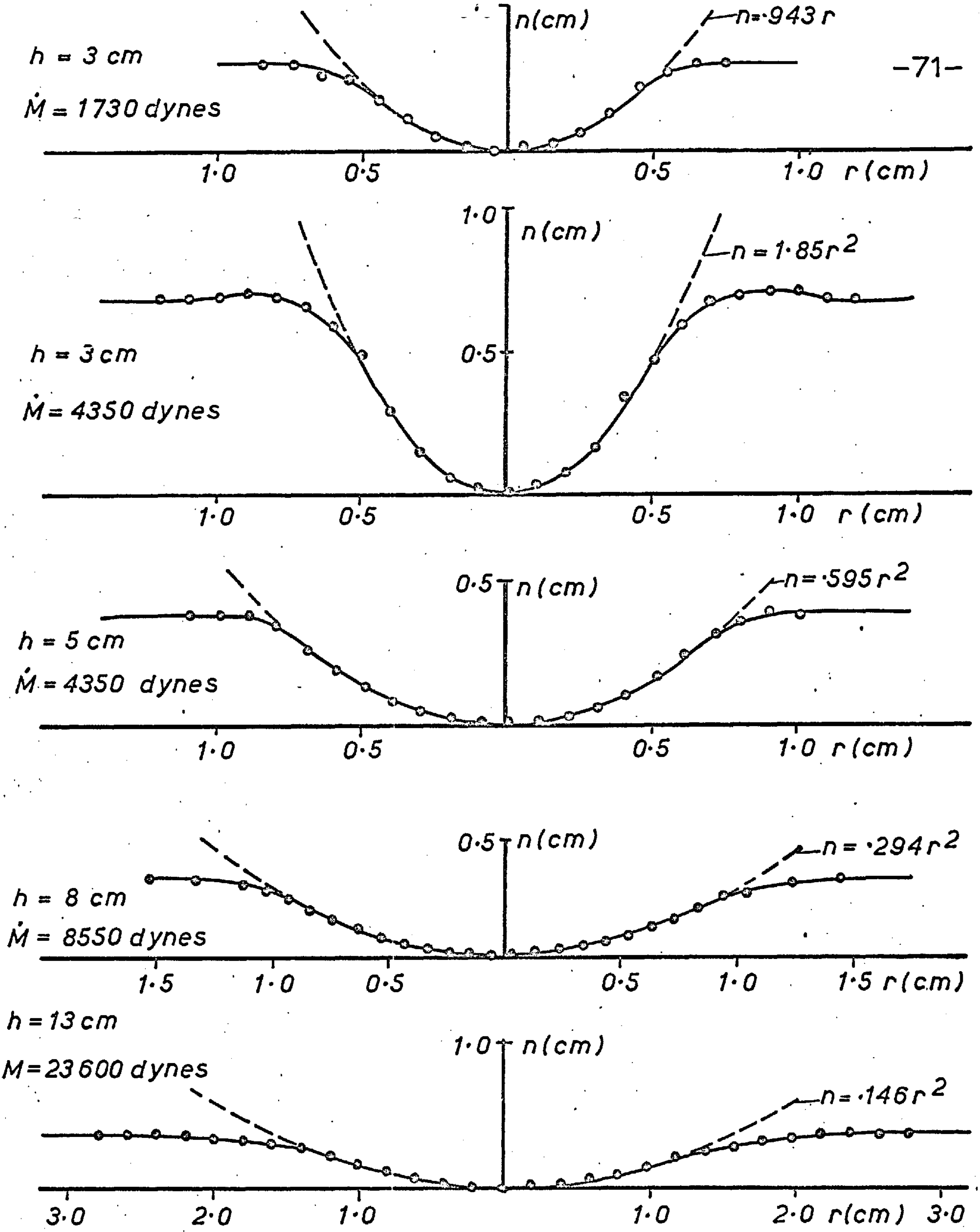

FIG.4.6-4 MEASURED POINTS ON THE SECTION THROUGH THE DIAMETER OF EACH DEPRESSION, COMPARED WITH A PARABOLA, FITTED TO THE CENTRE OF THE DEPRESSION, AND THE POINT OF INFLECTION IN THE CAVITY WALL.

(CO_2 - MERCURY SYSTEM)

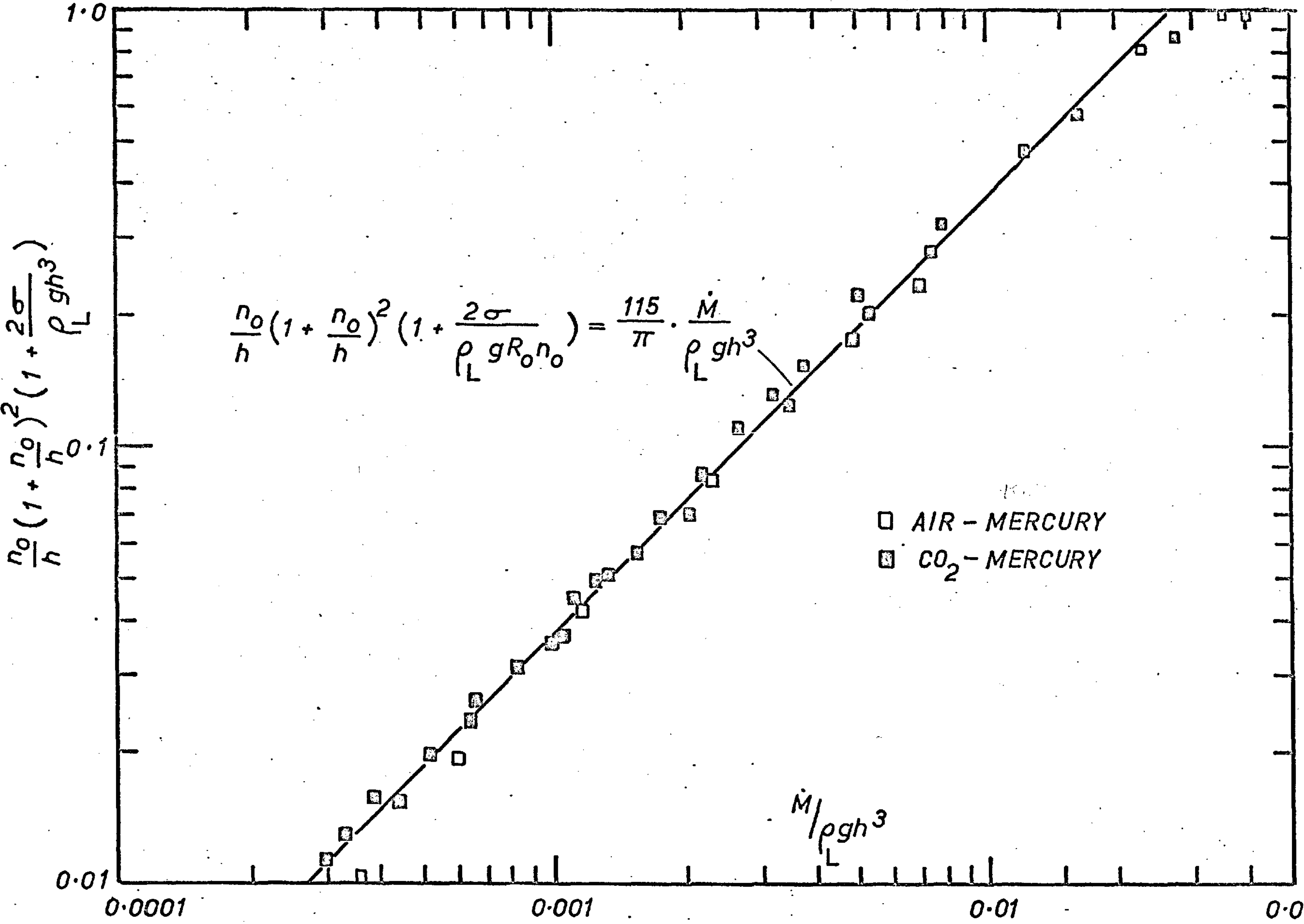

FIG. 4.6-5 VARIATION OF DEPTH OF DEPRESSION BELOW FREE LIQUID SURFACE n_o, WITH JET MOMENTUM $\dot{M}$ AND NOZZLE-LIQUID DISTANCE h, INCLUDING EFFECT OF SURFACE TENSION σ (MERCURY)

4.7 Velocities in Liquid Bath

A Bolex 16mm. cine camera was used to measure both the bulk circulation flow pattern and the liquid surface velocity, with CO_2 impinging on water in the 73cm.dia. tank. The flow patterns were observed using small (0.4cm.dia.) plastic spheres, originally denser than water, but having air bubbles inserted at their centres to bring their specific gravity as close to 1.0 as possible. Only spheres with velocities of rise or fall of less than 0.05cm./sec. in still water were acceptable. Around the tank a light-tight enclosure was made of black cloth. Using a 275 watt photoflood lamp and slit system to produce a beam of light 1.5cm. wide, the bath was illuminated along a diameter normal to the camera, which was bolted to the framework. The refraction due to the circular bath was reduced by adding 30cm. high perspex sides to the square base of the tank, and filling the intervening space with water. Movements of the plastic spheres were recorded at a speed of 12 frames per second by the camera, which was 60cm. from the illuminated plane.

Generalised circulation patterns are shown in Figures 4.7-1 and 4.7-2. Fluid from the bulk was entrained into the fast moving surface layer. A toroidal vortex was formed by fluid returning to the centre of the tank after deflection at the tank wall. A cone-shaped stagnant area existed at the bottom of the bath beneath the depression.

The change in velocity pattern with increasing momentum of the impinging jet was investigated for nozzle-water distances of h = 8.0 and 17.0cm. For a given nozzle height, the velocity of the fluid increased with increasing jet momentum. Similarly, for a fixed jet momentum, the rate of circulation increased as the height of the nozzle above the water became shorter. At the same time, however, the stagnant areas in the bath enlarged for these shorter nozzle-water distances.

Preliminary measurements of liquid surface velocities were made, using particles introduced into the jet, which were then carried radially by the surface layer. Aluminium flakes were chosen, to minimise any effect due to the particles projecting into the gas flowing across the water surface. However, difficulty was encountered with this method, as the aluminium flakes formed a ring of particles at a certain radius. Beyond this, the particles did not move radially, but circulated randomly on the surface. This radius marked the point at which the force tending to spread the particles over the whole surface was balanced by the drag due to the liquid surface velocity. Average surface velocities up to this point were measured at h = 17.0cm. for the three jet momentums shown in Figure 4.7-2, and are recorded on that figure.

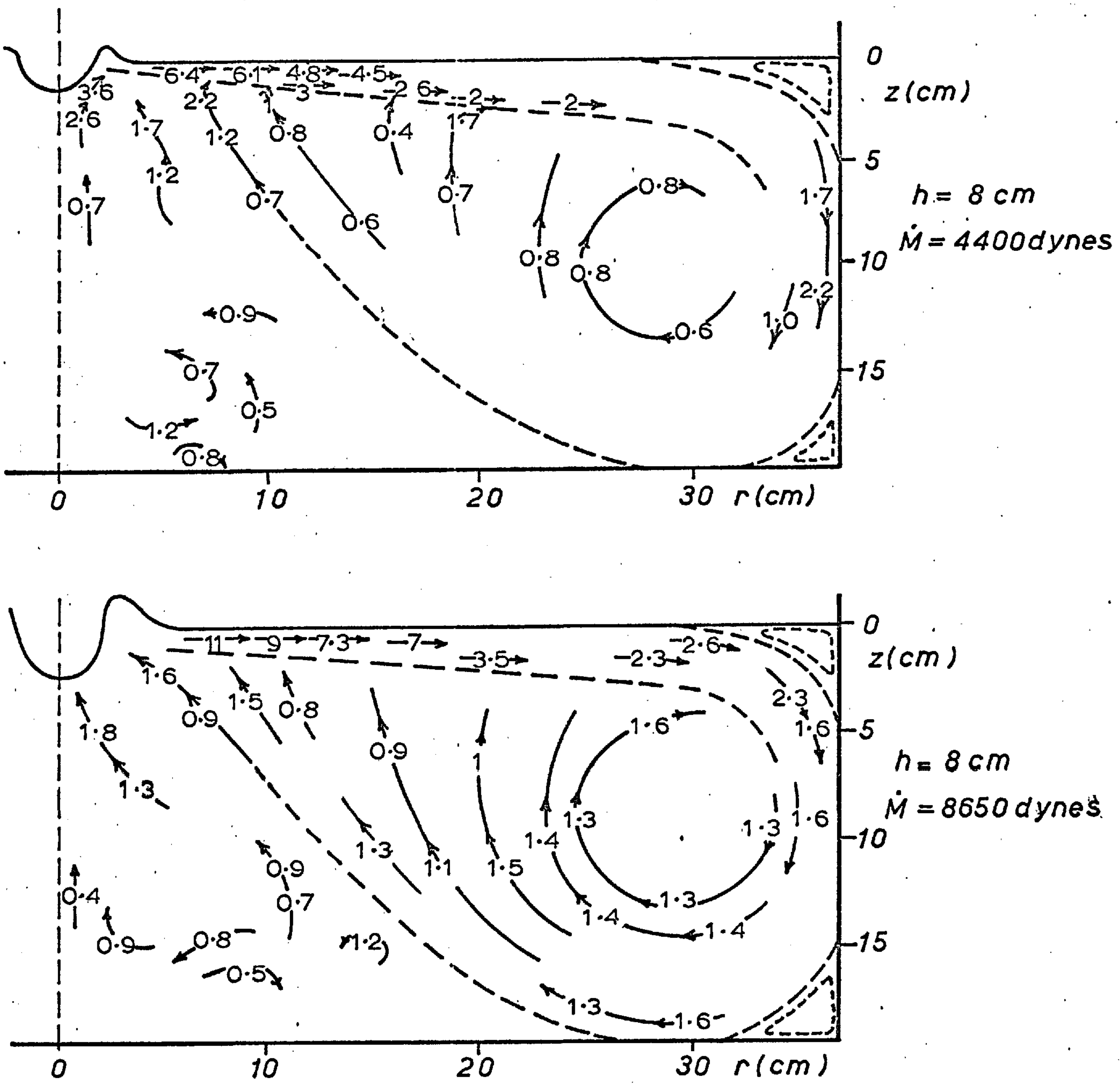

FIG. 4.7–1 MEASURED VELOCITIES ($cm.sec^{-1}$) IN BATH. CO_2– WATER SYSTEM

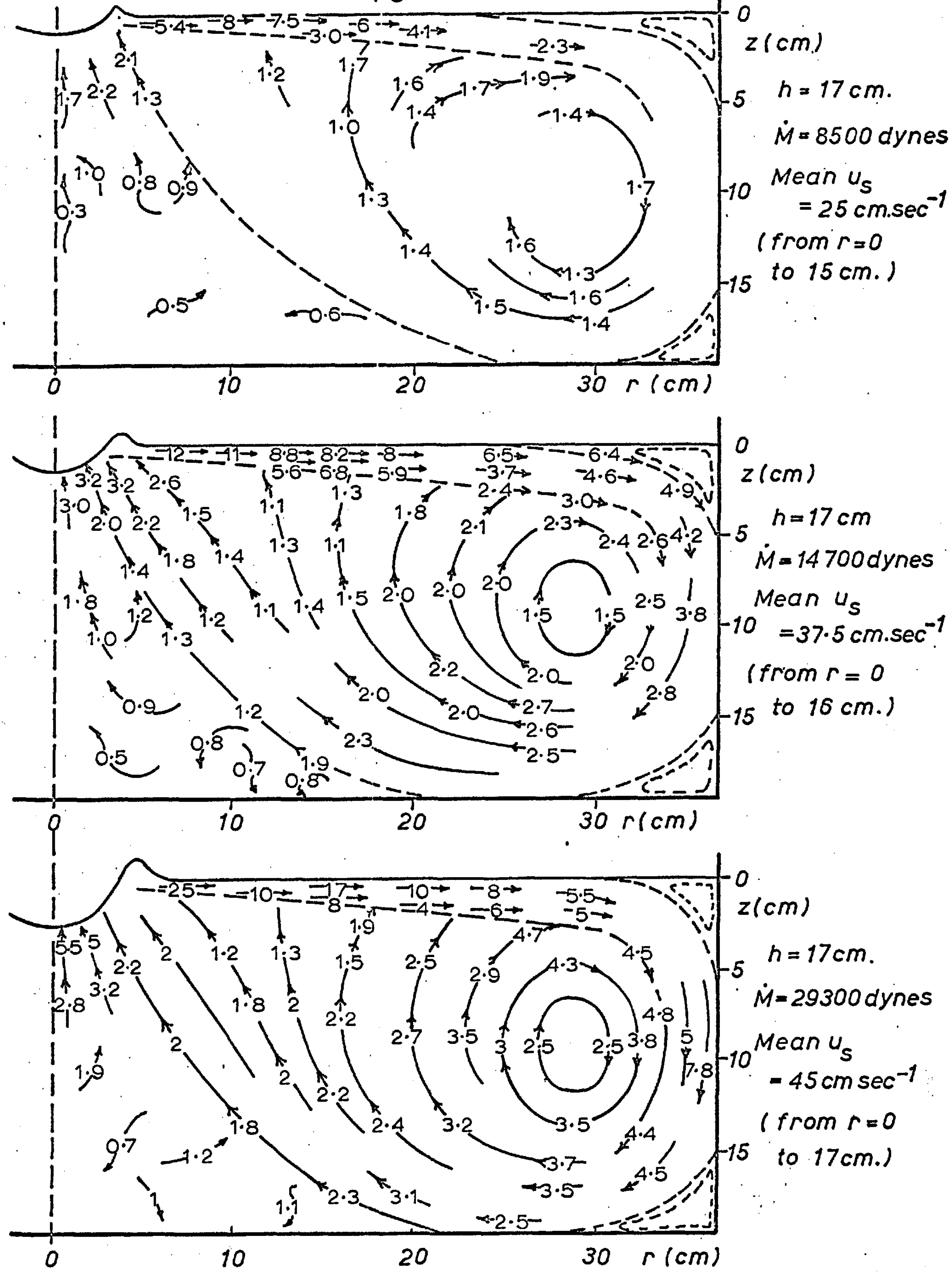

FIG. 4.7-2 MEASURED VELOCITY (cm.sec^{-1}) IN BATH CO_2 – WATER SYSTEM

4.8 Mass Transfer between the Gas Jet and Liquid Bath

Mass transfer studies were carried out by jetting carbon dioxide on to tap water and determining the rate of absorption by pH measurement. High field conductance measurements have shown[55] that only 0.37% of the carbon dioxide dissolved is present in the hydrated form, the rest remains as CO_2 molecules. However the dissociation of the hydrated form, H_2CO_3, to give hydrogen ions and bicarbonate ions provides a rapid method of determining the total CO_2 concentration in the water. A Pye Dynacap pH meter capable of discrimination down to ± .01 pH units was used, in conjunction with a calomel reference electrode and a Pye glass electrode.

Preliminary tests showed that, as the concentration of CO_2 increased from zero to saturation at one atmosphere, the pH of tap water varied from 9 to 5.3, while the variation in the pH of the distilled water available was only from 5 to 3.8. For this reason experiments were carried out using tap water. A calibration of the pH against CO_2 concentration over a range of solution temperature was first made. CO_2 was diluted with nitrogen to a predetermined CO_2 partial pressure and bubbled through tap water contained in a flask in a constant temperature bath, until a constant pH reading was obtained. Calibration curves in the range 16-22°C are shown in Appendix II.(figure A.2-1.) CO_2 concentrations were estimated from pH measurement to an accuracy of $\pm$ 0.01 x 10^{-5} moles/$cm^3 H_2O$. During the investigation regular checks on this calibration were made, but no significant change occurred.

Immediately prior to each mass transfer experiment, the CO_2 concentration in the water was reduced below 0.03 x 10^{-5} moles/$cm^3 H_2O$ by bubbling nitrogen through the bath. Blowing was then begun at predetermined values of jet height and momentum. At regular time intervals (3 or 5 minutes), 50cc. samples were taken from the liquid via the two sampling tubes situated at the points $r = 0$, $z = 6$cm and $r = 24$cm, $z = 14$cm. The sampling tube was flushed prior to taking each sample, to ensure that fresh solution was obtained for the pH measurement. All solution removed from the tank was returned through a siphon, to maintain a constant water level. The run was continued until the pH reached 5.60 (c.50% saturation), or for 100 minutes, whichever occurred first. It can be seen from the calibration curves that below a pH value of 5.60, further changes in pH with increasing concentration were small. This, coupled with decreased rates of transfer at the higher concentrations of CO_2, made it convenient to terminate experiments at this pH value.

Mass transfer rates were measured for ranges of nozzle-water distance and jet momentum. A typical graph of CO_2 concentration versus time is shown in Figure 4.8-1. The concentrations measured at the two sampling points fall on the same curve confirming that the bath was well mixed. The value of the mass transfer coefficient was obtained from a graph of the logarithm of the CO_2 content of the bulk versus time, as shown below:

$$\dot{n} = (k_L)_{mean} . A . (C^i - C^b) \quad ....4.8-1$$

where $\dot{n}$ is the rate of mass transfer to liquid (moles/sec) and is equal to $V. \, dC^b/dt$

Hence:

$$\ln \frac{C^i - C^b_t}{C^i - C^b_{t=o}} = -(k_L)_{mean} \frac{.A}{V} .t \quad ....4.8-2$$

CO_2 solution in water obeys Henry's Law, so assuming equilibrium at the interface:

$$C^i = q \, P_{co_2}$$

where q is solubility of CO_2 (moles/cm^3) at one atmosphere pressure and the given temperature P_{co_2} is taken as atmospheric pressure, less the water vapour pressure in atmospheres at the measured bath temp.

Appendix II (Figures A.2-2 and A.2-3) contains the mass transfer results, plotted in the form of Equation 4.8-2. Table A.2-1 shows mean mass transfer coefficients $(k_L)_{mean}$ derived from the slope of each plot. The variation of $(k_L)_{mean}$ with nozzle-water distance h and jet momentum $\dot{M}$ for a bath surface area of 4185 cm^2 is shown in Figure 4.8-2.

To study the effect of change in interface area without alteration of the circulation velocity pattern, 0.635cm. thick perspex rings, with an outside diameter equal to the diameter of the tank, were suspended on top of the water surface. In this way the area for mass transfer was reduced progressively from 4185 cm^2 to 2915 cm^2, 1825 cm^2 and 612 cm^2. Results were obtained for jet momentums of 14600 and 23500 dynes at nozzle-water distances of 17.1cm, 24.0cm and 33.0cm, and are presented in Appendix II, Figures A.2-4 to A.2-9, and in Table A.2-2. Under these blowing conditions, no significant effect of the rings on the movement of particles in the bath, or on the rate of bath circulation, could be detected.

To estimate transfer coefficients for the depression, the product $k_L.A$ (cm^3/sec) was plotted versus A (cm^2) in Figure 4.8-3, from the results in Table A.2-2. The values of A_d, the projected area of the depression on the undisturbed water surface, were calculated as $\pi m^2/4$, using values of m from Figure 4.5-4. The mass transfer coefficient in the depression is then $k_L. A_d/S$ where S is the true area of the concave depression, taken from Figure 4.5-6.

These estimated depression mass transfer coefficients are shown in Table 4.8-1.

Preliminary measurements on the desorption of CO_2 from tap water, using a jet of nitrogen, were carried out. Two experiments were performed, one at h = 17.1cm. and $\dot{M}$ = 14600 dynes, and the other at h = 24.0cm. and $\dot{M}$ = 23500 dynes. The results are shown in Figures A.2-10, 4.8-2 and 4.8-3, and are included on Table A.2-2.

Further preliminary experiments were also carried out for absorption of CO_2 into tap water contained in the small (30.5cm. dia.) perspex tank. With a water depth (Z) of 19.5cm the circulation pattern differed considerably from that in the large tank. The toroidal vortex no longer reached the bottom of the tank, and a stagnant area existed below. Consequently the water depth was reduced to 10cm., to ensure the circulation pattern was similar to those described in section 4.7. Two experiments at this bath depth were performed, for h = 17.1cm., and 24.0cm., each for $\dot{M}$ = 14600 dynes. These results are shown in Figures A.2-11 and 4.8-3 and are included on Table A.2-2.

Accuracy of Mass Transfer Measurements

The main uncertainty arising from the pH measurement was in the calibration , using a buffer solution, of the pH meter before each experiment. The possible inaccuracy was estimated as ± .02 pH units, which could produce a systematic error in any given experiment, resulting in an error in measured slope of the $\ln (C^i-C^b{}_t/C^i-C^b{}_{t=o})$ versus t graph of ± 6%. The estimate of the slope of the curve was accurate to ± 3%, giving a maximum error in $(k_L)_{mean}.A/V$ of ± 9%. The measurement of surface area A and bath volume V were accurate to ± 0.5%. The values of the jet momentums $\dot{M}$ recorded in Tables A.2-1 and A.2-2 are accurate to ± 200 dynes, and the values of h to ± 0.1cm.

From Figures 4.8-2 and 4.8-3 it can be seen that most of the measured transfer coefficients are represented by the mean curves to within the quoted accuracy of ± 9%. However, the mean mass transfer coefficients over the depression area estimated from Figure 4.8-3 depend on measurements from curves which are not precisely defined at the point of measurement. The accuracy of the values recorded in Table 4.8-1 is therefore not more than ± 40%, taking into account the uncertainty in the values of S quoted in section 4.5 (± 15%).

TABLE 4.8-1

Estimated mass transfer coefficients for the depression

h (cm)	$\dot{M}$(dynes) $\times 10^4$	A_d(cm^2)	S(cm^2)	$k_L \cdot A_d$ (cm^3/sec) from Fig. 4.8-3	(k_L)depression (cm./sec)
17.1	1.46	47	64	1.4	.022
"	2.35	54	87	4.0	.046
24.0	1.46	73	79	1.0	.013
"	2.35	80	98	3.0	.031
33.0	1.46	125	125	1.2	.0095
"	2.35	131	135	2.0	.015

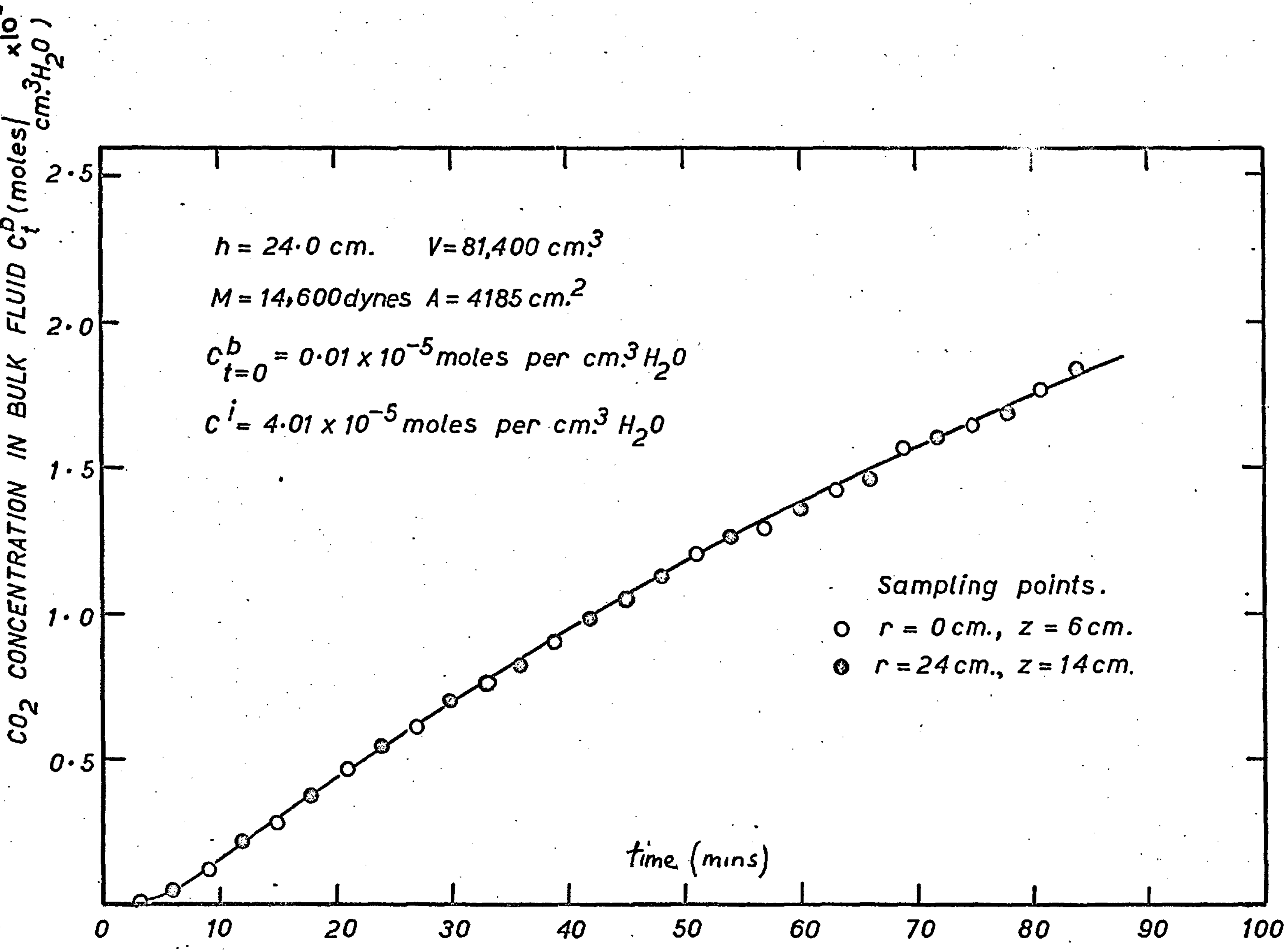

FIG. 4.8-1 VARIATION WITH TIME OF CO_2 CONCENTRATION IN BULK FLUID FOR A TYPICAL MASS TRANSFER RUN

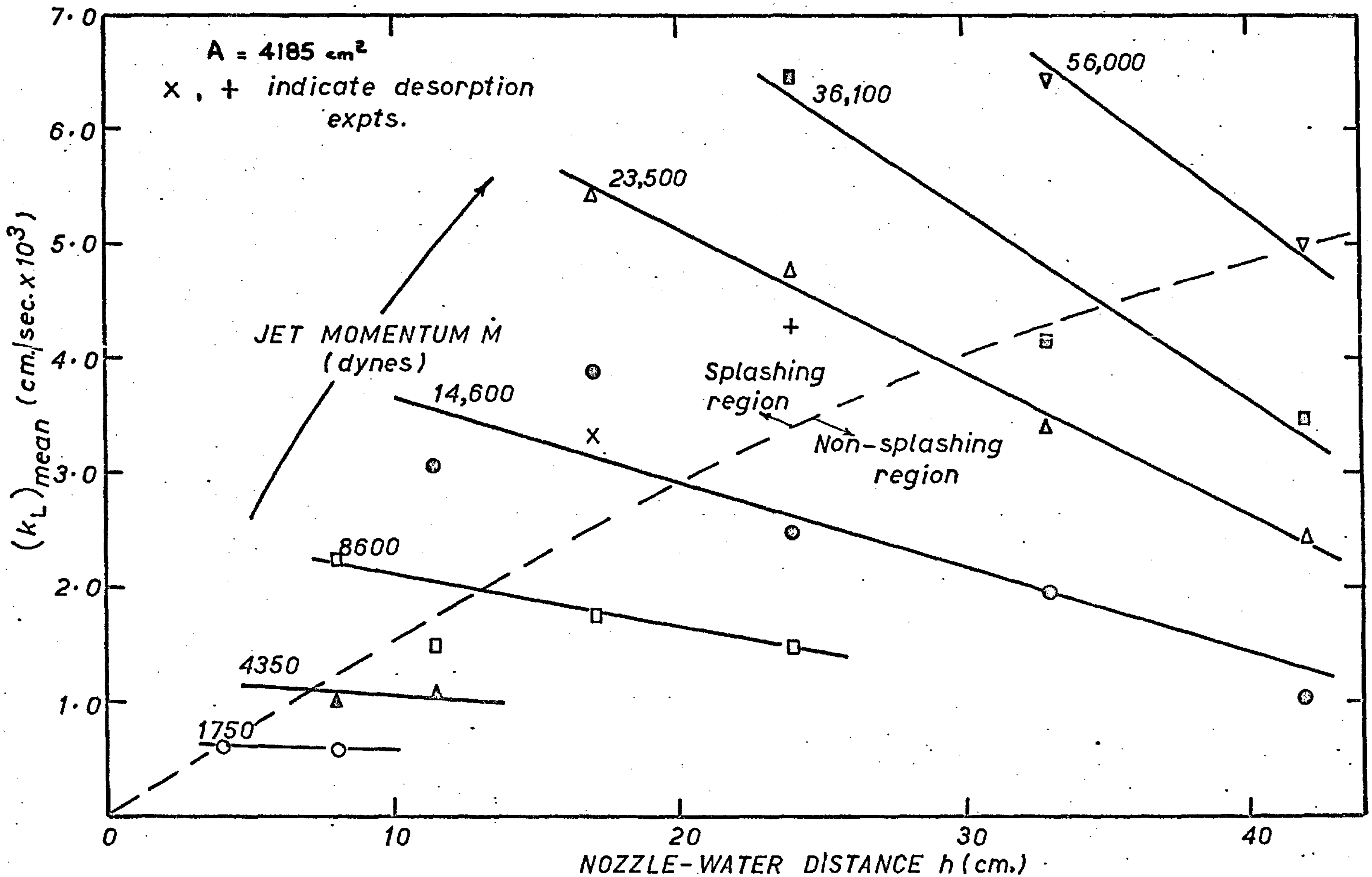

FIG. 4.8-2 VARIATION OF MEAN MASS TRANSFER COEFFICIENT, WITH NOZZLE-WATER DISTANCE, AND JET MOMENTUM

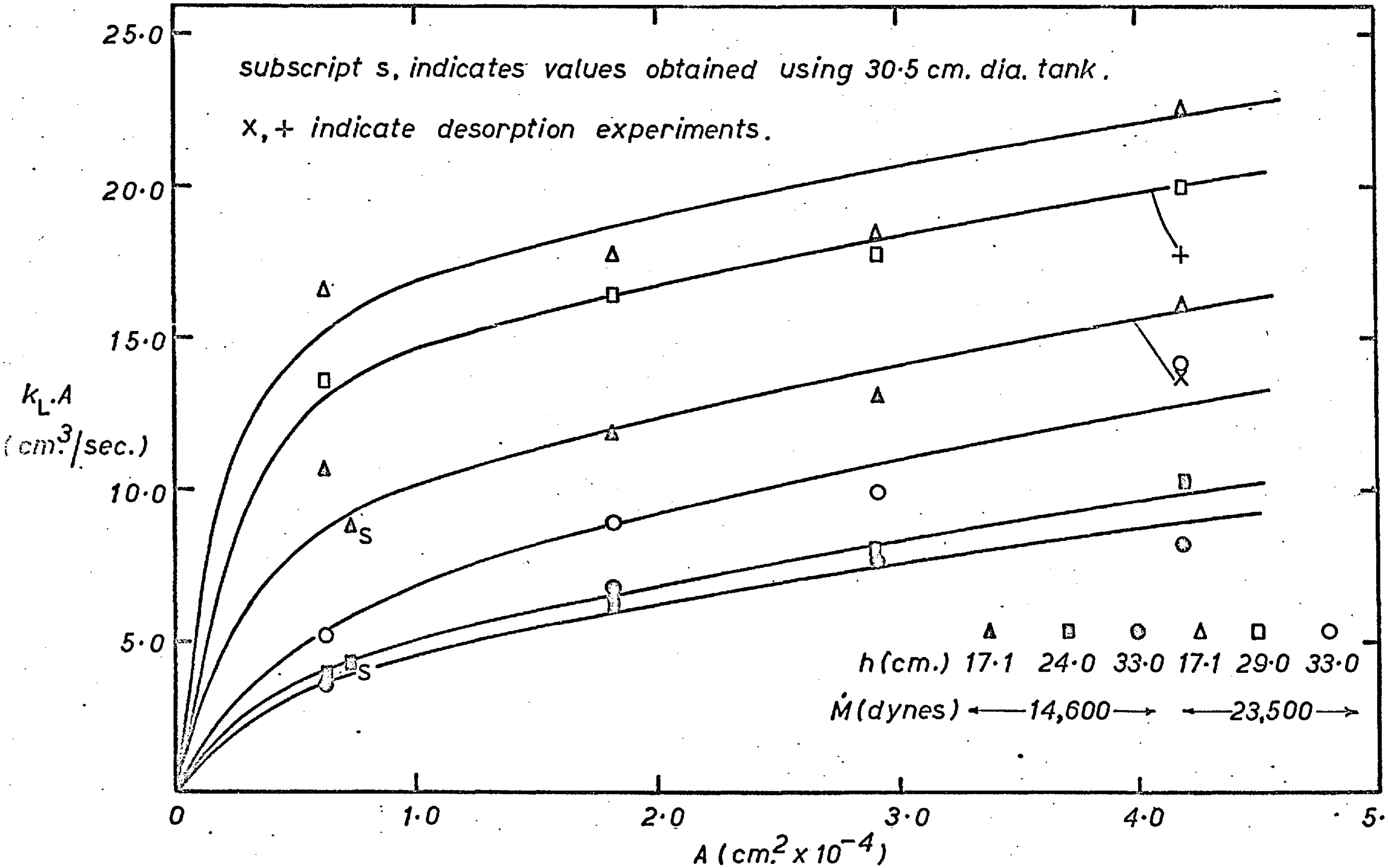

FIG. 4.8-3 VARIATION OF THE PRODUCT $k_L.A$ WITH PLANE INTERFACE AREA A, FOR ABSORPTION OF CO_2 IN TAP WATER

5.0 HIGH TEMPERATURE INVESTIGATION

The aim of the investigation was to study the effects of varying the gas flow rate and the height of the nozzle above the surface, on the rates of mass transfer between a gas jet and a molten metal surface.

The oxygen-silver system at 1000°C was chosen for the following reasons. Above the melting point of silver (960.8°C), oxygen has a high solubility without oxide formation. Data is available for oxygen solubility[56] and diffusivity[57] in silver over a range of temperature. Finally an electrochemical technique developed by Diaz, Masson and Richardson[58] enables oxygen activities to be measured continuously by probes situated at various points in the silver bath.

5.1 High Temperature Apparatus - General

To simplify the interpretation of results, it was decided to work with an isothermal system. This involved heating the oxygen upstream of the nozzle to an exit temperature of approx. 1000°C. A cylindrical lance of nimonic 75 alloy contained the electrical heating elements, and the nozzle was attached to its lower end. The main framework supported a hydraulically operated system to raise and lower the lance. The general layout of the apparatus is shown in Figures 5.1-1 and 5.1-2.

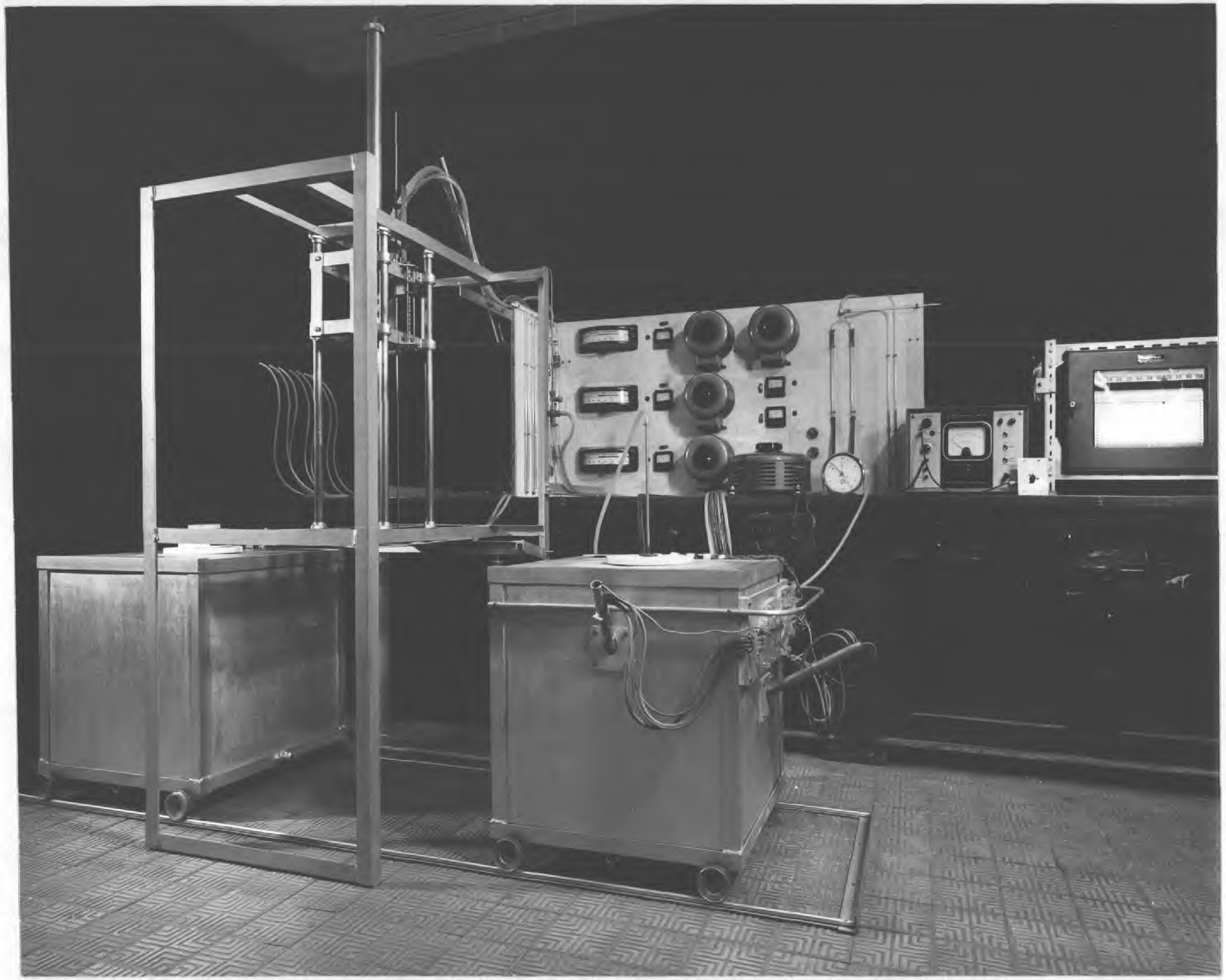

FIGURE 5.1-1 PHOTOGRAPH SHOWING GENERAL LAYOUT OF HIGH TEMPERATURE APPARATUS

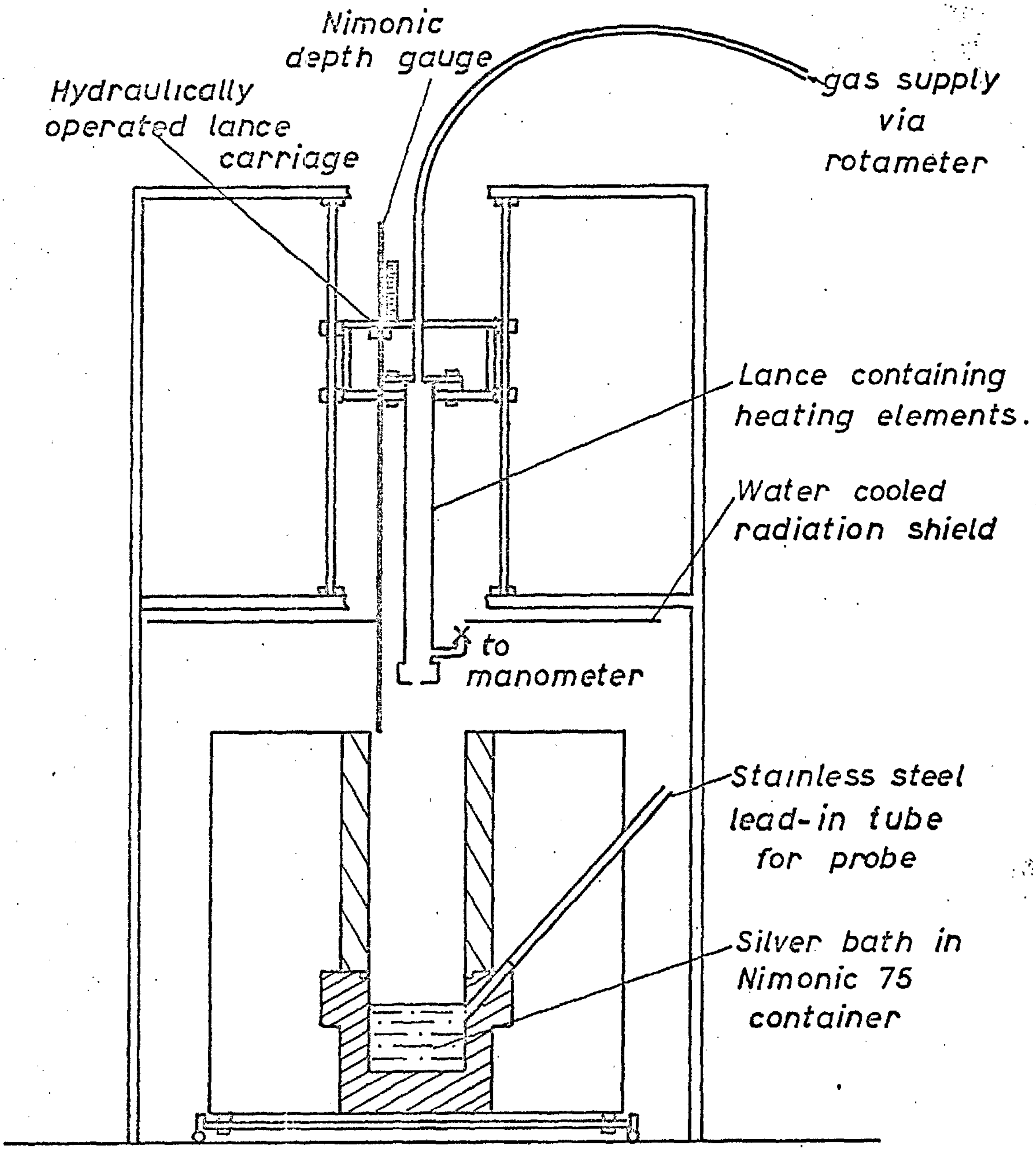

FIG. 5.1-2 GENERAL LAYOUT OF HIGH TEMPERATURE APPARATUS

Mixtures of oxygen and nitrogen were supplied from cylinders. The flows of each gas were controlled separately by needle valves and metered by rotameters before mixing.

Two moveable furnaces were used. One contained the bath of silver and oxygen probes, and the second, of identical dimensions, was used to preheat the lance. The preheating furnace enabled heating conditions in the lance to be stabilised before the beginning of each experiment.

The height of the lance above the surface of the silver was determined by the use of a moveable nimonic 75 rod. The distance between the tip of this pointer and the plane of the nozzle was indicated on a graduated scale. Contact between the pointer and the surface of the silver completed a 6 volt d.c. circuit containing an indicator light.

A secondary gas system supplied gas of predetermined oxygen partial pressure through a bubbling device. This was immersed in the silver, before each experiment, to adjust the initial concentration in the silver.

5.2 Furnace Design

The bath of molten silver (99.92% Ag), 17,500g. in weight, was contained in a pot, 15cm. diameter by 15cm., fabricated from 16 gauge nimonic 75 sheet. Details of the furnace construction are shown in Figure 5.2-1.

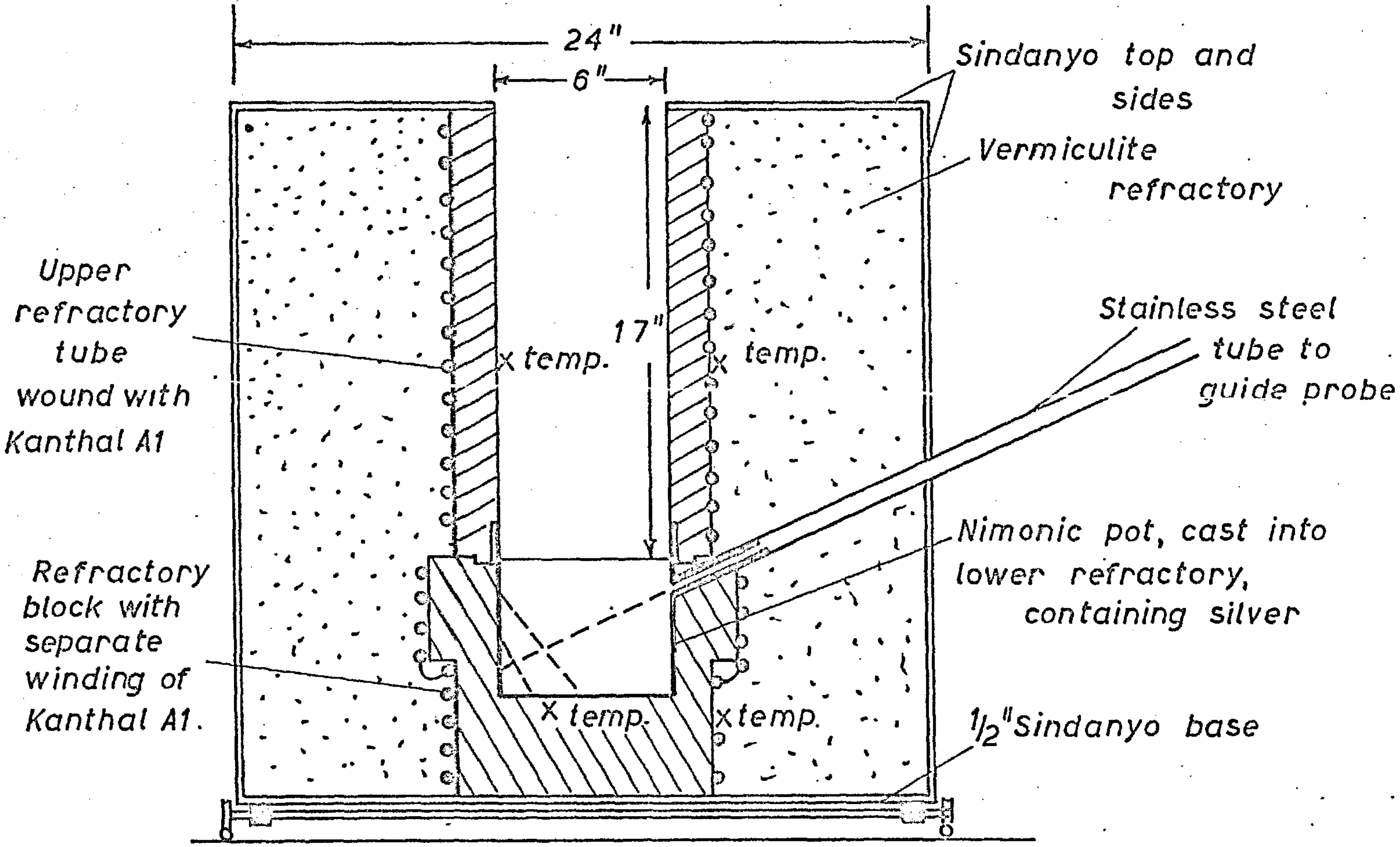

FIG.5.2-1 GENERAL FURNACE CONSTRUCTION DETAILS, SHOWING ONE OF THE PROBE GUIDE TUBES. DOTTED LINES IN SILVER BATH INDICATE PATHS OF THE THREE PROBES

The furnace was heated by two separate windings of 16s.w.g. Kanthal 'A1' wire, each connected to a separate variable transformer. The upper winding supplied 1.5 kilowatts and the lower one 1 kilowatt. The winding temperatures were indicated on Smiths proportional controllers, which operated mercury switch relays connected to additional resistances for fine temperature control ($\pm$ 5°C). Temperatures measured at the base of the pot and in the furnace atmosphere were recorded on a Honeywell Brown 6 point, 2 second print time recorder. All temperatures were measured using Platinum, ,Platinum + 13% Rhodium thermocouples.

Short nimonic tubes provided inlets through the pot wall. These fitted into stainless steel tubes, which protruded through the centres of three of the furnace sides at different heights and angles. The oxygen probes, which fitted inside these stainless steel tubes, were thus able to traverse different parts of the silver bath.

The furnace for preheating the lance was of similar dimensions, but without silver. The refractory tube was cast in one piece, the bottom being at the same level as the silver surface. A single winding supplying 2.5 kilowatts was used in the preheating furnace, otherwise the circuit was similar to the silver furnace. The temperature of the furnace atmosphere was measured and the power controlled to give the same heat transfer to the lance for a given flow rate of gas.

5.3 Lance Construction

Details of the lance construction are shown in Figure 5.3-1. The main heater for the gas consisted of a double spiral silicon carbide element. An auxilliary heater comprising of a grooved aluminous porcelain tube, wound with 22s.w.g. Kanthal 'A1' wire fitted over the upper half of the element. The two circuits were separately controlled by variable transformers. Electrical connections were made through the top of the lance by long reach glow plugs. Maximum power outputs of the auxilliary and silicon carbide heaters were 650 and 1350 watts respectively. The walls of the lance were protected from overheating on the inside by aluminous porcelain sleeves. Thermocouples were positioned to measure approximate heater temperatures.

The nimonic 75 nozzle, throat diameter .254cm., was of quadrant shaped entry section, similar to the one used in the room temperature work. It was positioned on the lance by a threaded cap, which tightened the nozzle disc against a 'Fiberfrax' (alumina-silica fibre) seal.

5.4 Exit Gas Temperature Measurement

The power required by the lance depended on its depth of penetration within the furnace. Preliminary temperature measurement and control were carried out in the preheating furnace. A special pyrometer used to measure the gas temperature contained two

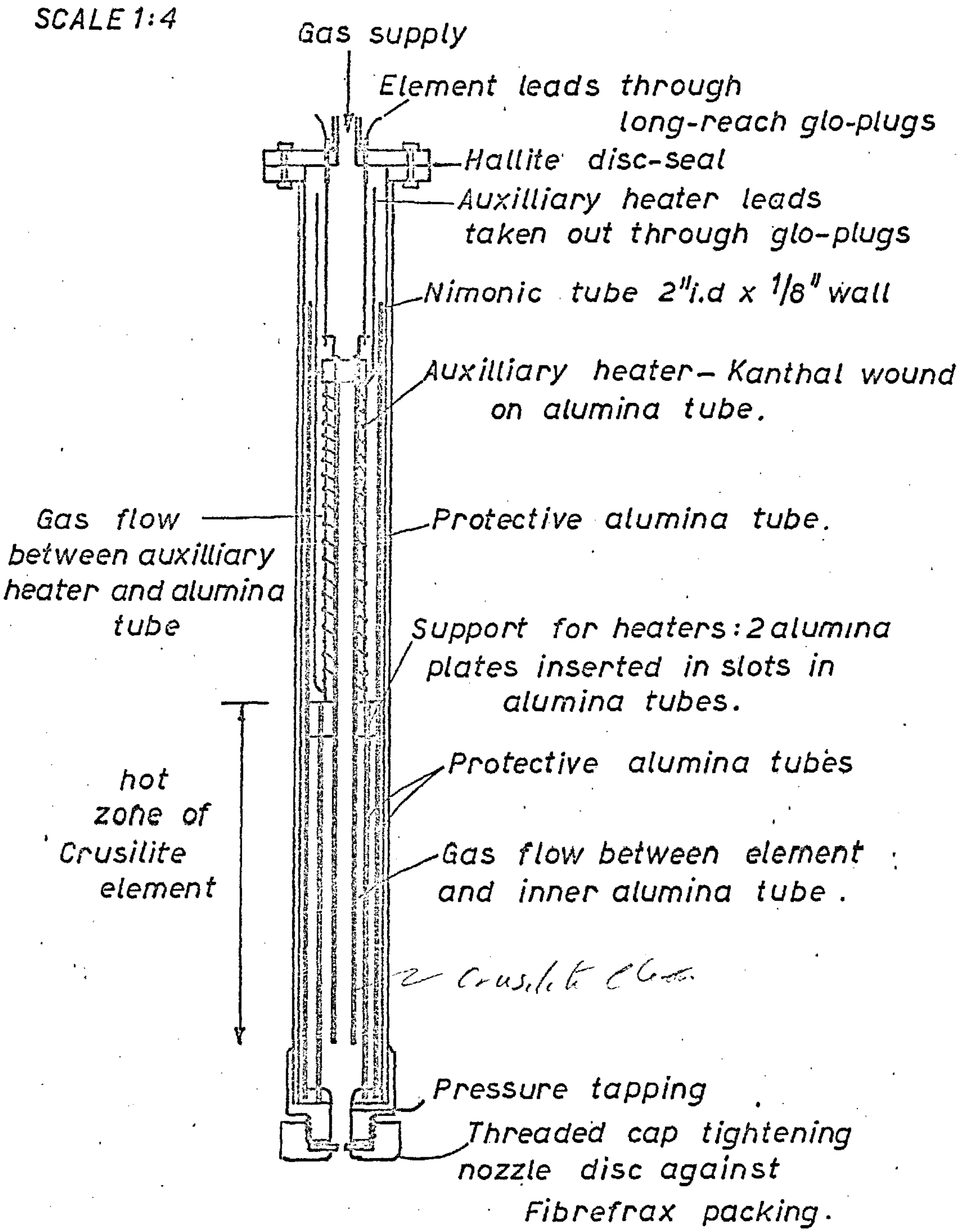

FIG.5.3-1 DETAILS OF LANCE CONSTRUCTION

thermocouples (Pt/Pt+13%.Rh), which were situated at the mid- points of adjacent, horizontal alumina tubes (1 cm.dia. x 7.5 cm. long), each with closed ends. One of the tubes, which was situated directly below the nozzle, had two 7 mm. holes, one in the upper surface, and the other in the lower surface at the opposite end of the tube. The thermocouple bead was thus exposed to the entire gas jet before appreciable entrainment could occur. At the same time it was shielded from direct radiation from both the lance and the furnace. The input to the lance heaters was adjusted until the thermocouple exposed to the jet reached the same temperature as the furnace atmosphere, which was indicated by the adjacent couple.

5.5 Oxygen Analysis Probes

The oxygen analysis probes employed lime stabilised zirconia tubes (15 mole % CaO), which contained the reference silver-oxygen electrode at the tip. The background theory to the use of this system is presented in Appendix III.

Details of the probe holder design are shown in Figure 5.5-1. The end of the zirconia tube, after first silver and then copper plating, was connected to the holder by means of a water cooled soldered joint. Oxygen was passed down the centre alumina tube to maintain an atmosphere of oxygen over the small pellet of "fine" grade silver (99.92%Ag) at the tip.

Electrical contact with the reference side of the cell and with the silver bath was made by means of stainless steel* wire 0.046cm.

SCALE 1:1 (apart from sectioning)

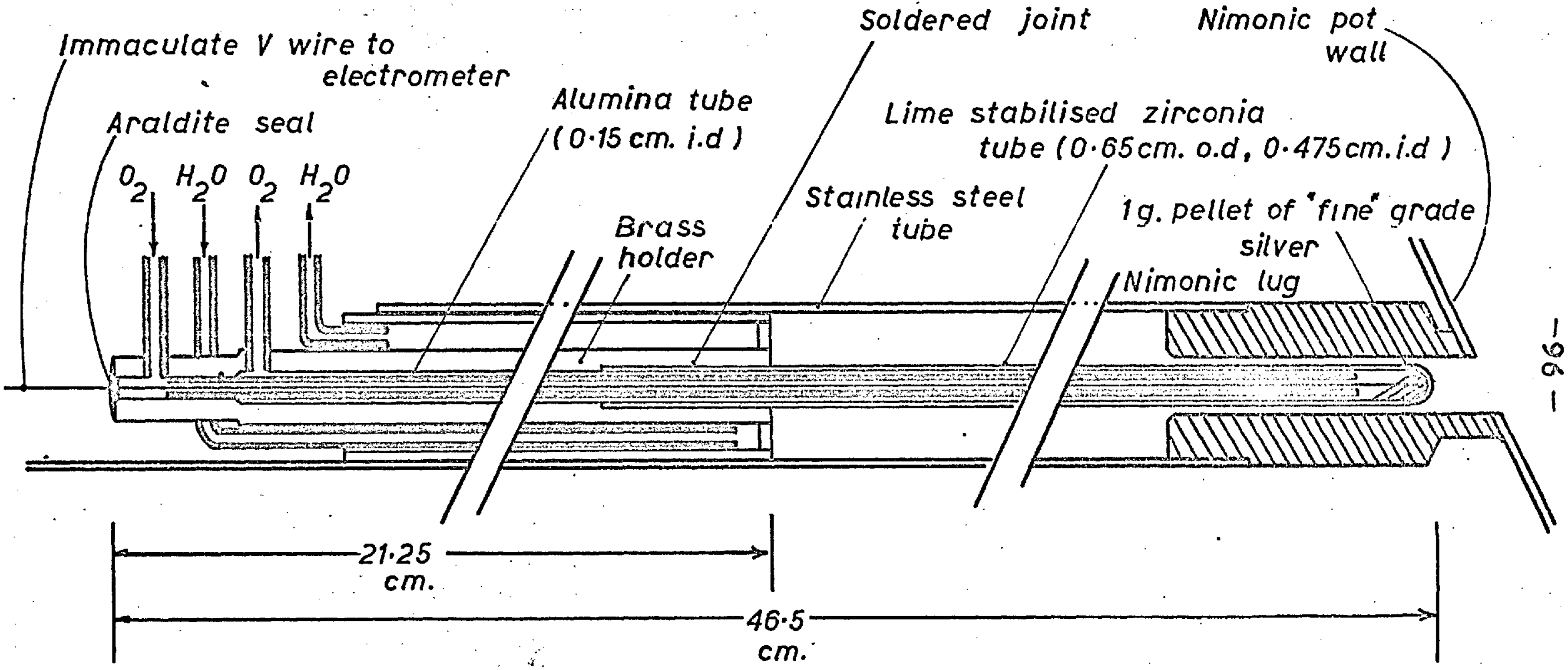

FIG.5.5-1 SECTIONED VIEW OF THE STABILISED ZIRCONIA PROBE AND WATER COOLED PROBE-HOLDER

dia. A Vibron 33B-2 Electrometer was used to measure the emf of each cell, with the silver bath connected to the electrometer via shielded leads and a coaxial switch.

5.6 Measurements on Nozzle

The pressure drop across the nozzle was measured at room temperature for a given flow rate, calculated from the rotameter reading and the gas temperature and pressure in the meter. The coefficient of discharge of the nozzle was calculated as described in section 4.3. The momentum of jet was also measured, by the impingement method described in that section. Figure 5.6-1 shows the variation of Cd, and measured and calculated momentum, with mass flow rate. The diameter of the nozzle, which had been measured using a vernier microscope showed no signs of wear at the end of the investigation. This is confirmed by final determination of Cd and momentum of jet, which are also shown in Figure 5.6-1.

In the high temperature experiments, the increase in nozzle diameter was calculated using a coefficient of linear expansion of 17.3×10^{-6} per °C for the nimonic alloy. For each flow rate, the throat Reynolds Number was calculated and a value of Cd obtained from Figure 5.6-1.

---

* Immaculate V. (. 12C, 1.3Si, .8Mn, 23.5Cr, 21.5Ni)

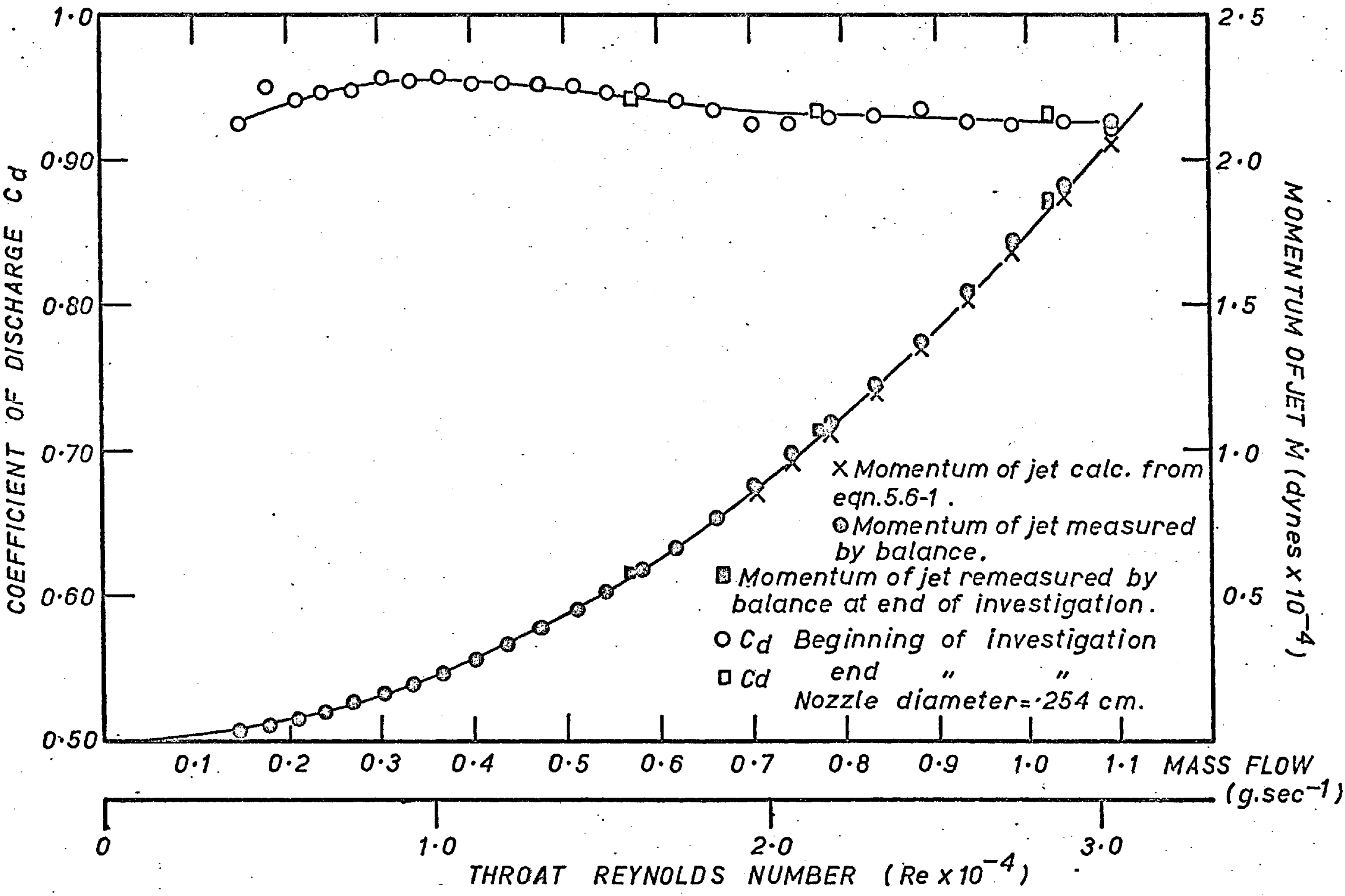

FIG. 5.6-1 MOMENTUM OF JET, MEASURED AND CALCULATED FROM EQUATION 5.6-1, AND MEASURED VALUES OF Cd FOR OXYGEN.

The momentum of jet $\dot{M}$ for this flow rate $\dot{m}$ was then calculated as follows :

$$\dot{M} = \dot{m} \; V_J$$

hence: $$\dot{M} = C_d \, \rho_2 \, a_2 \, V_J^{\,2}$$

now:
$$V_J = \left[\frac{\dfrac{2\gamma}{\gamma-1} \cdot \dfrac{P_2}{\rho_2} \left\{ \left(\dfrac{P_1}{P_2}\right)^{\frac{\gamma-1}{\gamma}} - 1 \right\}}{1 - \left(\dfrac{\rho_2}{\rho_1} \cdot \dfrac{a_2}{a_1} \right)^2} \right]^{1/2}$$

thus:
$$\dot{M} = C_d a_2 \left[\frac{\dfrac{2\gamma}{\gamma-1} \cdot \dfrac{P_2}{\;} \left\{ \left(\dfrac{P_1}{P_2}\right)^{\frac{\gamma-1}{\gamma}} - 1 \right\}}{1 - \left\{ \left(\dfrac{P_2}{P_1}\right)^{\frac{1}{\gamma}} \cdot \dfrac{a_2}{a_1} \right\}^2} \right] \quad \text{.....5.6-1}$$

Using this value of $\dot{M}$ and the measured flow rate $\dot{m}$, the exit density ρ_2 and velocity V_J were calculated. The values of exit gas temperature shown in results section 5.8 were deduced from ρ_2.

5.7 Experimental Procedure for Mass Transfer Work

At the beginning of each run, the preheating furnace was positioned centrally beneath the lance. The lance, with exit gas pyrometer attached, was lowered in to the required depth. Concurrently, the surface of the silver was cleaned to mirror brightness using a nimonic rod. The bubbler was then immersed in the bath and oxygen free nitrogen was introduced, with a secondary stream of the same gas to purge the furnace atmosphere. By bubbling at 500 mls. per minute for 1 hour, the partial pressure of oxygen in the silver could be reduced to **0.5** atmospheres (5.37×10^{-5} moles/cm^3 of O_2).

After connecting the water and oxygen supplies the probes were then introduced very slowly into the silver bath to minimise thermal shock.

The requisite gas flow was passed through the nozzle and the power to the heaters adjusted until the gas was at the required temperature. The lance was raised from the preheating furnace and then lowered into the silver furnace which had been moved into position. The height indicator had been preset, and when electrical contact with the surface of the silver was made by the rod, the lance was correctly positioned.

During lance transfer, the gas supply was cut off and the current increased to reduce lance cooling. Subsequently the current through each internal heater was readjusted, and when the temperatures inside the lance reached their previous values, the gas flow was turned on. The emf produced by each probe was noted at 1 minute intervals.

In a number of runs, gas with a partial pressure of 0.2 atmospheres of oxygen was used. When the silver reached an oxygen pressure of c. 0.17 atmospheres, the gas composition was changed to pure oxygen, without changing the total momentum of jet. Blowing was continued until the oxygen pressure in the silver reached 0.8 to 0.9 atmospheres. Finally oxygen was desorbed from the silver, by again blowing gas with a partial pressure of 0.2 atmospheres of oxygen, until the partial pressure was reduced to c. 0.3 atmospheres. In the remaining runs only pure oxygen was used.

Initially, experiments were also made to measure desorption rates from the silver containing c.0.3 atmospheres of oxygen, by blowing with a jet of oxygen-free nitrogen. This resulted in the presence of a skin at the interface, which inhibited mass transfer. Analysis showed this to be a mixture of silicon and silica, doubtless formed from the silicon carbide element. At temperatures in excess of 1400°C in an oxygen-rich atmosphere, the element "aged" and became coated with a layer of silica. Subsequent reduction of the oxygen pressure to a low value (10^{-5}atm) at these high temperatures resulted in the formation of gaseous silicon monoxide[59]. Expansion through the nozzle cooled the gas, and the silicon monoxide disproportionated into silicon and silica:

$$2\ SiO \longrightarrow Si + SiO_2$$

Consequently further use of oxygen-free nitrogen was not attempted.

A number of experimental difficulties were encountered, notably in the operation of the probes. These were very susceptible to thermal shock and to jamming in the nimonic lugs on the silver container. To minimise oxygen transfer across the gas-metal interface in the lugs, only a small clearance was allowed between the probe and lug. Too rapid withdrawal of a probe resulted in silver coming into contact with the cooler stainless steel tube, where it froze and jammed the probe. Attempts to free this invariably resulted in its fracture.

5.8 Mass Transfer Results

Initial mass transfer studies were conducted using one probe immersed in the bath. Preliminary results obtained with lance heights of 10cm. and jet momentums up to 20,000 dynes indicated poor mixing of the silver. Instead of a gradual variation with time, the oxygen pressure at a fixed position changed sharply, followed by periods when it remained almost constant with time. Such a curve is shown in Figure 5.8-1.

In subsequent experiments, traverses with the probe across the full diameter of the bath revealed marked local variations in the oxygen pressure, and the presence of an oxygen rich stream flowing from the liquid surface adjacent to the wall. The width of the stream was approximately 0.5cm. This flow pattern suggested that the stirring action of the oxygen jet was similar to that encountered in the low temperature investigation.

Later studies of the degree of mixing, with additional probes situated at different positions in the bath, showed that effective circulation only occurred when the jet momentum was in excess of 20,000 dynes, with lance heights less than 10cm. When the nozzle-silver distance was larger, greater jet momentums were required. Figure 5.8-2 shows the result of a mixing experiment.

The rates of mass transfer were interpreted using expressions similar to those in section 4.8. In this case, the diatomic oxygen molecules are absorbed into silver in the form of atoms.

Thus: $$\dot{n}_o = (k_L)_{mean} \; A \, (C_o^i - C_o^b) \qquad .... \; 5.8\text{-}1$$

where $\dot{n}_o$ is the rate of transfer of oxygen atomsacross the interface (g.atoms/sec) and equals $V.dC_o^b/dt$

Hence:
$$\ln \left(\frac{C_o^i - (C_o^b)_t}{C_o^i - (C_o^b)_{t=o}} \right) = - \, (k_L)_{mean} . \; \frac{A}{V} \; .t$$

Oxygen dissolution in silver follows Sierverts Law:[58,60]

$$C_o = q \sqrt{P_{o_2}}$$

where q is the solubility of O at one atmosphere pressure and the given temperature (g.atoms of O/cm^3 per atmos.$^{1/2}$)

If equilibrium exists at the interface:

$C_o^i = q \sqrt{P_{o_2}^g}$ where $P_{o_2}^g$ is the partial pressure of oxygen in the impinging jet(atmos)

and $C_o^b = q \sqrt{P_{o_2}^b}$ where $P_{o_2}^b$ is the partial pressure of oxygen measured by the probe (atmos)

Thus:

$$\ln \left(\frac{\sqrt{P_{O_2}^{\,g}} - \left(\sqrt{P_{O_2}^{\,b}}\right)_t}{\sqrt{P_{O_2}^{\,g}} - \left(\sqrt{P_{O_2}^{\,b}}\right)_{t=o}} \right) = -(k_L)_{mean} \cdot \frac{A}{V} \cdot t \quad \ldots .\ 5.8\text{-}2$$

Results for absorption and desorption in the form of Equation 5.8-2 for jet momentums in excess of 20,000 dynes are presented in Appendix III.

An initial study was made of the effect of the interface surface area on rates of transfer, on the lines of the room temperature investigation. "Fiberfrax" alumina-silica fibre rings, .635cm. thick, were placed on the surface of the bath, and rates of oxygen transfer were measured with the interface area reduced from 182 cm^2 to 91 cm^2, and to 45 cm^2. Only one series of experiments, at h = 10.5cm and $\dot{M}$ = 56,500 dynes, gave useful results (Appendix III). At smaller jet momentums, or larger values of h, the circulation was again inadequate to cause mixing, on which the analysis of results depends.

The exit gas temperatures, calculated as described on page 99, were generally low, being 950°C for jet momentums up to 20,000 dynes, down to 860°C for jet momentums of 56,000 dynes. A more accurate method of temperature control may be desirable in future work, if this parameter proves to be important.

The accuracy of the height measurement was estimated as ± 0.1cm., allowance being made for the expansion of the nimonic height gauge. The variation in the momentum of the jet was accurate to ± 4% over each series of experiments. The accuracy of the mass transfer coefficient determination was approx. ± 10% for the slope measurement. Coefficients for absorption and desorption experiments with $P_{o_2}^{g}$ = 0.2 atmos. agreed to ± 15%. However coefficients for $P_{o_2}^{g}$ = 1 atmos. were up to 25% higher than for $P_{o_2}^{g}$ = 0.2 atmos, at the same jet momentum.

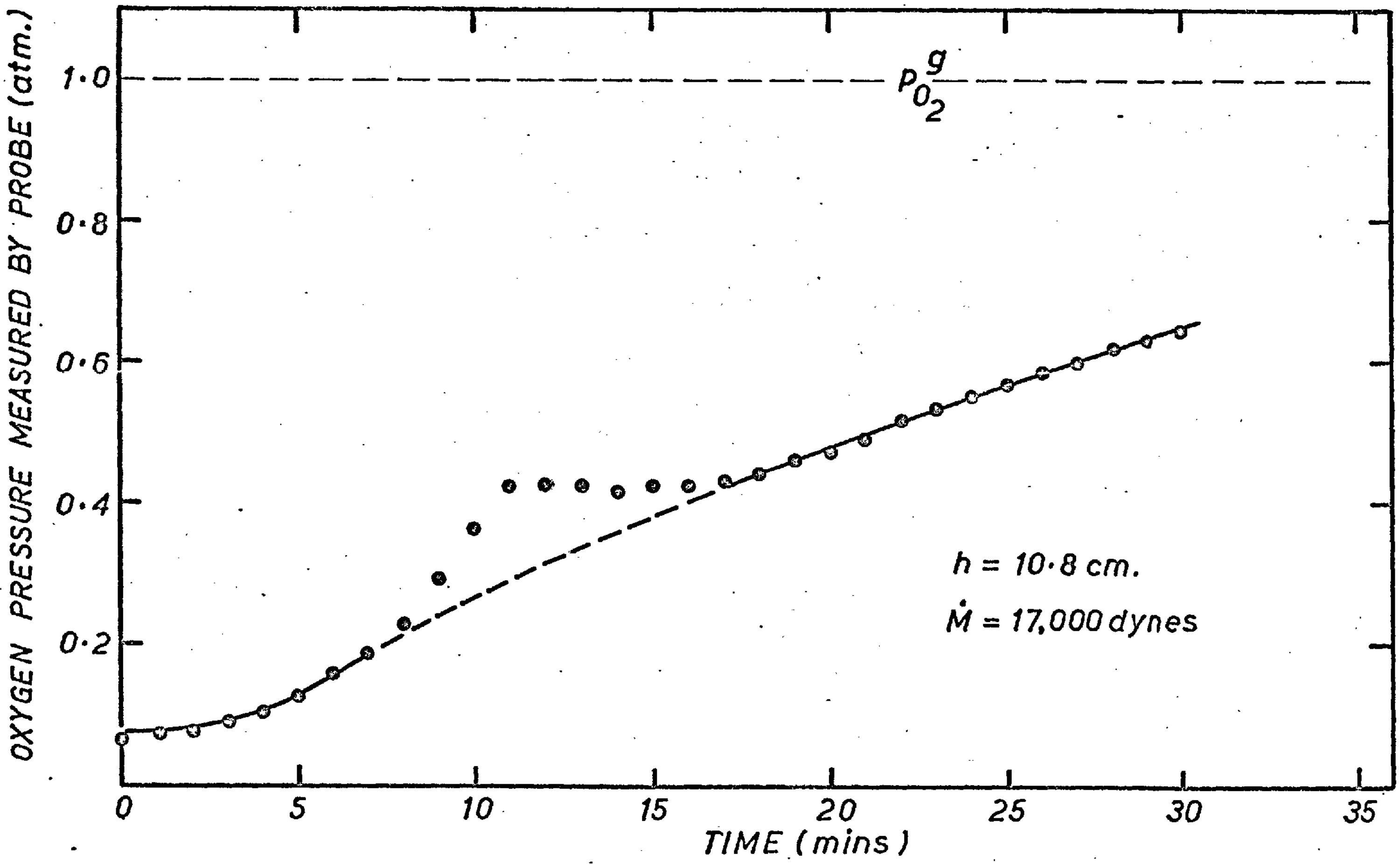

FIG.5.8–1 VARIATION OF OXYGEN PRESSURE IN SILVER WITH TIME, USING A JET OF PURE OXYGEN, SHOWING INCOMPLETE MIXING OF THE BATH.

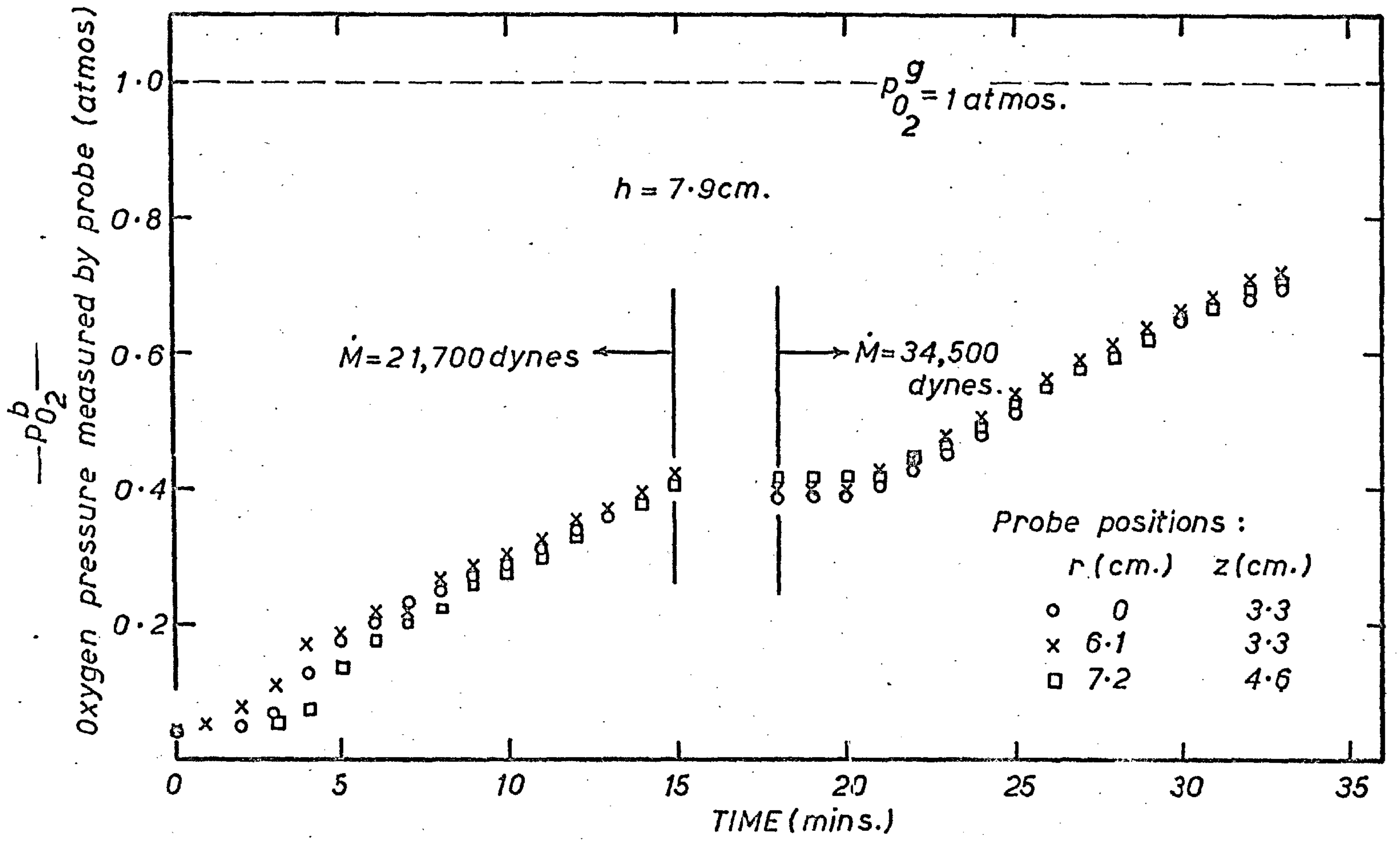

FIG.5.8-2 VARIATION IN MIXING OF SILVER BULK, WITH INCREASING JET MOMENTUM $\dot{M}$.

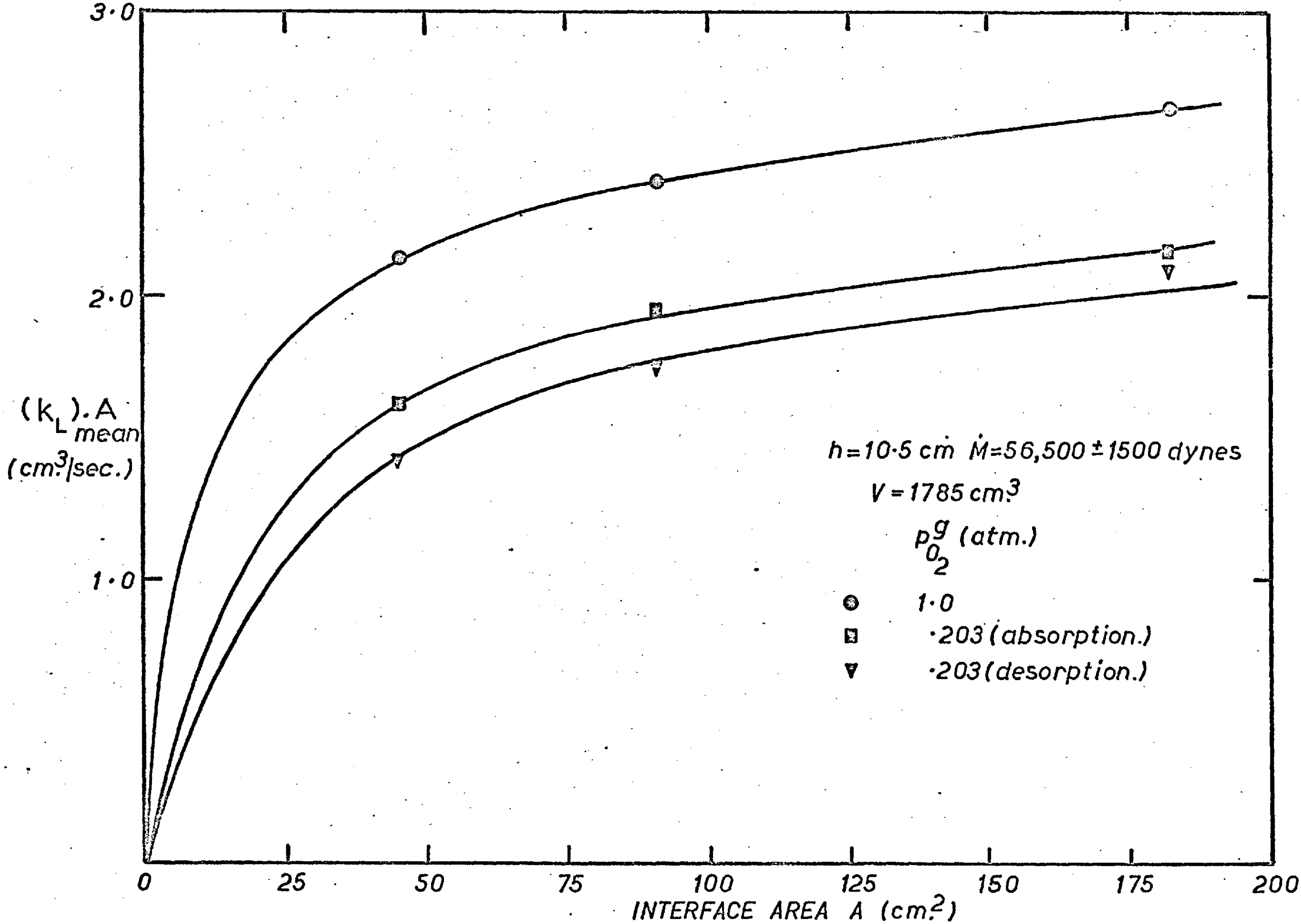

FIG.5.8-3 VARIATION OF TRANSFER RATE WITH INTERFACE AREA A

6.0 DISCUSSION OF RESULTS

6.1 Nozzle Characteristics

The values obtained for the coefficient of discharge of the small diameter converging nozzles used in both the high and low temperature investigations compare satisfactorily with those found in the literature, for example those of Kastner et al[53]. The tendency for the value of C_d to decrease at low Reynolds numbers, as shown in Figure 4.3-1, has been noted by previous investigators, and has been predicted by Bragg[61], using a modified force-defect theory. It must be noted, however, that the accuracy of flow measurement by the rotameter decreases at the low end of its range.

The difference in jet momentum, between the one measured by impingement on a flat plate, and that measured using the system described in section 4.3, is of interest. Other workers, for example Denis[40], have used impingement on a flat plate as a means of determining jet momentum. It is uncertain whether the extra force produced on the plate, as shown in Figure 4.3-2, was due to the momentum of the gas entrained into the radial wall jet produced on the plate, or whether it resulted from an upward velocity vector in the gas departing from the area of impingement. Bradshaw and Love[34] indicate such an upward velocity vector. It would appear that the effect occurred close to the area of impingement, as the size of the flat plate had little effect on the balance reading. It would seem that only small upward velocity of the gas would be required. For example, an air jet issuing from the .253cm. dia. nozzle at 1.15g/sec. has an exit velocity of 18,800cm/sec. and a momentum of 21,600 dynes. At a distance of 20cm. downstream it has a mass flow of 23.5g/sec. and a centre-line velocity of 1600cm/sec. Thus for a 10% increase in the force recorded on a flat plate at this point, an upward velocity of 92cm/sec. in the departing gas would be required.

6.2 The Free Jet

The application of Newton's 2nd Law of motion to a submerged jet, i.e. a jet issuing into an ambient fluid of equal density, shows that the jet momentum is a conserved property, and is equal to $\frac{\pi d^2}{4} \cdot \rho . V_J^2$. This assumes that the pressure is hydrostatically distributed throughout the flow. If viscous effects are neglected, then the velocity profiles across the jet should be dynamically similar under all conditions. In other words $\frac{V}{V_o} = f(\eta)$ where $\eta = \frac{r}{x'}$

x' is the distance downstream from the origin of a point source with a momentum vector equal to that of the jet.

From the conservation of momentum it can be shown that

$$\frac{V_o}{V_J} = K. \frac{d}{x'}$$

Similarly for the conservation of mass

$$\frac{\dot{m}}{\dot{m}_J} = K' \cdot \frac{x'}{d}$$

From consideration of the kinetic energy

$$\frac{\dot{E}}{\dot{E}_J} = K'' \cdot \frac{d}{x'}$$

where $K = \frac{1}{\sqrt{8 I_{\dot{M}}}}$, $K' = \sqrt{\frac{8}{I_{\dot{M}}}} \cdot I_{\dot{m}}$, $K'' = \frac{I_E}{\sqrt{8 I_{\dot{M}}^{3}}}$

and $I_{\dot{m}} = \int_0^\infty f(\eta) \cdot \eta \cdot d\eta$

$$I_{\dot{M}} = \int_0^\infty f^2(\eta) \cdot \eta \cdot d\eta$$

$$I_E = \int_0^\infty f^3(\eta) \cdot \eta \cdot d\eta$$

This treatment is due to Holdhusen[61], and is applicable independant of the form of the velocity distribution across the jet. Use of a normal error curve to describe the distribution, as in the work of Albertson et al[24], and Abraham[32], provides a convenient means of determining the constants in the final equations.

with $\frac{V}{V_o} = \exp\left\{-\beta \left(\frac{r}{x'}\right)^2\right\}$

the constants become

$$K = \sqrt{\frac{\beta}{2}} \quad , \quad K' = 2\sqrt{\frac{2}{\beta}} = \frac{2}{K} \quad \text{and } K'' = \frac{\sqrt{2\beta}}{3} = \frac{2}{3} K$$

However, the use of the error curve has the disadvantage of specifying that the zone of jet diffusion extends to infinity. The experimental values of V/V_o obtained in section 4.4 indicate good agreement with a normal error curve up to values of r/x equal to .15, beyond which values of V were too small to measure accurately. The measurement of centre-line velocity V_o by pitot was possible up to values of x/d of 200, but at these distances it was not possible to measure the velocity distribution. It can be seen from Figures 4.4-1 and 4.4-3 that the values of β and K vary with the throat Reynolds Number. For $Re = 8x10^3$, $\beta = 80$ and $K = 6.2$. Increasing Re to $3x10^4$ raised the value of K to 7.8. Furthermore, at high Reynolds Numbers ($Re = 5x10^4$), K was not constant, but changed gradually from 8.6 just outside the potential core, to 7.0 at large values of x/d (200). Other investigators have noted the effect of Reynolds Number on K. Baines[29] reported an increase in K with increasing values of Re, and also an increase in the length of the potential core. Further examination of the actual points in his graph suggest that the coefficient K for the jet with $Re = 7x10^4$ was not in fact constant, but decreased with increasing values of x/d. However, his results terminated for values of x/d of 60, and consequently the value of K did not reach that found for a slower jet with $R = 2.1x10^4$. Ricon and Spalding[30] determined the constant K by measuring the axial mass flow rate in the jet.

Using this technique they were able to extend their measurements up to values of x/d of 400. They found an increase in mass entrainment rates (i.e. a decrease in K) below Re = $2.5\text{x}10^4$, where K = 6.25, down to Re = $5\text{x}10^3$ where K = 5.0. However, above Re = $2.5\text{x}10^4$ they found mass entrainment rates to be substantially constant, and did not report any variation of K with x/d.

The variation in the value of K indicates that it is not satisfactory to assume similarity between two jets at different Reynolds Numbers. At short distances from the nozzle, the velocity distribution depends on the immediate history of the jet, and hence on the nozzle diameter and Reynolds Number, and may also be related to the degree of upstream turbulence. At large distances downstream, these effects are likely to be of minor importance.

6.3 Impingement of jet on Liquid Surface

a) Depression

The main measurements in the room temperature investigation on the dimensions of the depression were concentrated on its depth below the free liquid surface. This dimension has also been chosen as the principal characteristic of the depression by other investigators. The depth n_o has been correlated with the jet momentum $\dot{M}$ and nozzle height h using a stagnation pressure analysis at the centre-line of the jet. This assumption leads to the equation

$$n_o = \frac{\beta}{\pi} \frac{\dot{M}}{\rho_L g x^2}$$

The values of n_o obtained for both water and mercury agree with this analysis, provided that the distance of the stagnation point from the nozzle x is taken as $(h + n_o)$, as shown in Figure 6.3-1. The work of Poreh and Cermak[26] and of Bradshaw and Love[34] suggests that the stagnation region is small, of the order of .03 to .05 h. Thus for values of n_o/h greater than 0.5, it is quite justifiable to take into account the extra distance of travel of the jet below the liquid surface. Neglecting the additional distance of travel, up to values of n_o/h of 0.5 has little effect on the results. It must be noted, however, that when the jet is contained in a deep cavity, normal entrainment can no longer occur, and in this respect the treatment is not entirely rigorous.

From measurements on the diameter and the shape of the depression in water, a parabola was fitted to the bottom of the depression and the top of the raised lip. This was found to be a reasonable approximation (Figures 4.5-5a and 4.5-5b). Such a parabola may be predicted by an irrotational flow which is given by:

$$P_{Max} - P = \rho \frac{c^2}{2} \left(r^2 + 4\,(h-x)^2\right)$$

where P is the additional pressure above the static pressure, and c is a constant

The velocities in such flow are

$$V_x = 2c\,(h-x) \quad \text{into stagnation area}$$

$$V_r = c.r \quad \text{out of " "}$$

At the plane $h = x$

$$P_{Max} - P = \rho \frac{c^2}{2} . r^2$$

An analysis of the results of Poreh and Cermak gives a value of c equal to $98/h^2 . \sqrt{\dot{M}/\rho}$. This derivation assumes a uniform velocity in the impinging jet, and is therefore confined to a small region in the vicinity of the stagnation point. At large depression depths for small nozzle heights, the gas is given a substantial upward momentum on departing from the depression. This causes a bellowing of the cavity.

The combined effect of higher surface tension and the higher density of mercury reduced the height of the lip around the depression in comparison with the water results. However, a parabola fitted to the lower part of the cavity proved a good approximation to its shape in this region (Fig. 4.6-4).

From the measured shapes, the radius of curvature of the depression at its maximum depth could be evaluated, and the effect of interfacial tension calculated. Taking interfacial tension into account results in:

$$n_o + \frac{2\sigma}{\rho_L g R_o} = \frac{\beta}{\pi} \cdot \frac{\dot{M}}{\rho_L g(h+n_o)^2}$$

Results in this form are shown in Fig. 6.3-2. The agreement between water and mercury results was improved, and β was determined as 115.

In Fig. 6.3-3, the results of the present worker are compared with the estimated scatter of the work by Banks and Chandrasekhara[18] and by Mathieu[37]. The results of Banks were presented in the form of a graph of n_o/h versus $\dot{M}/\rho_L g n_o^3$. In the present work the dimensionless group $\dot{M}/\rho_L g h^3$ was chosen for the following reasons. Firstly, as the accuracies of measurement of n and h were of the same order, ± .01cm., it follows that for values of h much larger than n_o, the relative ~~accuracy of measurement of h much larger than n, the relative~~ accuracy of measurement of h was correspondingly larger. Also, for a fixed value of $\dot{M}/\rho_L g h^3$, small variations in the value of n_o are immediately obvious. However the method of presentation of results used by Banks conceals these small variations in n_o, as both the ordinate and abscissa values will be altered.

The deviation from the theoretical curve of the present results obtained at low values of n_o/h for water, may be due to the method of measurement adopted. In the experimental system, the depression appeared dark against a light background. It was thus easier to measure the position of the maximum oscillation of the depression than to measure the minimum position, which may have been overestimated. This overestimation would lead to larger relative errors in n_o at small values of n_o/h.

b) Splashing

The splashing results for water presented in Figure 4.5-1 show a decrease in the value of n_o at which drop formation commences, for increasing values of h. These results indicate that, for a particular gas/liquid system, though the stagnation pressure, and hence the velocity in the impingement area, is the main factor influencing the breakup of the surface, the area of the depression has some effect. Thus the distance over which the shearing forces on the liquid surface act influences the stagnation velocity required for drop formation.

The critical depth of depression n_c, for which splashing commences, may be dependent on the following parameters:

$$n_c = f\,(\rho_L, \rho_L g, \mu_L, \sigma, V_o, \rho_g, \mu_g, h)$$

Noting that $V_o^2 \propto \dot{M}/h^2$, the following dimensionless parameters may influence drop formation:

$$\left(\frac{g\rho_L}{\sigma}\right)^{1/2} n_c = f\left(\frac{\rho}{\rho_L}, \frac{\mu}{\mu_L}, \frac{\sigma}{\rho_L g h^2}, \frac{g\mu_L^4}{\rho_L \sigma^3}, \frac{\dot{M}}{\rho_L g h^3}\right)$$

In future investigations it will be necessary to study the effect of variation of liquid properties on drop formation, to determine which of the parameters has the greatest significance. It is noted that the parameter $g\mu_L^4/\rho_L\sigma^3$ has been used by investigators [66,67] in the study of drag on rising bubbles, and is solely a property of the liquid.

c) Bath Circulation

The stirring action of a jet of CO_2 on the water bath is shown in Figures 4.7-1 and 4.7-2. The CO_2 can be considered as virtually non-absorbed, as only 1-2% of the total gas blown on to the surface was absorbed, as measured in the mass transfer experiments. The circulation pattern consisted of a surface layer moving outwards in a radial direction, the motion being imparted by the drag of the gas along the interface. Fluid from the bulk was entrained into this surface layer, which, on deflection at the wall of the tank, produced a toroidal vortex. ~~If the tank had had infinite dimensions, then no vortex would have formed.~~ However, the dimensions of the container only seriously influence the velocities in the surface layer, when the fluid entrained from the bulk is already moving at a comparable velocity. The uniform mixing of the water bulk was affected when the ration of bath depth (Z) to bath diameter became greater than approx. 0.35. At larger depths, a stagnant region formed at the bottom of the tank.

The stirring action of the oxygen jet on the silver bath was assumed to be similar to that of a CO_2 on water, from the detection (page 102) of an oxygen-rich stream at the edge of the bath. However, much higher jet momentums were required to give adequate mixing for mass transfer work.

A comparison of the flow patterns for CO_2 impinging on water at $\dot{M}$ = 14,700 dynes and h = 17cm. (Fig. 4.7-2), and at $\dot{M}$ = 8650 dynes and h = 8cm. (Fig. 4.7-1), shows that, although the kinetic energies of the two jets were the same on impingement ($6x10^6$ dyne-cm/sec.), the transfer of energy to the bath was more efficient in the first case. This is in line with the observation that droplet formation occurs at smaller depths of depression for increasing lance height, and is related to the area of the interface over which the jet impinges.

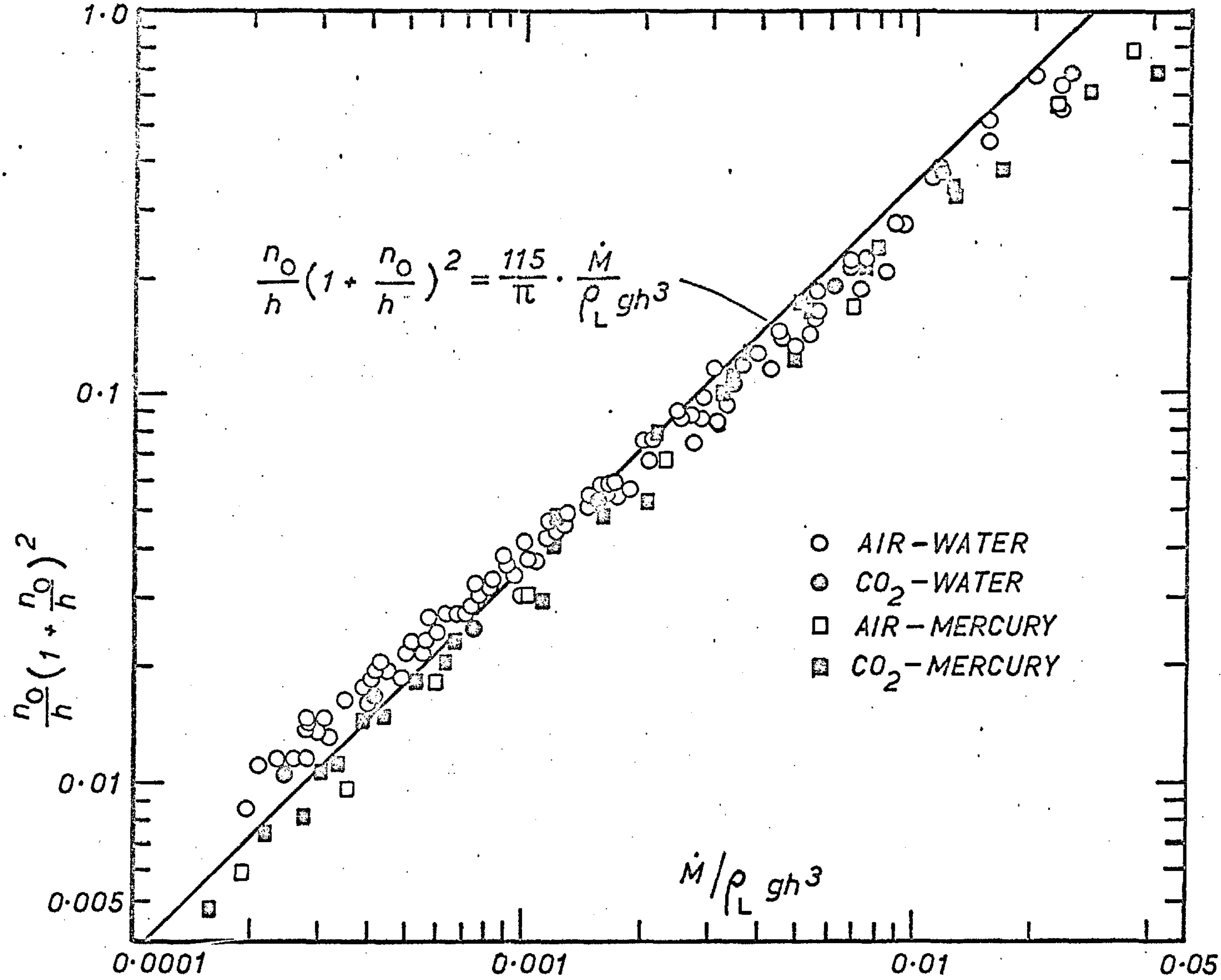

FIG.6.3-1 VARIATION OF DEPTH OF DEPRESSION BELOW FREE LIQUID SURFACE n_0, WITH JET MOMENTUM $\dot{M}$, AND NOZZLE-LIQUID DISTANCE, NEGLECTING EFFECT OF SURFACE TENSION.

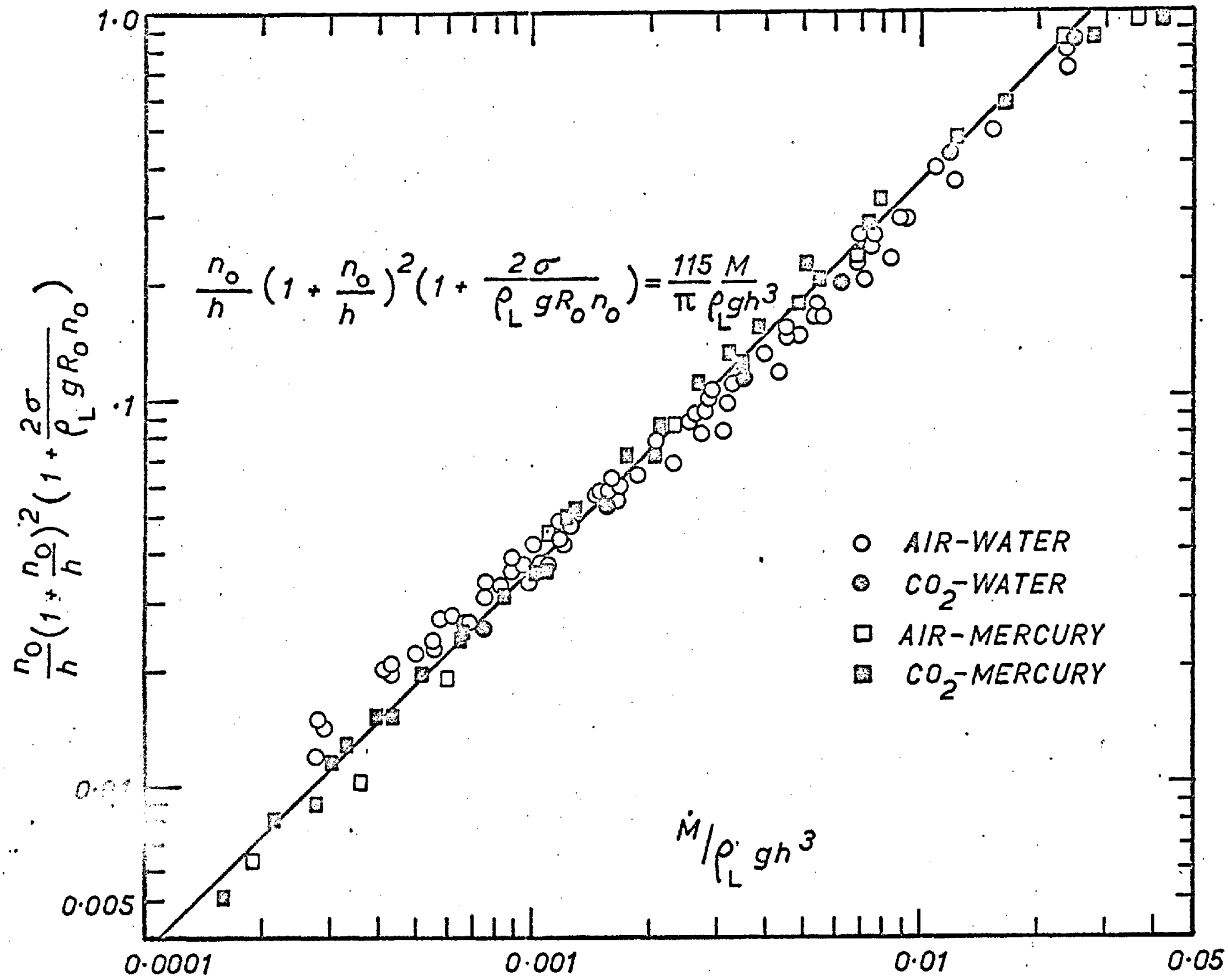

FIG.6.3-2 VARIATION OF DEPTH OF DEPRESSION BELOW FREE LIQUID SURFACE n_0, WITH JET MOMENTUM $\dot{M}$, AND NOZZLE LIQUID DISTANCE h, INCLUDING EFFECT OF SURFACE TENSION σ.

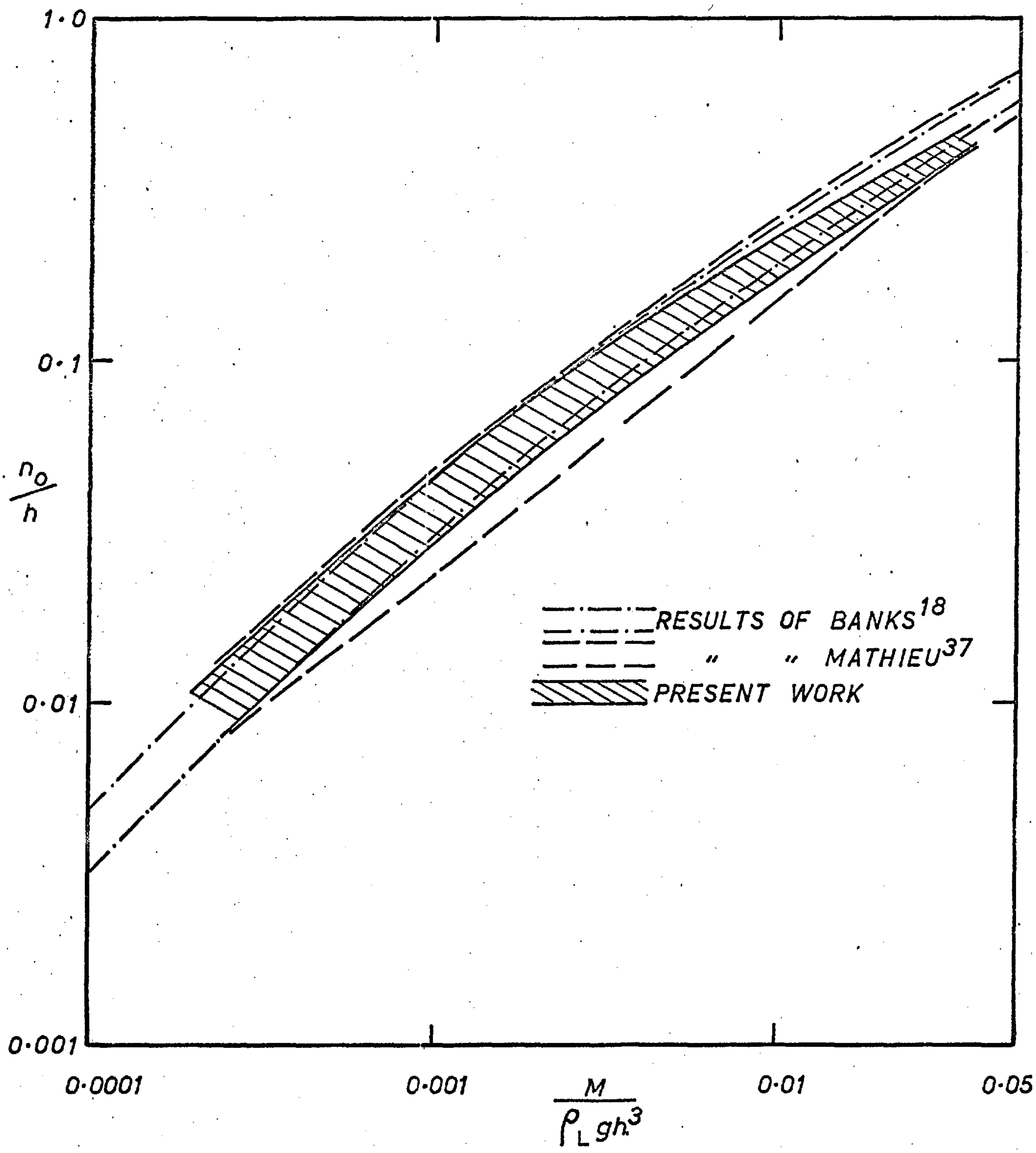

FIG.6.3-3 COMPARISON BETWEEN PRESENT WORK ON DEPTH OF DEPRESSION n_o, IN AIR-WATER SYSTEM WITH PREVIOUS RESULTS.

6.4 Mass Transfer Work.

a) CO_2 - water system.

The measured mass transfer coefficients (Figure 4.8-2) versus lance height, for different jet momentums, follow the trends observed in the rate of bath circulation. This set of results was for a total absorbing area of $4185cm^2$. Thus at a given lance height, the larger the jet momentum, the faster the rate of bath circulation, and the larger the measured mass transfer coefficient. At constant jet momentum, the influence of the lance height was not very marked, except for the highest values of jet momentum. This is further support for the suggestion that at larger values of h the proportion of the jet energy imparted to the bath is increased. For example, similar mass transfer coefficients were obtained for jet energies on impingement of 4.2×10^6 dyne-cm/sec. (at $\dot{M} = 14600$ and $h = 24$cm) and of 6×10^6 dyne-cm/sec. (at $\dot{M} = 8650$ and $h = 8$cm.)

Comparison with the theory developed in Chap. 3 on the variation of mass transfer coefficient with the radial distance r (i.e. with the absorbing area A), for a given lance height and jet momentum, has been complicated by the difficulty of measuring surface velocities. However the experimental results are presented in Figure 6.4-1, which also shows the variation predicted for the cases when u_r = constant and when $u_r . r$ = constant. A value of $D_{CO_2} = 1.5\times10^{-5}$ cm^2/sec. was used. The temperature variation in this series of results was small ($17.5 \pm 1.5^{o}C$). The indicated experimental points correspond to the values shown in Fig. 4.8-3. In general the results suggest that the surface velocity depends on a higher power of r than either solution predicts:

$$u_r . r^n = \text{constant} \quad \text{where } n > 1$$

In this context the effect of surface active agents on the system must be considered. A standard experimental procedure in filling the tank from the water supply was adopted. The water line was flushed through until water was obtained direct from the head tank (marked by a drop in water temperature) and then the tank was flushed through with water for 15 minutes, before finally filling. This did not remove the presence of surface active agents, but attempted to maintain their effect as constant as possible. When the jet impinged on the surface of the water, a build up in the surface active agent concentration occurred towards the edge of the tank. A force opposing the drag of the gas was thus exerted, destroying the radial motion of the liquid surface at some distance from the edge of the tank. This effect could be more clearly seen in aqueous solutions of PVA. Future work on surface active free systems would be of interest, to study any change in rate of decay of the surface velocity, and hence the mass transfer coefficient, with radial distance.

The similar results obtained for desorption experiments and absorption in the small tank further suggest that the liquid surface velocity is the controlling factor in mass transfer to the liquid. Droplet formation has little effect on the measured rates of mass transfer.

b) Oxygen - silver system

The results obtained for oxygen absorption and desorption in molten silver at 1000°C follow a similar pattern as for the room temperature mass transfer results. However stirring of the silver by the oxygen jet was not as efficient as the action of the CO_2 jet on water, and the range of results was severly restricted to jet momentums above 20,000 dynes. No measurement of the surface velocities in the silver was attempted. However, the results in Appendix III, and values of the mass transfer coefficient predicted by $u_r.r$ = constant may be compared, using a value of $u_r.r = 80\ \text{cm}^2/\text{sec}$.

As D_{o_2} in silver $= 9 \times 10^{-5}\ \text{cm}^2/\text{sec.}$ 57

$$\text{then } K_{mean} = 2\left(\frac{2}{\pi}\right)^{1/2} (9\text{x}10^{-5}\text{x}80)^{1/2} \cdot \frac{1}{r_1} \ \text{cm}/\text{sec.}$$

r_1(cm)	Measured K_{mean}(cm/sec.x10^2)	Predicted K_{mean} (cm/sec.x10^{-2})
3.8	4.8	3.6
5.4	2.5 For P_{o_2} = 1 atm.	2.5
7.6	1.5	1.8

The measured mass transfer results decrease more rapidly with increasing r_1 than predicted by $u_r . r$ = constant, as was also found in the room temperature investigation. The mass transfer coefficients measured for absorption and desorption for $P_{o_2}^{g}$ = .2 atm. were similar to each other but those for $P_{o_2}^{g}$ = 1 atm. (as above) were approx. 25% larger for the same jet momentum and lance height. The energy of the jet was actually less in the case of $P_{o_2}^{g}$ = 1 atm., as the nozzle exit velocity was lower. However the viscosity of the pure oxygen jet was 10% in excess of the jet with $P_{o_2}^{g}$ = 2 atm., and this factor may have considerably influenced the drag force on the surface of the silver.

c) Jet degassing of steel to remove hydrogen.

Results taken from the work of Hoyle[24] have been analysed using a similar procedure to the one presented above. Unfortunately only a few sufficiently accurate time measurements were quoted, and only these results have been treated. Assuming the hydrogen pressure at the interface to be negligible, Equation 4.8-2 reduces to

$$\ln \left(\frac{[H]_t}{[H]_{t=0}} \right) = - (k_L)_{mean} \cdot \frac{A}{V} \cdot t$$

The results are presented in Figure 6.4-2. From the measured slope, $(k_L)_{mean} = 1.92 \times 10^{-3} \cdot \frac{V}{A}$

Using $V = 1260 \text{cm}^3$ and $A = 81 \text{cm}^2$

Then $(k_L)_{mean} = 3 \times 10^{-2}$ cm/sec.

As the stirring in the system was partly due to the jet and partly to induction stirring, direct comparison with the present work is difficult, especially as the momentum of the jet was not evaluated. However using a value of D_H in steel of 150×10^{-5} cm^2/sec, a surface velocity of the order of 200cm/sec. can be predicted.

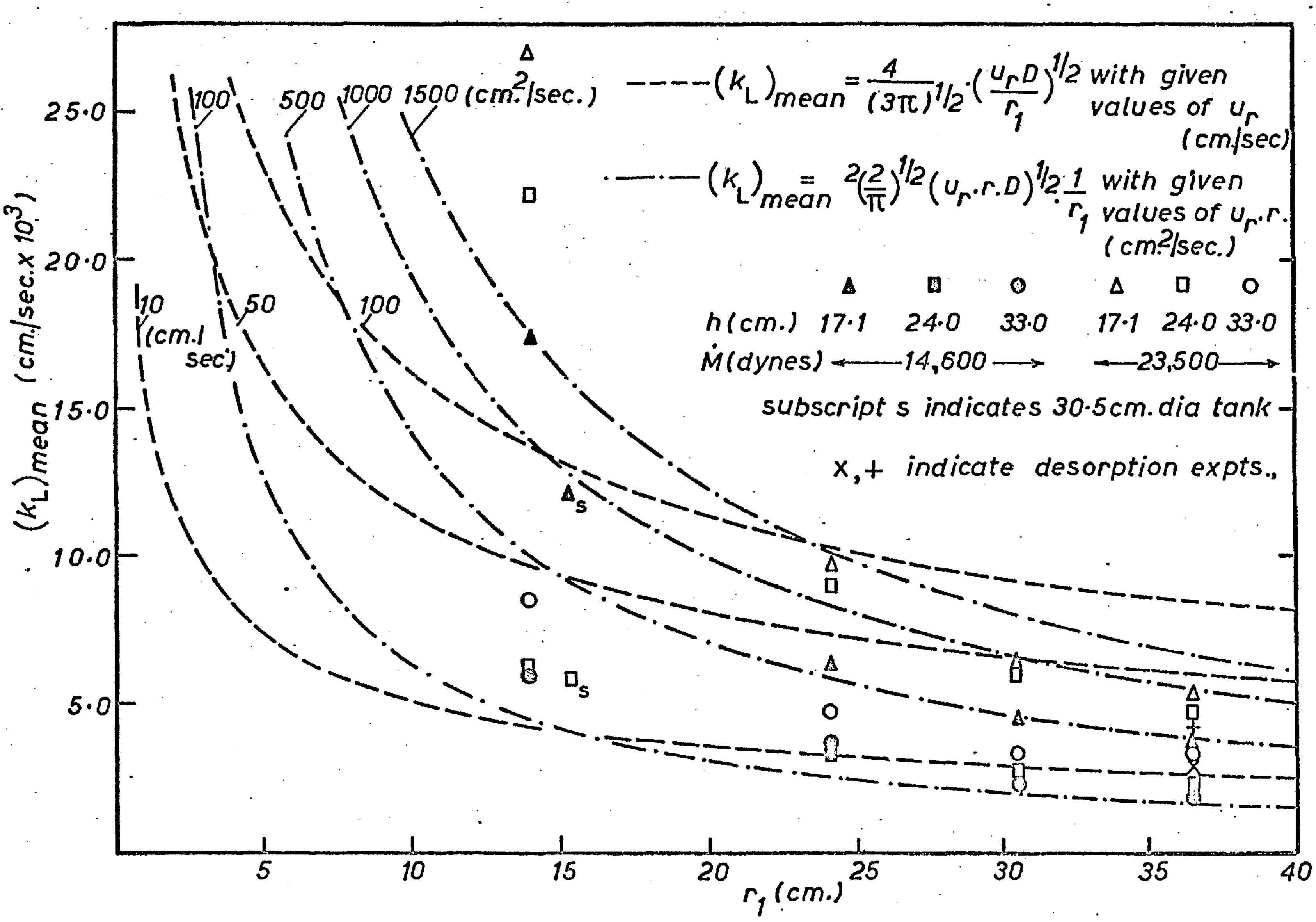

FIG. 6.4-1 COMPARISON OF MASS TRANSFER COEFFICIENTS OBTAINED FOR CO WATER SYSTEM WITH THEORETICAL CURVES.

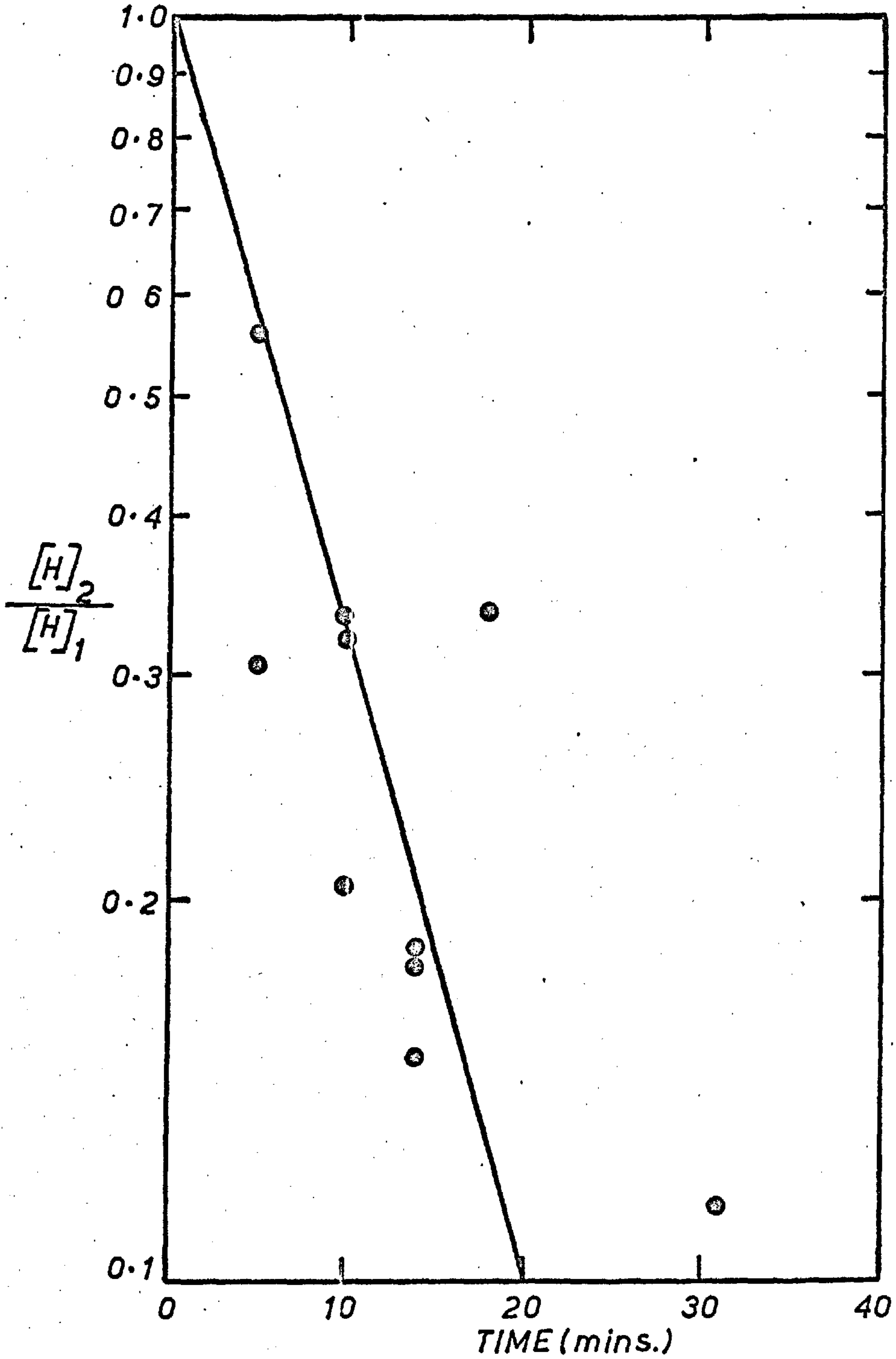

FIG.6.4-2 RESULTS OF HOYLE[24] FOR REMOVAL OF HYDROGEN FROM STEEL USING A JET OF ARGON

CONCLUSIONS

Measurements on the free jet show agreement with previously proposed equations for the velocity decay and profile across the jet. The measured jet constants are similar to those obtained by previous workers. A marked dependence of K on Re has been noted.

The measured depth of the depression formed by jets of air and carbon dioxide impinging on water and mercury correlates well with stagnation pressure analysis. The assumption of a paraboloidol shape for the depression has enabled the effect of the interfacial tension on the depth of the depression to be calculated. This improves the agreement with stagnation pressure analysis.

Circulation patterns and velocities, measured photographically, show a dependence on jet energy and nozzle-water distance similar to the commencement of splashing.

Rates of mass transfer between the CO_2 jet and water show quantitative agreement with a quasi-steady state theory using a radial flow model. The measured mass transfer coefficients, from .003 to .025 cm/sec, show marked dependence on the liquid surface velocity.

A high temperature apparatus has been developed to measure oxygen transfer to liquid silver. Preliminary results indicate that the stirring action of the jet is much less effective than in the room temperature system. Mass transfer coefficients show a similar dependence on the liquid surface velocity.

ACKNOWLEDGEMENTS

Sincere appreciation is extended to Professor A.V. Bradshaw for supervision and assistance given during the course of this work.

Discussion with members of the John Percy Research Group and of the Nuffield Research Group have been extremely useful. The author wishes to extend his thanks especially to Dr. W.G. Davenport in this respect. The technical assistance of Mr. A.J. Haynes proved invaluable.The moral support lent to the author by his wife during the preparation of this thesis is also gratefully acknowledged.

Financial support during the investigation was provided by the British Iron & Steel Research Association through Professor F.D. Richardson.

Appendix 1

MEASUREMENTS ON DIMENSIONS OF DEPRESSION IN LIQUID SURFACE

TABLE I (aqueous solutions) shows, for variations in nozzle - liquid distance (h) and jet momentum flux ($\dot{M}$), values of:

i). Cavity depth below free liquid surface (n_o).

ii). Total cavity depth ($n_o + 1$).

iii). Diameter of cavity across lip (m)

iv). Surface area of cavity (s) computed from:

$$S = \frac{m^4}{96(n_o+1)^2}\left[\left\{1 + \frac{16\,(n_o+1)^2}{m^2}\right\}^{3/2} - 1\right]$$

v). Radius of curvature of cavity at stagnation point (Ro) computed from:

$$R_o = \frac{m^2}{8(n_o + 1)}$$

N.B. Some values of m are shown marked with an asterisk. These are diameters of the cavity at the level of the free liquid surface. In these cases R_o has been computed as $\dfrac{m^{*2}}{8\,n_o}$.

a). <u>AIR ON WATER</u> d = .253cm. ρ_L = 1.0g.cm^{-3} σ = 73 dynes.cm^{-1} Z = 19.32-19.74cm.

h (cm.)	$\dot{M}$ dynes x10^{-4}	$\frac{\dot{M}}{\rho_L g h^3}$ (x10^3)	n_o (cm.)	$\frac{n_o}{h}$ (x10)	$n_o + 1$ (cm.)	$\frac{n_o + 1}{h}$ (x10)	m (cm.)	$\frac{m}{h}$	S (cm.^{2})	$\frac{S}{h^2}$	R_o (cm.)	$1+\frac{2\sigma}{\rho_L g R_o n_o}$
4.00	.145	23.1	1.42	3.55	2.09	5.22	2.54	.635	12.5	.782	.39	1.270
4.02	.150	23.5	1.29	3.21	2.48	6.16	2.13*	-	-	-	.43	1.270
5.95	.150	7.29	.95	1.60	1.29	2.17	2.25*	-	-	-	.67	1.235
"	.250	12.1	1.29	2.17	2.46	4.14	2.85*	-	-	-	.79	1.145
6.01	.145	6.85	.98	1.63	1.28	2.13	2.89	.481	10.3	.285	.82	1.185
7.81	.150	3.22	.62	.795	1.41	1.81	2.51*	-	-	-	1.27	1.190
"	.250	5.35	.89	1.14	2.33	2.98	3.07*	-	-	-	1.33	1.125
"	.390	8.35	1.22	1.56	-	-	3.45*	-	-	-	1.22	1.100
8.07	.560	10.9	1.93	2.39	3.20	3.96	5.21	.646	41.5	.637	1.06	1.075
"	.780	15.3	2.46	3.05	-	-	5.88	.728	-	-	-	-
"	1.030	20.0	2.97	3.68	-	-	6.31	.782	-	-	-	-
8.09	.145	2.80	.61	.755	.91	1.12	3.50	.433	11.8	.181	1.68	1.145
"	.380	7.32	1.30	1.61	1.95	2.41	3.99	.494	20.9	.320	1.02	1.110
"	.785	15.1	2.26	2.79	3.99	4.94	5.00	.619	46.8	.715	.78	1.080
9.39	.150	1.85	.48	.51	1.65	1.76	2.94*	-	-	-	2.25	1.140
"	.250	3.09	.62	.66	2.51	2.68	3.27*	-	-	-	2.15	1.110
"	.395	4.87	1.02	1.09	-	-	3.64*	-	-	-	1.62	1.090
"	.580	7.15	1.36	1.45	-	-	4.18*	-	-	-	1.60	1.070
11.45	.395	2.68	.76	.665	1.27	1.11	3.58*	-	-	-	2.11	1.095
"	.580	3.93	1.17	1.02	1.98	1.73	4.79*	-	-	-	2.45	1.050
"	.800	5.44	1.40	1.22	2.36	2.06	4.85*	-	-	-	2.06	1.050
11.50	.385	2.58	.85	.74	1.15	1.00	4.70	.409	21.0	.159	2.40	1.075
"	.795	5.34	1.49	1.30	2.41	2.10	5.63	.490	38.3	.289	1.64	1.060
"	1.380	9.25	2.25	1.96	4.11	3.58	6.43	.559	65.0	.492	1.26	1.055

h (cm.)	$\dot{M}$ dynes $\times 10^{-4}$	$\frac{\dot{M}}{\rho_L g h^3}$ $(\times 10^3)$	n_o (cm.)	$\frac{n_o}{h}$ $(\times 10)$	$n_o + 1$ (cm.)	$\frac{n_o + 1}{h}$ $(\times 10)$	m (cm.)	$\frac{m}{h}$	S (cm^2)	$\frac{S}{h^2}$	R_o (cm.)	$1+\frac{2\sigma}{\rho_L g R_o n_o}$
11.53	.145	.964	.33	.285	-	-	3.31*	-	-	-	4.15	1.110
"	.245	1.63	.54	.47	-	-	3.62*	-	-	-	3.03	1.090
"	1.030	6.85	1.83	1.59	3.08	2.68	5.77	.501	46.2	.348	1.36	1.060
"	1.345	8.95	2.24	1.94	3.81	3.30	6.29	.545	59.8	.450	1.29	1.050
"	1.735	11.5	2.91	2.52	4.90	4.25	6.66	.578	77.8	.585	1.13	1.045
13.77	.580	2.28	.79	.575	1.36	.985	4.05*	-	-	-	2.60	1.075
"	.800	3.13	1.13	.82	1.95	1.42	5.35*	-	-	-	3.17	1.040
"	1.050	4.11	1.31	.95	2.66	1.93	5.75*	-	-	-	3.15	1.035
13.88	.145	.555	.29	.21	-	-	3.62*	-	-	-	5.65	1.100
"	.245	.940	.45	.325	-	-	3.89*	-	-	-	4.20	1.080
"	.380	1.46	.68	.49	-	-	4.21*	-	-	-	3.26	1.065
17.12	.795	1.62	.90	.525	1.23	.72	7.00	.409	42.6	.145	4.98	1.035
"	1.380	2.81	1.44	.84	2.49	1.46	7.86	.460	65.0	.222	3.10	1.035
"	2.220	4.51	1.93	1.13	3.46	2.02	8.64	.505	87.4	.298	2.70	1.030
17.15	.145	.294	.23	.135	-	-	4.82*	-	-	-	12.6	1.050
"	.245	.496	.35	.205	-	-	5.01*	-	-	-	8.98	1.045
"	.375	.759	.49	.285	-	-	5.07*	-	-	-	6.56	1.045
"	.550	1.11	.67	.39	-	-	5.10*	-	-	-	4.85	1.030
"	.780	1.58	.88	.515	1.22	.715	7.67	.447	50.6	.172	6.05	1.030
"	1.725	3.50	1.66	.97	2.85	1.66	8.76	.511	80.8	.275	3.37	1.030
"	2.180	4.41	1.96	1.14	3.43	2.00	9.89	.576	106.	.361	3.56	1.020
"	2.720	5.50	2.44	1.42	4.56	2.66	-	-	-	-	-	-
17.20	1.050	2.10	1.03	.60	1.73	1.01	6.58*	-	-	-	5.25	1.030
"	1.370	2.75	1.34	.78	2.69	1.56	7.10*	-	-	-	4.70	1.025
20.69	1.370	1.59	1.06	.51	1.86	.90	8.88	.429	71.8	.167	5.30	1.025
"	1.785	2.05	1.36	.655	2.60	1.26	9.68	.467	92.0	.214	4.50	1.025
20.86	.245	.276	.24	.115	-	-	5.40*	-	-	-	15.2	1.040
"	.375	.421	.41	.195	-	-	6.14*	-	-	-	11.5	1.030

h (cm.)	$\dot{M}$ dynes $\times 10^{-4}$	$\frac{\dot{M}}{\rho_L g h^3}$ ($\times 10^{-3}$)	n_o (cm.)	$\frac{n_o}{h}$ ($\times 10$)	$n_o + 1$ (cm.)	$\frac{n_o + 1}{h}$ ($\times 10$)	m (cm.)	$\frac{m}{h}$	S (cm^2)	$\frac{S}{h^2}$	R_o (cm.)	$1+\frac{2\sigma}{\rho_L g R_o n_o}$
20.86	.550	.617	.55	.265	-	-	6.45*	-	-	-	9.46	1.030
"	.780	.876	.74	.355	-	-	6.72*	-	-	-	7.64	1.025
"	1.030	1.15	.91	.435	1.24	.595	8.46	.406	58.5	.135	7.22	1.025
"	1.345	1.51	1.07	.515	1.67	.80	9.21	.441	74.4	.171	6.35	1.020
23.97	1.365	1.01	.85	.355	1.31	.545	9.75	.407	75.6	.132	9.05	1.020
"	2.185	1.62	1.28	.535	2.28	.95	10.33	.432	97.0	.169	5.85	1.020
"	3.325	2.47	1.80	.75	3.31	1.38	10.37	.434	112.	.196	4.05	1.020
24.11	.375	.273	.35	.145	-	-	6.18*	-	-	-	13.6	1.030
"	.550	.405	.46	.19	-	-	6.26*	-	-	-	10.7	1.030
"	.780	.569	.61	.255	-	-	6.43*	-	-	-	8.58	1.030
"	1.035	.755	.73	.305	-	-	6.87*	-	-	-	8.09	1.025
"	1.370	1.00	.93	.385	1.31	.545	7.58*	-	-	-	7.72	1.020
"	1.750	1.28	1.07	.445	1.61	.67	9.80	.407	82.5	.142	7.45	1.020
"	2.210	1.61	1.28	.53	2.19	.91	9.85	.409	89.5	.154	5.55	1.020
"	2.745	2.00	1.59	.66	2.76	1.15	-	-	-	-	-	-
"	3.370	2.46	1.83	.76	3.31	1.37	-	-	-	-	-	-
"	4.140	3.02	2.18	.905	-	-	-	-	-	-	-	-
27.17	2.230	1.14	1.08	.40	1.84	.675	11.38	.419	110.	.150	8.81	1.015
"	2.810	1.44	1.28	.47	2.50	.92	11.95	.440	130.	.176	7.15	1.015
27.24	.560	.282	.38	.14	-	-	-	-	-	-	-	-
"	.785	.395	.46	.17	-	-	-	-	-	-	-	-
"	1.040	.524	.58	.215	-	-	-	-	-	-	-	-
"	1.370	.690	.71	.26	1.00	.365	-	-	-	-	-	-
"	1.750	.881	.93	.34	1.44	.53	10.91	.400	97.9	.132	10.4	1.015
32.39	2.810	.845	.99	.305	1.67	.515	13.16	.406	141.	.134	13.0	1.010
"	3.450	1.04	1.15	.355	2.25	.695	13.55	.418	159.	.152	10.2	1.015
32.59	.780	.230	.38	.115	-	-	-	-	-	-	-	-
"	1.035	.306	.48	.145	-	-	-	-	-	-	-	-
"	1.370	.405	.57	.175	-	-	-	-	-	-	-	-
"	1.750	.516	.70	.215	-	-	-	-	-	-	-	-

h (cm.)	$\dot{M}$ dynes x10^{-4}	$\frac{\dot{M}}{\rho_L g h^3}$ (x10^3)	$n_{\bullet}$ (cm.)	$\frac{n_o}{h}$ (x10)	$n_o + 1$ (cm.)	$\frac{n_o + 1}{h}$ (x10)	m (cm.)	$\frac{m}{h}$	S (cm^2)	$\frac{S}{h^2}$	$R_{\bullet}$ (cm.)	$1+\frac{2\sigma}{\rho_L g R_{\bullet} n_o}$
32.59	2.210	.652	.85	.26	1.30	.40	13.07	.401	136.	.128	16.5	1.010
"	4.105	1.22	1.37	.42	2.43	.745	12.74	.391	144.	.136	8.35	1.015
"	5.015	1.48	1.59	.49	3.03	.93	-	-	-	-	-	-
37.13	1.040	.207	.40	.11	-	-	-	-	-	-	-	-
"	1.370	.272	.49	.13	-	-	-	-	-	-	-	-
"	1.750	.349	.59	.16	-	-	-	-	-	-	-	-
"	2.215	.441	.68	.185	-	-	-	-	-	-	-	-
"	2.760	.550	.81	.22	1.24	.335	12.40	.342	125.	.091	15.7	1.010
"	3.390	.675	.97	.26	1.66	.445	13.11	.354	140.	.102	13.0	1.010
"	4.150	.827	1.15	.31	1.91	.515	13.93	.376	163.	.118	12.7	1.010
41.74	1.380	.193	.36	.085	-	-	-	-	-	-	-	-
"	1.780	.250	.47	.115	-	-	-	-	-	-	-	-
"	2.250	.316	.54	.13	-	-	-	-	-	-	-	-
"	2.820	.395	.65	.155	-	-	-	-	-	-	-	-
"	3.460	.485	.75	.18	1.48	.355	-	-	-	-	-	-
"	4.270	.600	.99	.235	1.77	.425	-	-	-	-	-	-
"	5.250	.736	1.12	.27	2.11	.505	-	-	-	-	-	-

b) CO_2 ON WATER   d = .253cm. ρ_L = 1.0g.cm.$^{-3}$ σ = 73 dynes.cm.$^{-1}$ Z = 19.42-19.50cm.

h (cm.)	$\dot{M}$ dynes x10^{-4}	$\frac{\dot{M}}{\rho_L g h^3}$ (x10^3)	n_o (cm.)	$\frac{n_o}{h}$ (x10)	$n_o + 1$ (cm.)	$\frac{n_o + 1}{h}$ (x10)	m (cm.)	$\frac{m}{h}$	S (cm^2)	$\frac{S}{h^2}$	$R_\bullet$ (cm.)	$1+\frac{2\sigma}{\rho_L g R_o n_o}$
4.20	.173	24.8	1.55	3.69	2.49	5.93	2.71	.645	15.3	.869	.37	1.260
6.25	.285	11.9	1.51	2.42	2.52	4.03	3.49	.559	21.1	.539	.61	1.165
12.30	.630	3.45	1.12	.91	1.88	1.53	5.91	.481	36.6	.242	1.86	1.070
"	1.125	6.16	1.78	1.45	3.20	2.60	6.41	.521	54.9	.363	1.60	1.050
24.99	1.135	.742	.60	.24	1.02	.41	8.45	.338	59.2	.095	8.74	1.030
"	2.390	1.56	1.22	.49	2.25	.90	10.81	.433	106.	.169	6.49	1.020
33.05	.865	.245	.35	.11	-	-	-	-	-	-	-	-
"	1.485	.418	.55	.17	-	-	-	-	-	-	-	-

c) CO_2 ON P.V.A.   d = .253cm. ρ_L = 1.0g.cm^{-3} σ = 47 dynes.cm^{-1} z = 19.34-19.42cm.

4.78	.170	15.9	1.38	2.89	1.99	4.16	2.55	.534	11.9	.524	.41	1.170
6.84	.275	8.77	1.33	1.95	1.99	2.91	3.23	.472	16.0	.342	.65	1.110
12.56	.615	3.17	1.06	.845	1.64	1.31	5.79	.461	33.4	.211	2.55	1.035
"	1.115	5.74	1.65	1.31	2.91	2.32	6.15	.490	48.7	.310	1.63	1.035
24.10	1.115	.812	.66	.275	1.23	.51	9.22	.383	71.8	.123	8.65	1.020
"	2.350	1.71	1.13	.47	2.04	.845	10.46	.435	98.0	.169	6.70	1.015
33.24	.855	.237	.34	.10	-	-	-	-	-	-	-	-
"	1.465	.406	.47	.14	-	-	-	-	-	-	-	-

TABLE 2 (mercury) shows, for variations in nozzle-mercury distance (h) and jet momentum ($\dot{M}$), values of:

i). Cavity depth below free liquid surface (n_o).

ii). Total cavity depth (n_o+l).

iii). Diameter of cavity across lip (m).

iv). Radius of curvature of cavity at stagnation point (R_o), estimated from a parabola fitted to the lower portion of the depression.

a). CO_2 - Mercury $\rho_L = 13.56 g.cm^{-3}$ $\sigma = 487$ dynes.cm^{-1} d = .253cm. **Z = 9.92-10.05 cm.**

h (cm.)	$\dot{M}$ dynes $x10^{-4}$	$\frac{\dot{M}}{\rho_L g h^3}$ $(x10^3)$	n_o (cm.)	$\frac{n_o}{h}$ (x10)	n_o+1	m (cm.)	$\frac{m}{h}$	R_o (cm.)	$1+\frac{2\sigma}{\rho_L g R_o n_o}$
2.00	.173	16.3	.495	2.48	.495	1.25	.625	.28	1.53
"	.280	27.4	.675	3.38	.680	1.50	.75	.26	1.42
"	.430	40.5	.735	3.68	.835	1.70	.85	.25	1.40
3.00	.173	4.82	.300	1.00	.300	1.45	.485	.53	1.46
"	.280	7.80	.520	1.73	.540	1.45	.485	.39	1.36
"	.435	12.1	.680	2.27	.700	1.80	.60	.27	1.40
4.00	.172	2.02	.190	.475	.190	1.60	.40	1.09	1.35
"	.270	3.18	.340	.85	.340	1.70	.425	.67	1.32
"	.425	5.00	.540	1.35	.540	1.80	.45	.45	1.30
"	.625	7.35	.635	1.59	.665	2.05	.515	.37	1.31
5.00	.174	1.05	.140	.28	.140	1.95	.39	1.92	1.27
"	.285	1.71	.245	.49	.245	1.95	.39	1.00	1.30
"	.435	2.62	.380	.76	.380	1.90	.38	.84	1.26
"	.625	3.76	.520	1.04	.525	2.15	.43	.64	1.22
"	.865	5.21	.650	1.30	.670	2.40	.48	.52	1.22
6.00	.285	.995	.170	.285	.170	2.20	.365	2.04	1.21
"	.435	1.52	.270	.45	.275	2.40	.40	1.49	1.18
"	.620	2.16	.390	.65	.410	2.50	.415	1.12	1.17
8.00	.430	.633	.155	.195	.155	2.70	.34	2.40	1.20
"	.855	1.26	.335	.42	.335	3.10	.39	1.70	1.13
"	1.460	2.15	.540	.675	.560	3.55	.445	1.11	1.12
"	2.340	3.44	.745	.93	.890	3.60	.45	.87	1.11
10.00	.430	.324	.110	.11	.110	3.20	.32	4.20	1.16
"	.855	.644	.220	.22	.220	3.20	.32	2.94	1.11
"	1.460	1.10	.385	.385	.405	3.75	.375	2.08	1.09
13.00	.620	.212	.095	.073	.095	4.50	.345	7.15	1.11

h (cm.)	$\dot{M}$ dynes $x10^{-4}$	$\frac{\dot{M}}{\rho_L g h^3}$ $(x10^3)$	n_o (cm.)	$\frac{n_o}{h}$ (x10)	n_o+1	m (cm.)	$\frac{m}{h}$	R_o (cm.)	$1+\frac{2\sigma}{\rho_L g R_o n_o}$
13.00	.865	.296	.135	.105	.135	4.70	.36	7.15	1.08
"	1.120	.384	.185	.14	.185	4.90	.375	4.28	1.09
"	1.475	.505	.235	.18	.235	4.80	.37	4.17	1.07
"	2.360	.808	.370	.285	.390	4.90	.375	3.43	1.06
"	3.610	1.23	.570	.44	.680	5.25	.405	2.40	1.05
16.00	.865	.159	.075	.047	.075	5.10	.32	13.5	1.07
"	1.470	.270	.130	.081	.130	5.15	.32	6.46	1.09
"	2.360	.434	.230	.145	.230	5.90	.37	5.25	1.06

b). AIR - Mercury $\rho_L = 13.56 g.cm^{-3}$ $\sigma = 487$ dynes.cm^{-1} d = .253cm.

2.00	.245	23.0	.645	3.23	.665	1.25	.625	.25	1.45
"	.375	35.3	.740	3.70	.860	1.75	.825	.25	1.40
3.00	.245	6.83	.395	1.32	.405	1.40	.465	.49	1.38
5.00	.375	2.26	.300	.60	.300	2.10	.42	.92	1.27
13.00	1.030	.353	.125	.096	.125	4.95	.38	9.10	1.06
"	1.735	.595	.230	.175	.230	5.10	.39	5.25	1.06
"	3.320	1.14	.485	.375	.585	5.50	.425	2.41	1.06
16.00	1.035	.190	.095	.059	.095	5.70	.355	9.80	1.08

Appendix II

MEASUREMENTS ON RATES OF MASS TRANSFER OF CO_2 TO TAP WATER.

FIGURE A.2-1 shows calibration curve for variation of pH with CO_2 concentration and temperature 16-22°C

FIGURES A.2-2 - A.2-11 show dependence of $\ln\left(\frac{C^i - C^b_t}{C^i - C^b_{t=o}}\right)$ on time t, for variation in h, $\dot{M}$, A and V.

Table A.2-1 shows mass transfer coefficients $(k_L)_{mean}$, calculated from the slope of the curves in Figures A.2-2 to A.2-9, as per Equation 4.8-2, for an interface area A equal to 4185 cm^2, with h and $\dot{M}$ varying.

Table A.2-2 shows the variation of mass transfer coefficients $(k_L)_{mean}$ with interface area A, for values of h and $\dot{M}$.

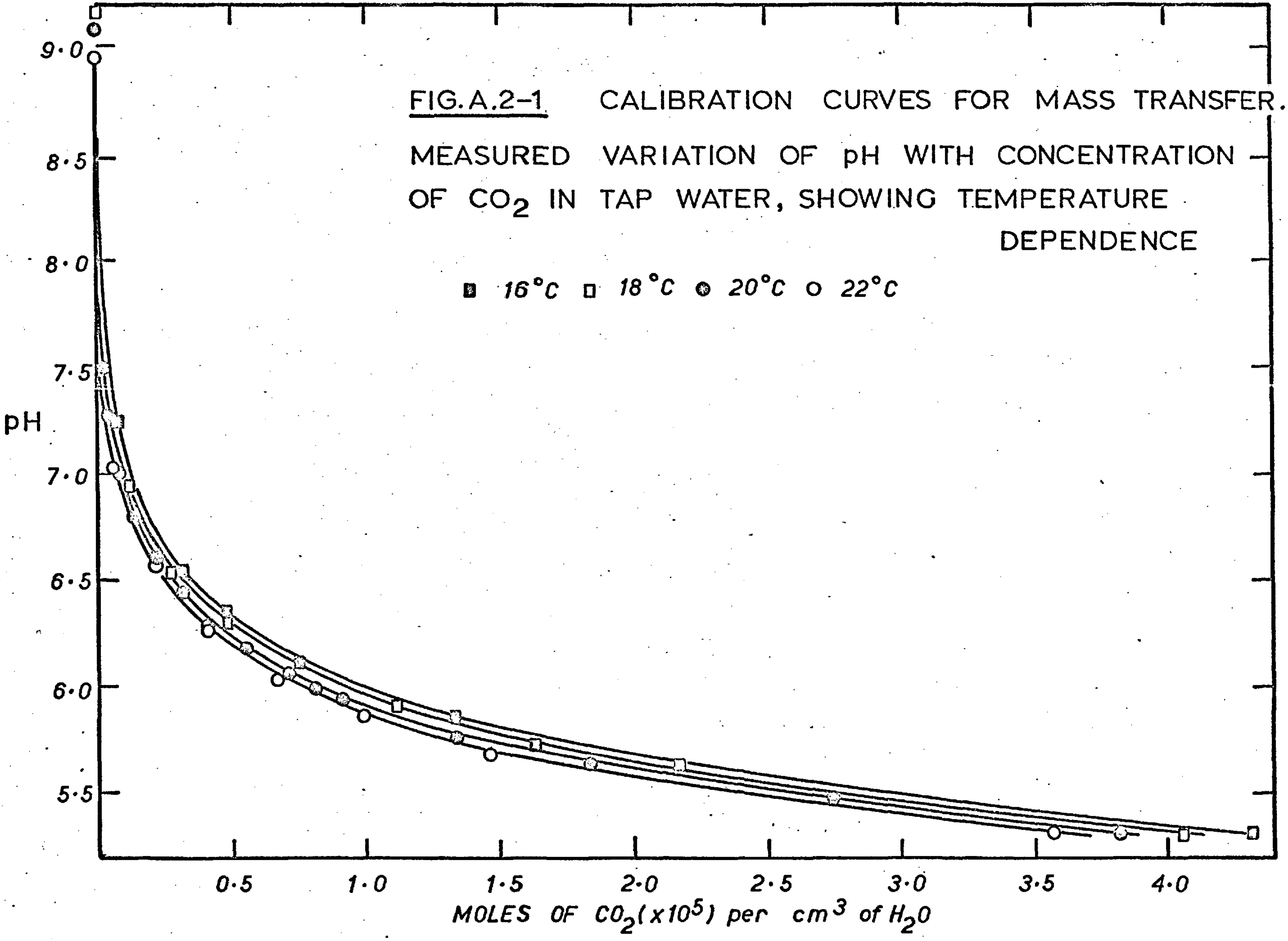

FIG. A.2-1 CALIBRATION CURVES FOR MASS TRANSFER. MEASURED VARIATION OF pH WITH CONCENTRATION OF CO_2 IN TAP WATER, SHOWING TEMPERATURE DEPENDENCE

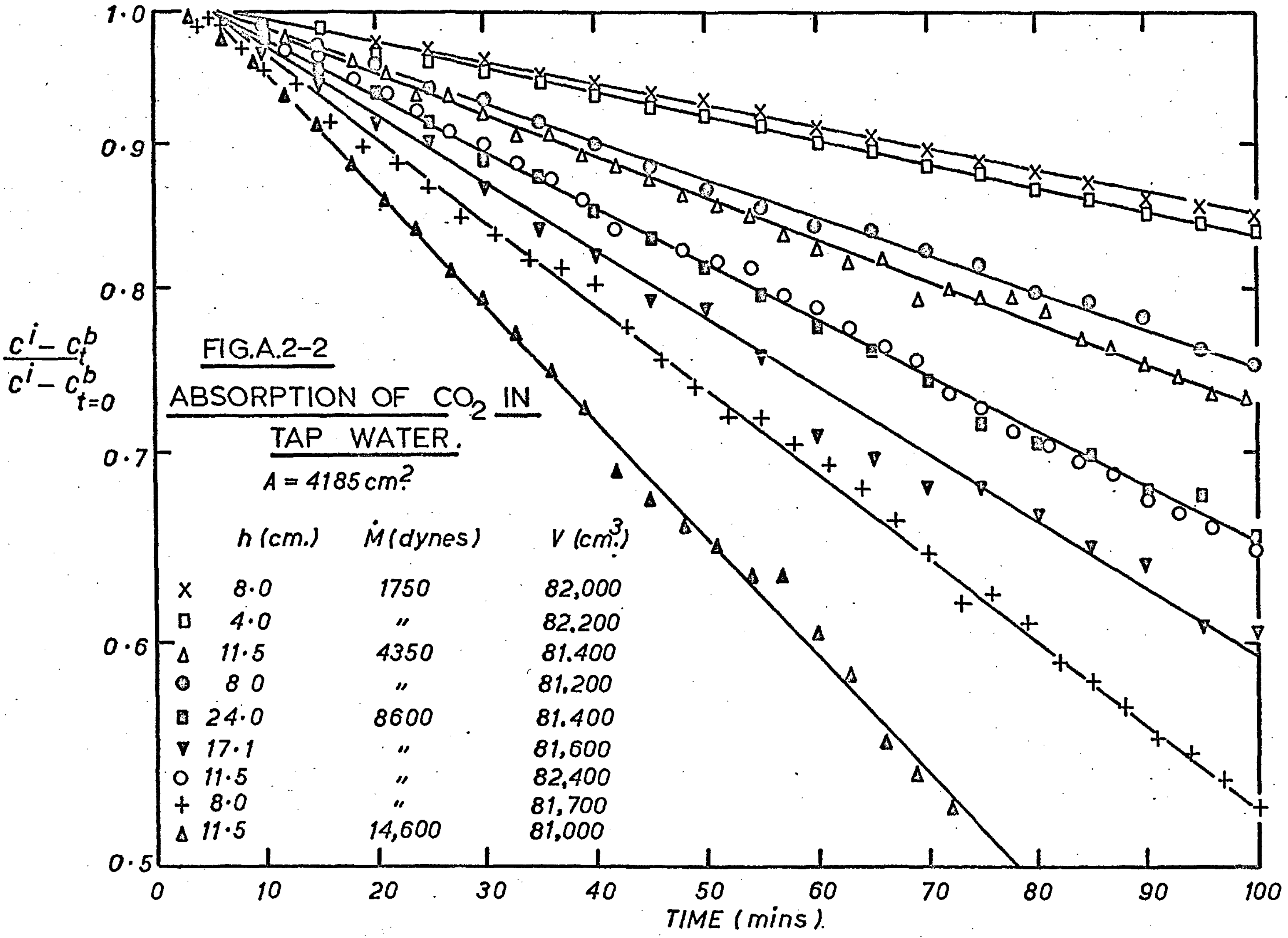

FIG.A.2-2

ABSORPTION OF CO_2 IN TAP WATER.

$A = 4185\ cm^2$

	h (cm.)	$\dot{M}$ (dynes)	V (cm^3)
×	8·0	1750	82,000
□	4·0	"	82,200
△	11·5	4350	81,400
◍	8 0	"	81,200
▣	24·0	8600	81,400
▼	17·1	"	81,600
○	11·5	"	82,400
+	8·0	"	81,700
▲	11·5	14,600	81,000

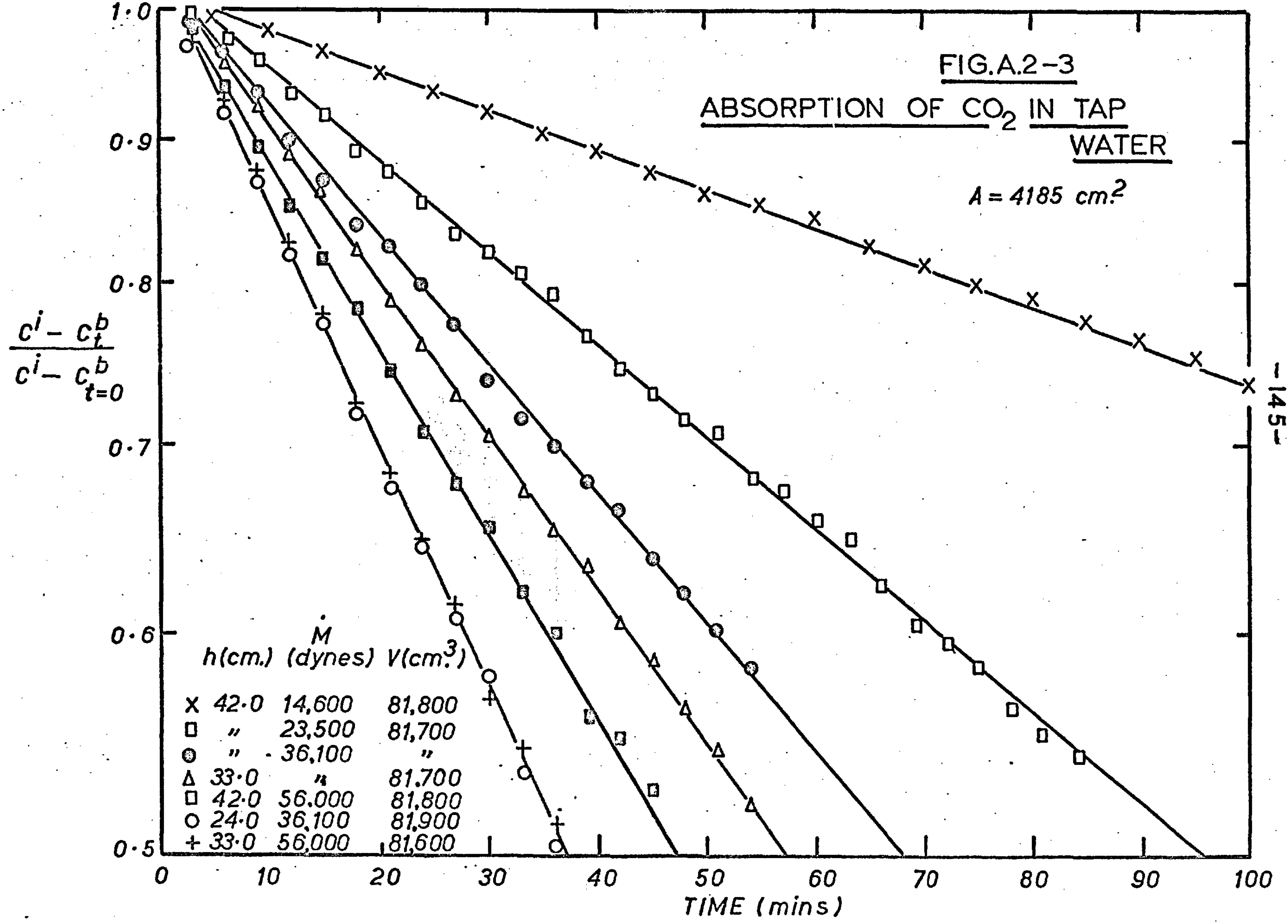

FIG.A.2-3

ABSORPTION OF CO_2 IN TAP WATER

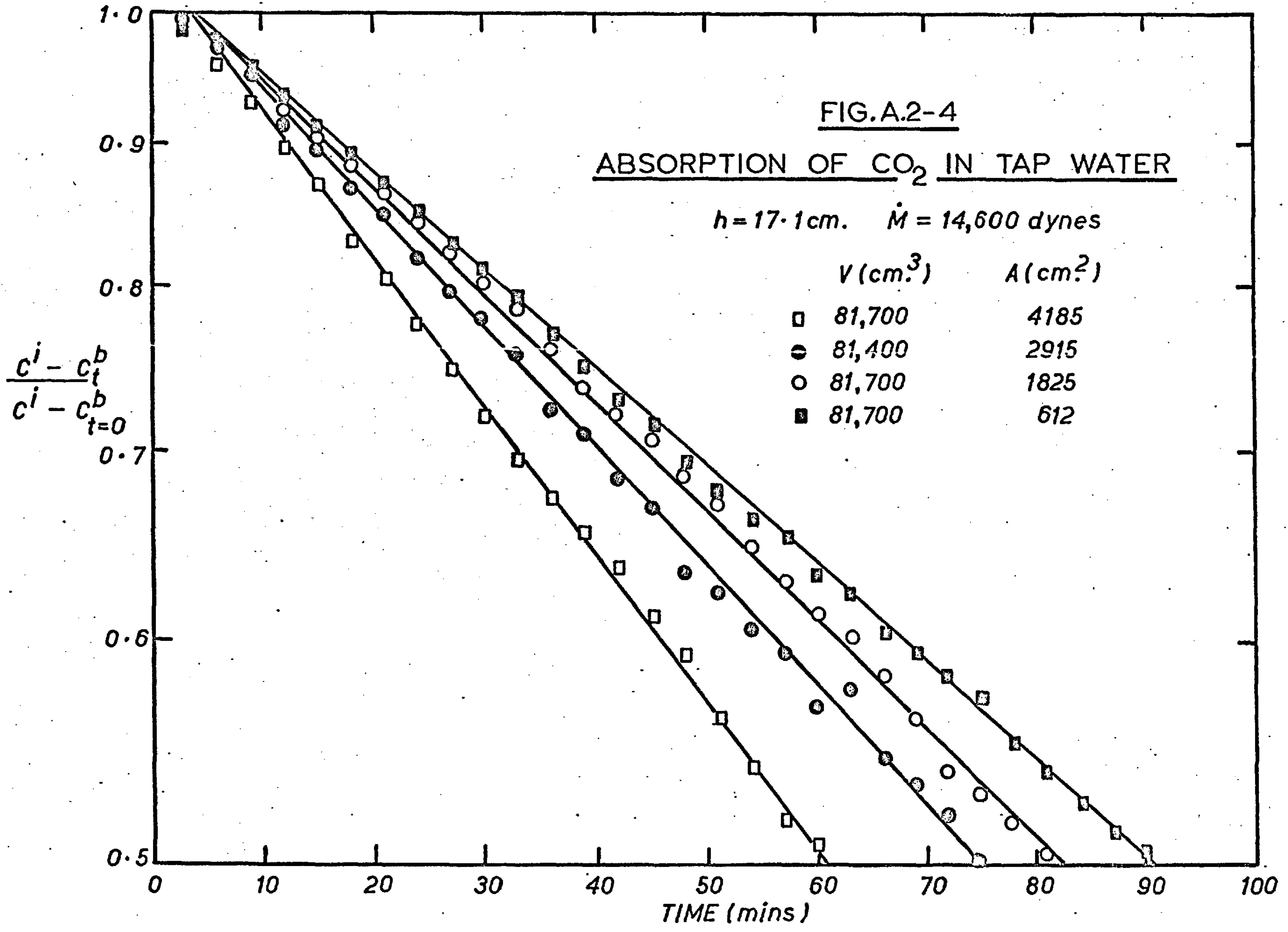

FIG. A.2-4

ABSORPTION OF CO_2 IN TAP WATER

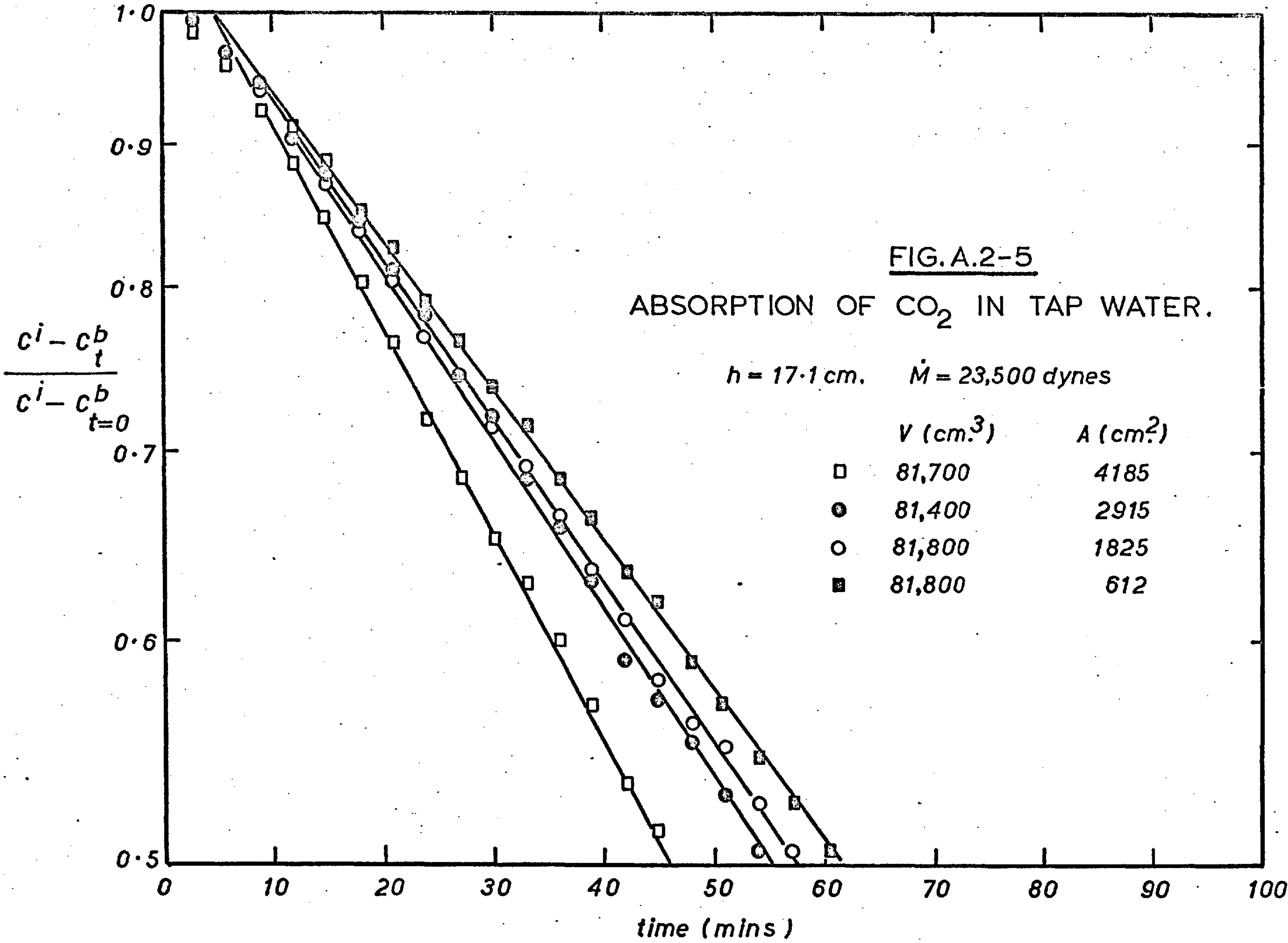

FIG. A.2-5

ABSORPTION OF CO_2 IN TAP WATER.

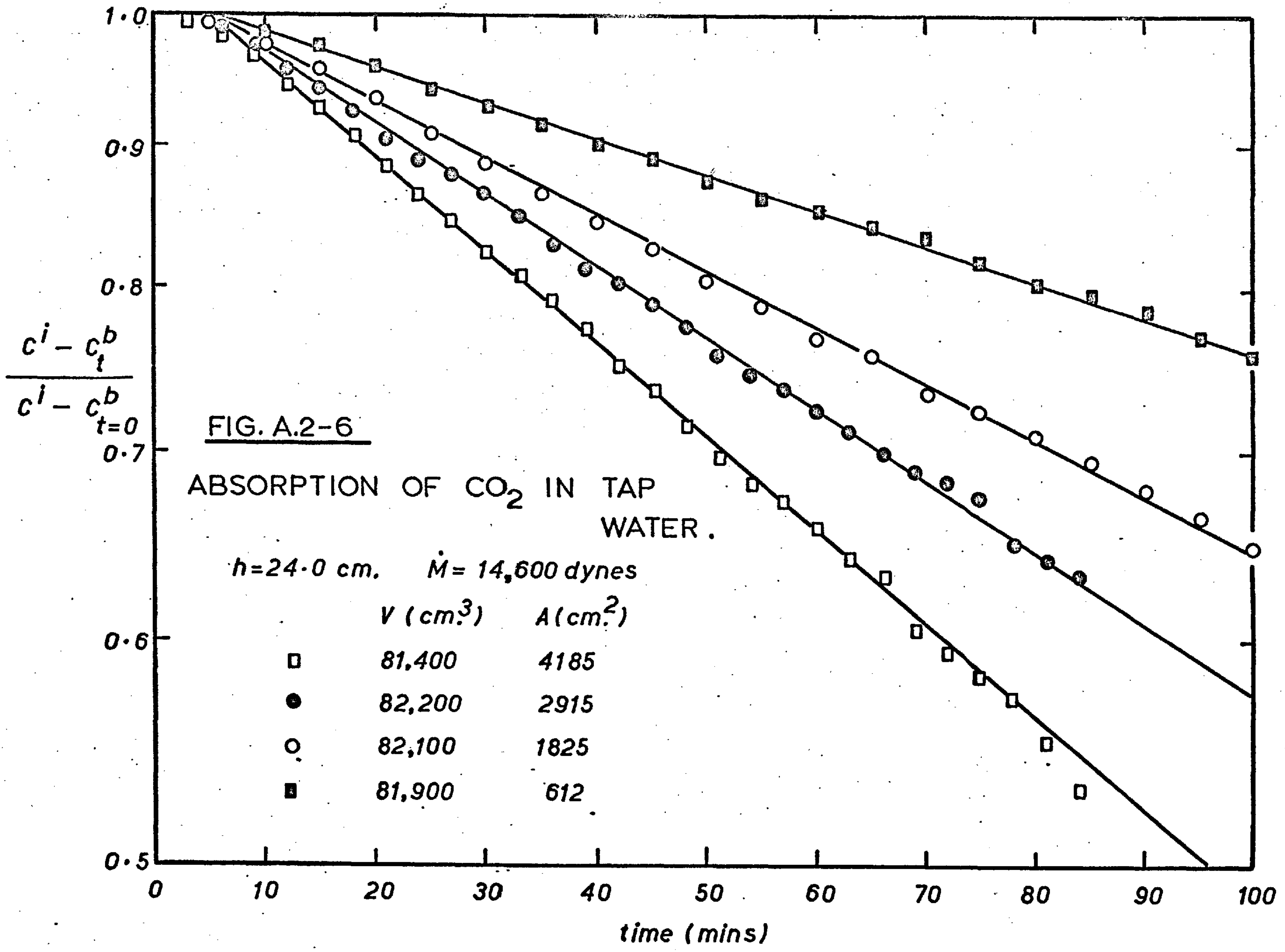

FIG. A.2-6

ABSORPTION OF CO_2 IN TAP WATER.

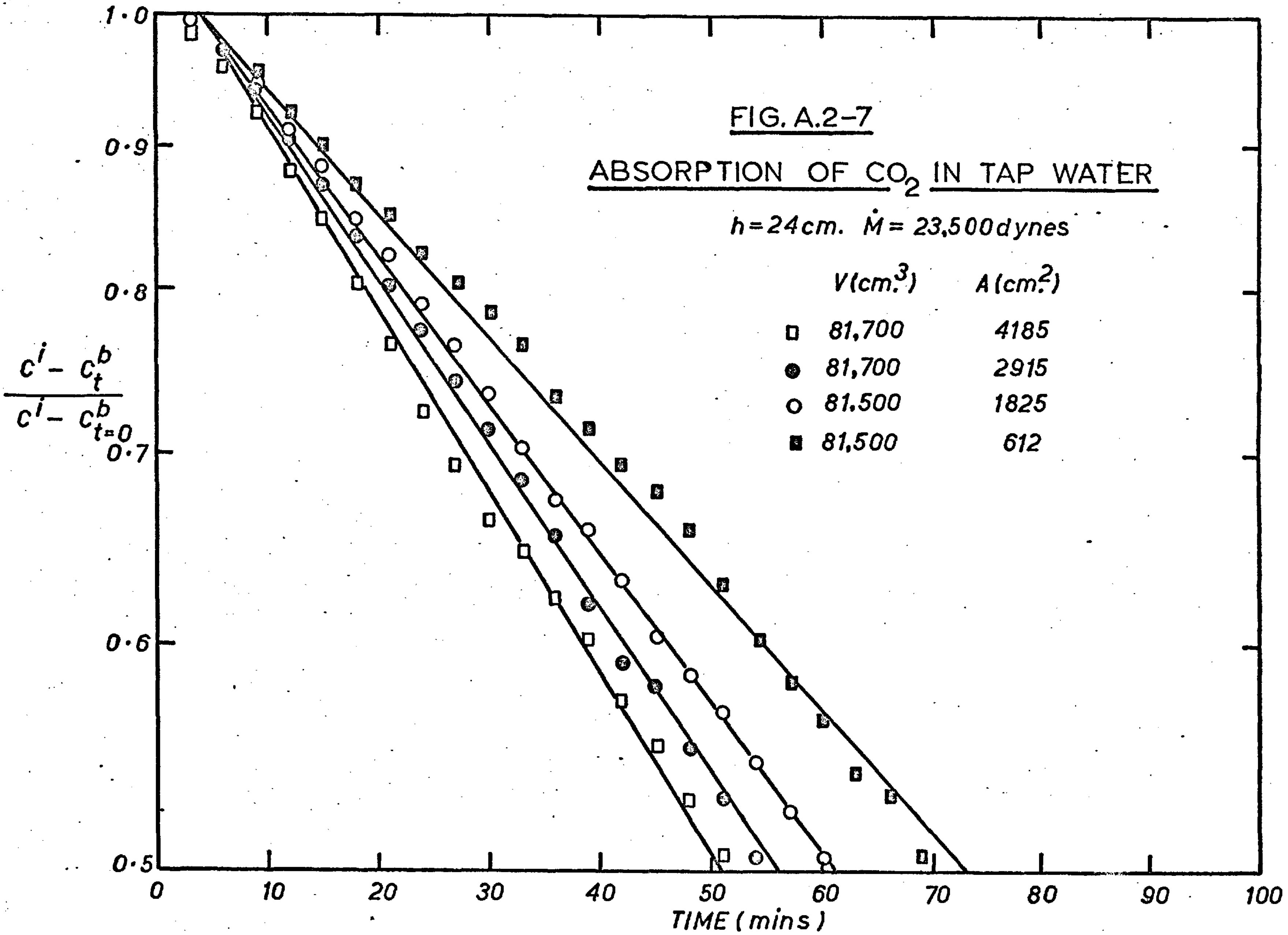

FIG. A.2-7

ABSORPTION OF CO_2 IN TAP WATER

$h = 24 \text{ cm.} \quad \dot{M} = 23{,}500 \text{ dynes}$

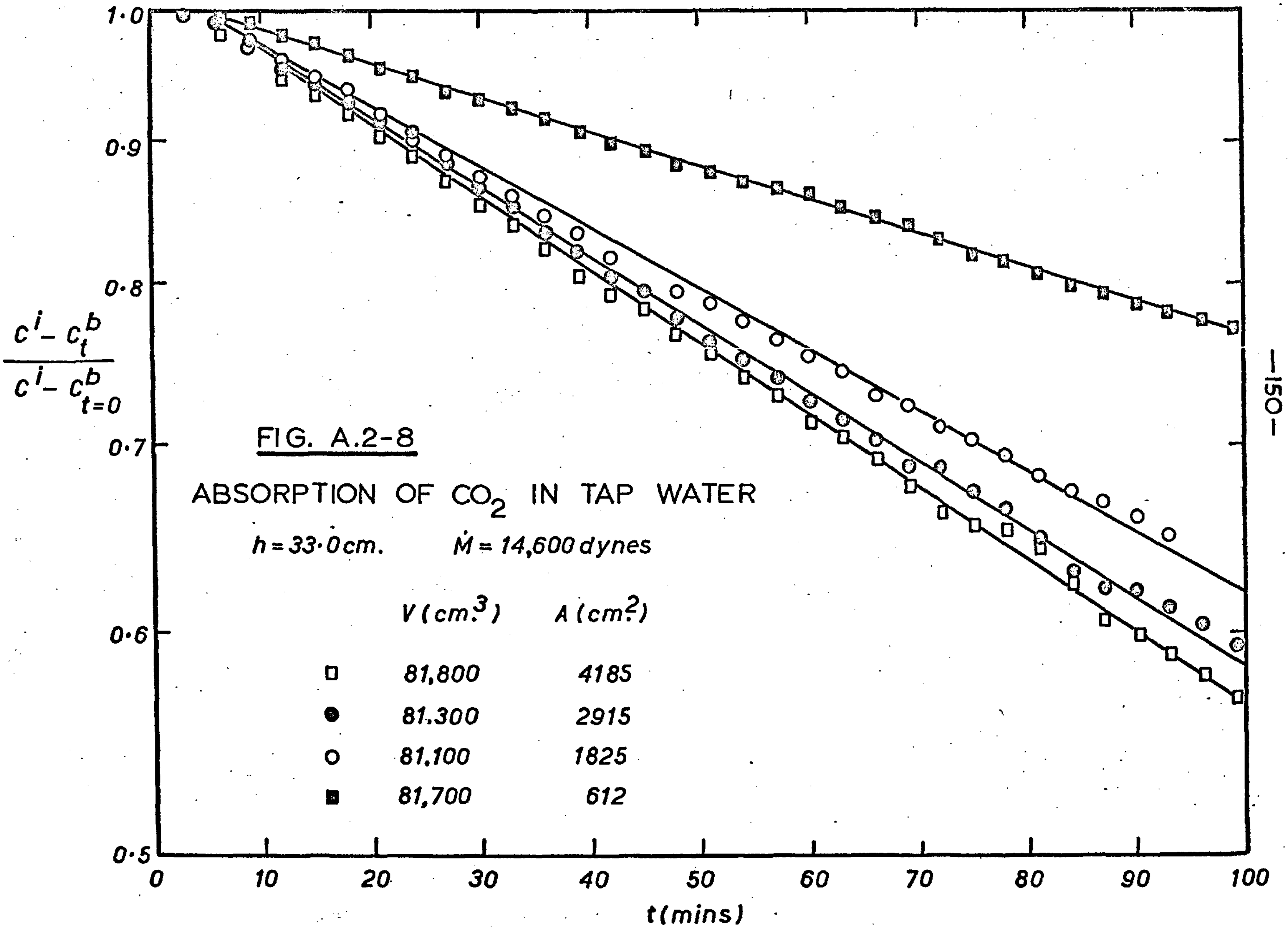

FIG. A.2-8

ABSORPTION OF CO_2 IN TAP WATER

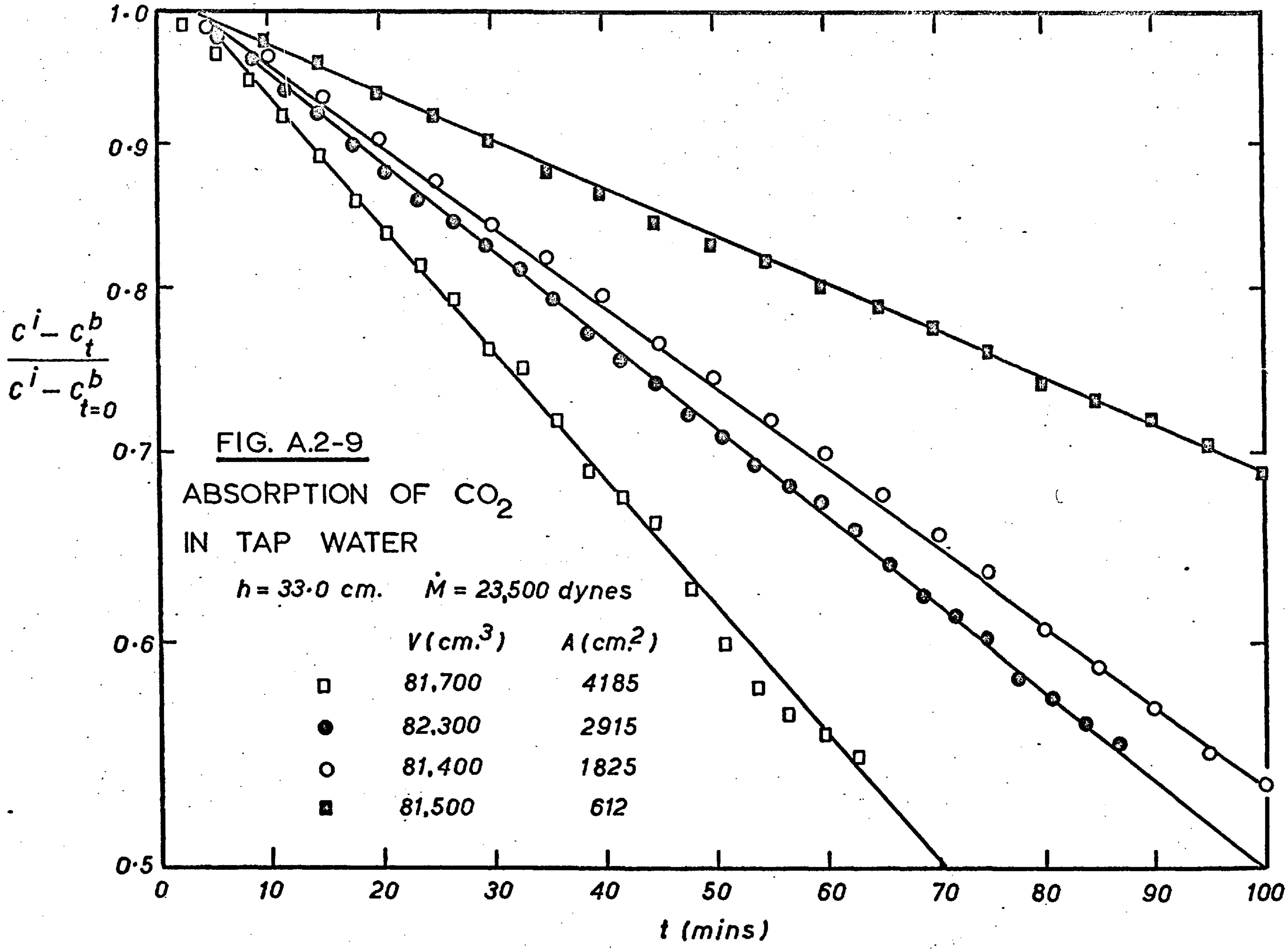

FIG. A.2-9

ABSORPTION OF CO_2 IN TAP WATER

$h = 33\cdot0$ cm. $\dot{M} = 23{,}500$ dynes

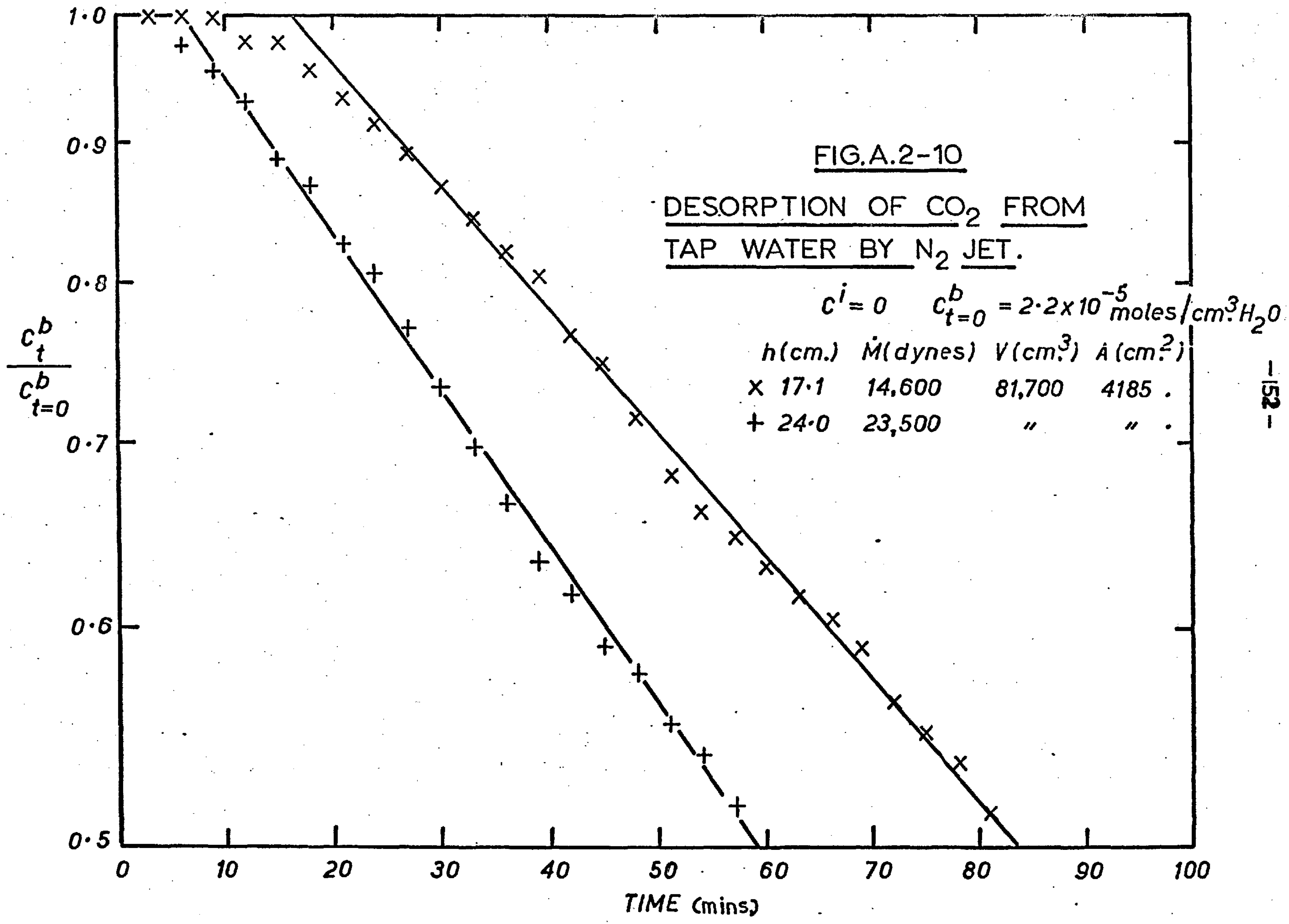

FIG. A.2-10

DESORPTION OF CO_2 FROM TAP WATER BY N_2 JET.

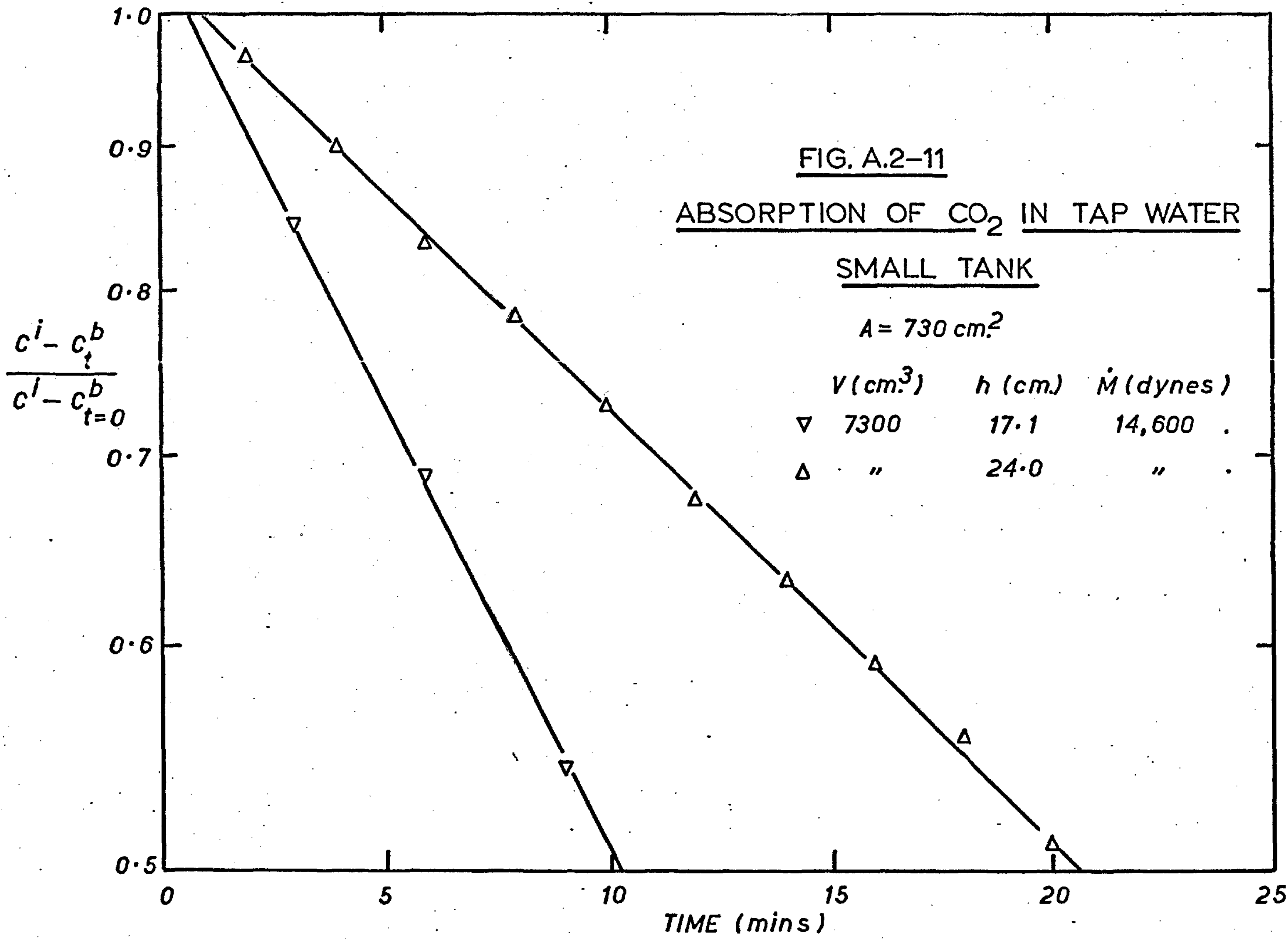

FIG. A.2–11

ABSORPTION OF CO_2 IN TAP WATER

SMALL TANK

Table A.2-1

A = 4185 cm^2

h (cm)	$\dot{M}$(dynes) x10^{-4}	V (cm^3) x10^{-4}	$(k_L)_{mean} \cdot A$ (cm^3/sec)	$(k_L)_{mean}$ (cm/secx10^3)
4.0	0.175	8.22	2.64	0.63
8.0	"	8.20	2.42	0.58
"	0.435	8.12	4.14	0.99
"	0.860	8.17	9.29	2.2
11.5	0.435	8.14	4.58	1.1
"	0.860	8.24	6.21	1.5
"	1.460	8.10	12.8	3.1
17.1	0.860	8.16	7.47	1.8
"	1.460	8.17	16.3	3.9
"	2.350	"	22.7	5.4
24.0	0.860	8.14	6.14	1.8
"	1.460	"	10.4	2.5
"	2.350	8.17	20.1	4.8
"	3.610	8.19	27.0	6.5
33.0	1.460	8.18	8.2	2.0
"	2.350	8.17	14.2	3.4
"	3.610	"	17.5	4.2
"	5.600	8.16	26.9	6.5
42.0	1.460	8.18	4.4	1.1
"	2.350	8.17	10.2	2.5
"	3.610	"	14.5	3.5
"	5.600	8.18	21.0	5.0

Table A.2-2

	h (cm)	$\dot{M}$(dynes) x10^{-4}	V (cm^3) x10^{-4}	A (cm^2)	$(k_L)_{mean}$ .A (cm^3/sec)	$(k_L)_{mean}$ (cm/secx10^3)
	17.1	1.460	8.17	4185	16.3	3.9
	"	"	8.14	2915	13.2	4.5
	"	"	8.17	1825	11.9	6.5
	"	"	"	612	10.8	17.6
D	"	"	"	4185	13.9	3.3
S	"	"	.73	730	8.9	12.2
	17.1	2.350	8.17	4185	22.7	5.4
	"	"	8.14	2915	18.6	6.4
	"	"	8.18	1825	17.8	9.8
	"	"	"	612	16.6	27.1
	24.0	1.460	8.14	4185	10.4	2.5
	"	"	8.22	2915	8.0	2.8
	"	"	8.21	1825	6.3	3.5
	"	"	8.19	612	4.0	6.5
S	"	"	.73	730	4.3	5.8
	24.0	2.350	8.17	4185	20.1	4.8
	"	"	"	2915	18.2	6.2
	"	"	8.15	1825	16.5	9.2
	"	"	"	612	13.7	22.3
D	"	"	8.17	4185	17.8	4.3

N.B. D refers to desorption, S to small tank (30.5cm.dia).

Table A.2-2(cont)

h (cm)	$\dot{M}$(dynes) $\times 10^{-4}$	V (cm^3) $\times 10^{-4}$	A (cm^2)	$(k_L)_{mean}$ .A (cm^3/sec)	$(k_L)_{mean}$ (cm/sec$\times 10^3$)
33.0	1.460	8.18	4185	8.2	2.0
"	"	8.13	2915	7.7	2.6
"	"	8.11	1825	6.8	3.7
"	"	8.17	612	3.6	6.0
33.0	2.350	8.17	4185	14.2	3.4
"	"	8.23	2915	10.0	3.4
"	"	8.14	1825	8.9	4.9
"	"	8.15	612	5.3	8.6

APPENDIX III

MEASUREMENTS ON RATES OF MASS TRANSFER OF OXYGEN TO MOLTEN SILVER AT 1010°C. A NOTE ON THE USE OF ZIRCONIA CELL TO MEASURE OXYGEN PRESSURE IN MOLTEN SILVER IS INCLUDED.

FIGURES A.3-1 - A.3-4 show measured variations in oxygen pressure for variation in h, $\dot{M}$ and A.

Table A.3.1 shows the variation in measured mass transfer coefficient $(k_L)_{mean}$.

The Use of An Electrochemical meter to measure Oxygen pressures in Molten Silver.

Certain solid oxides mixtures conduct by an anion vacancy mechanism [63,64], and can be used as an electrolyte in a cell of the form:

$$O_2\ (p_1)\ /\ \text{oxide}\ /\ O_2\ (p_2)$$

Lime-stabilised or magnesia-stabilised zirconia is such a mixture, and the latter has been used to measure oxygen pressures in hot gases[65], using platinum contacts to the cell.

The emf of the cell is given by

$$E = \frac{2.303\ R.T}{4F} \quad \log \quad (p_1/p_2)$$

where R is the gas constant, F is the Faraday constant and T the absolute temperature.

A lime-stabilised electrolyte has been used to verify that oxygen dissolution in silver obeys Sieverts Law[58], using stainless steel contacts to silver on either side of the electrolyte. In the present work, a similar cell was used with the reference oxygen pressure was maintained at one atmosphere, and the emf of the cell was given by

$$E = .0496\ .T.\ \log\ (p_{o_2})\ \text{millivolts.}$$

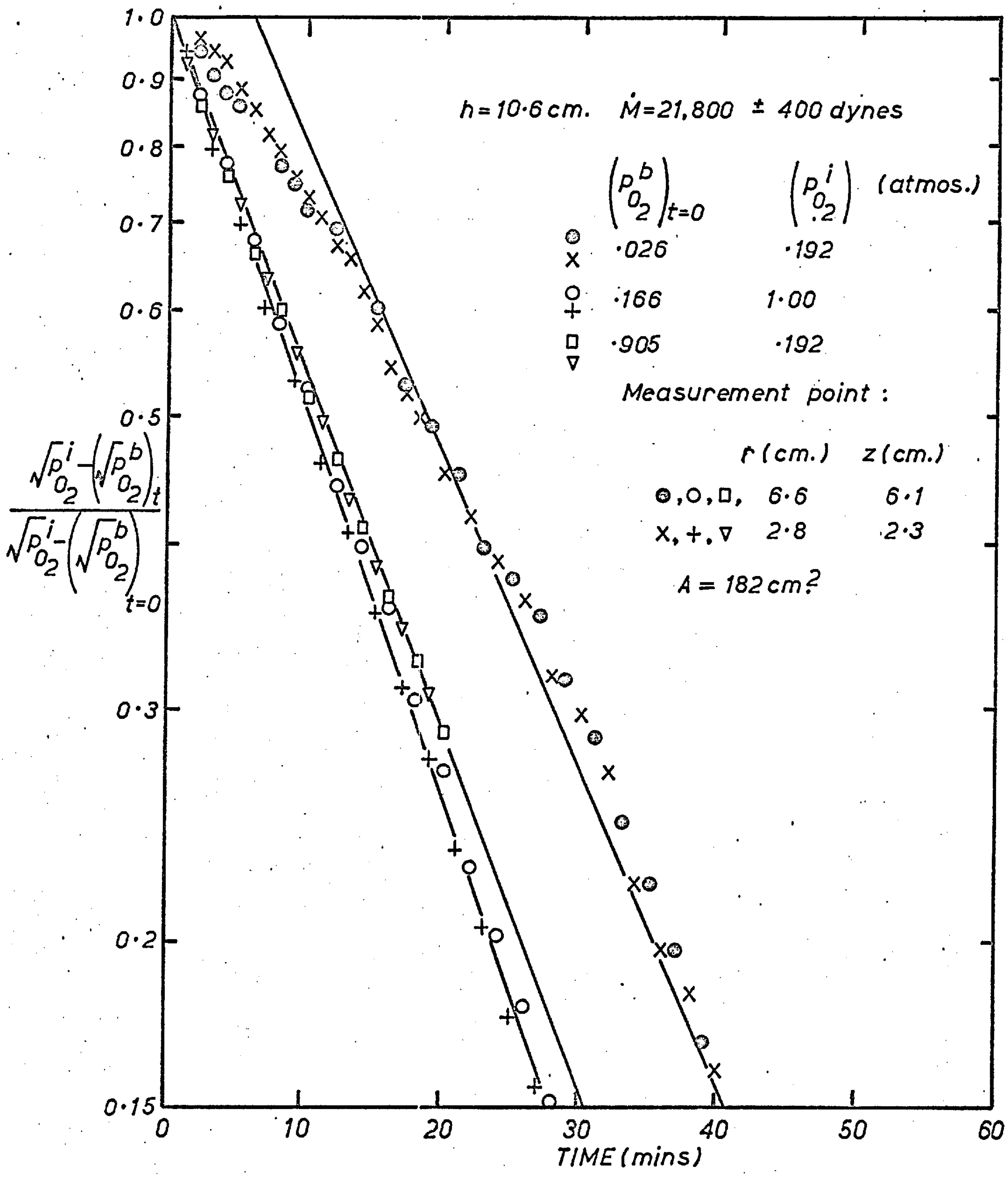

FIG.A.3-1 ABSORPTION AND DESORPTION RATES OF OXYGEN IN SILVER (1005°C)

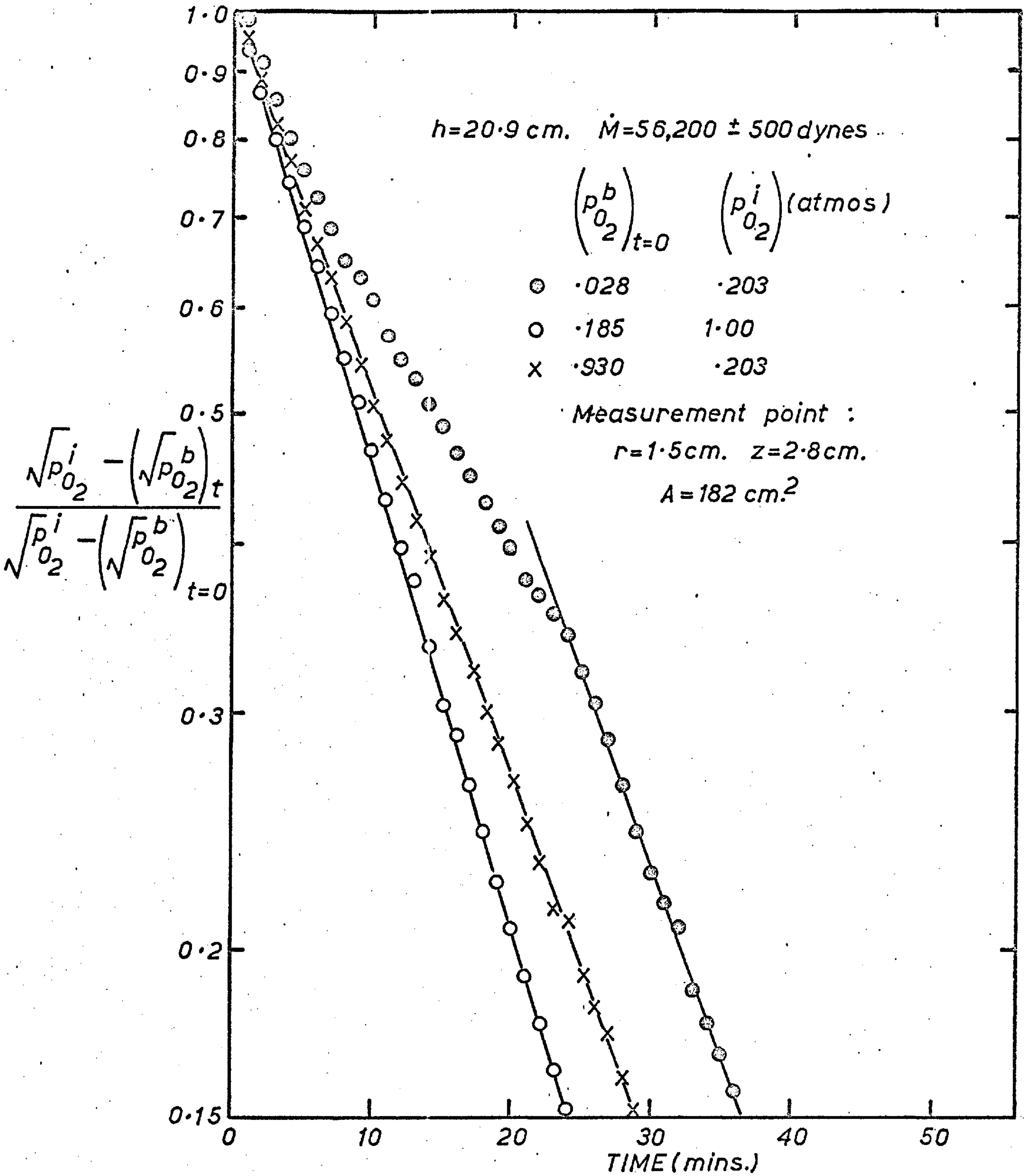

FIG.A.3-2 ABSORPTION AND DESORPTION RATES OF OXYGEN IN SILVER (1005°C)

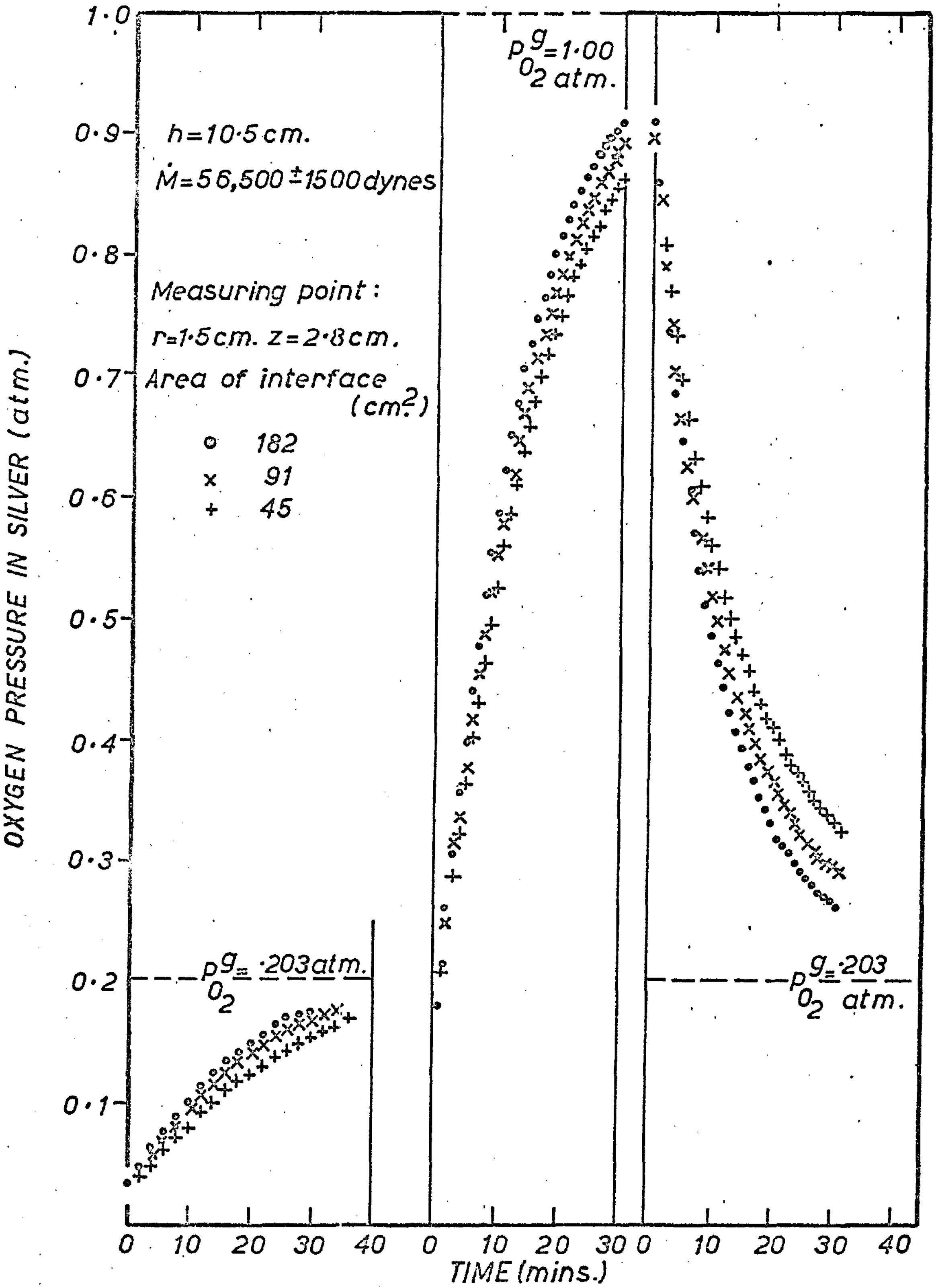

FIG.A.3-3 OXYGEN TRANSFER TO SILVER SHOWING VARIATION IN RATE OF TRANSFER WITH INTERFACE AREA.

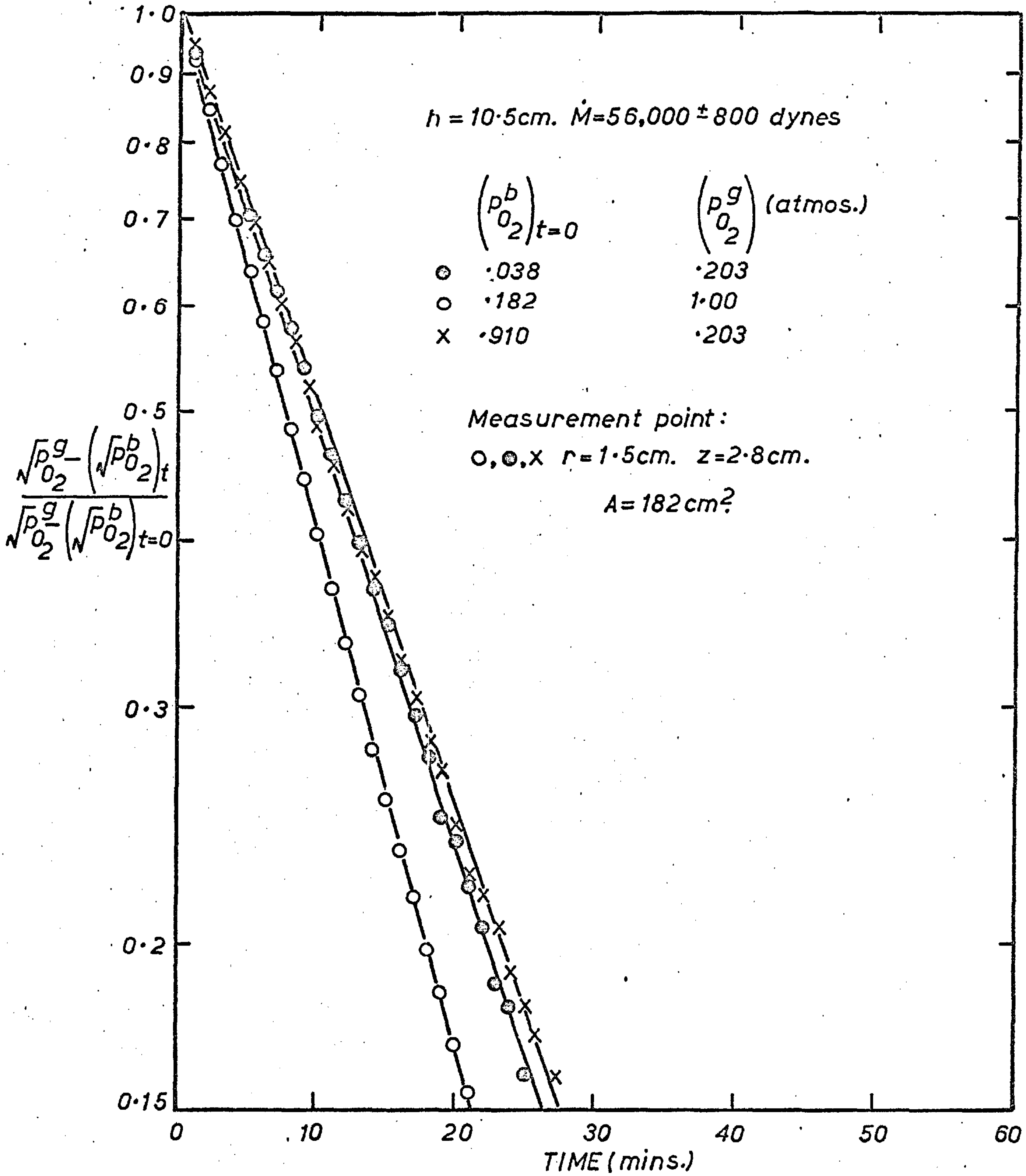

FIG.A.3-4a MASS TRANSFER OF OXYGEN TO SILVER BULK (1005°C.)

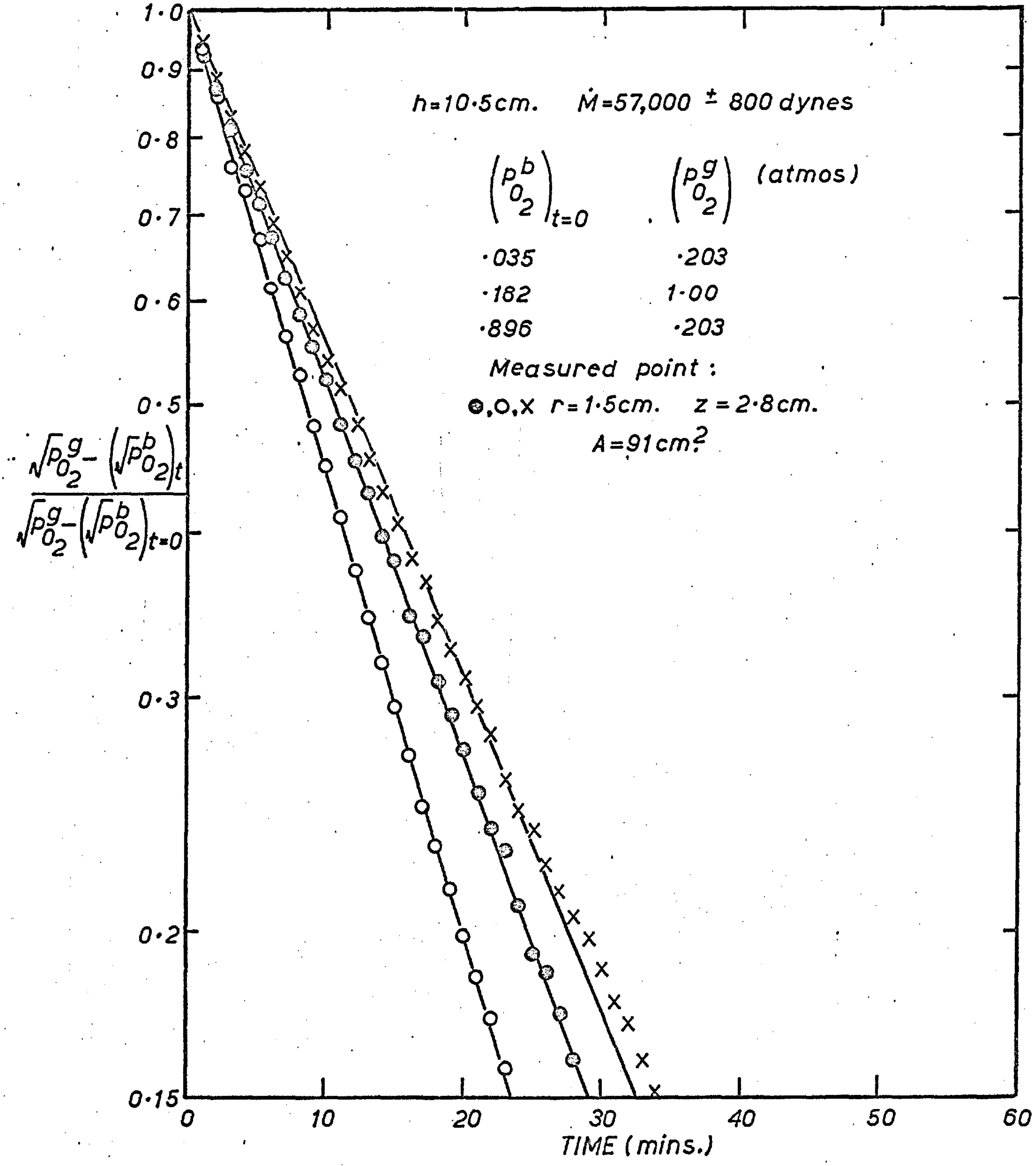

FIG.A.3-4b MASS TRANSFER OF OXYGEN TO SILVER BULK (1008°C.)

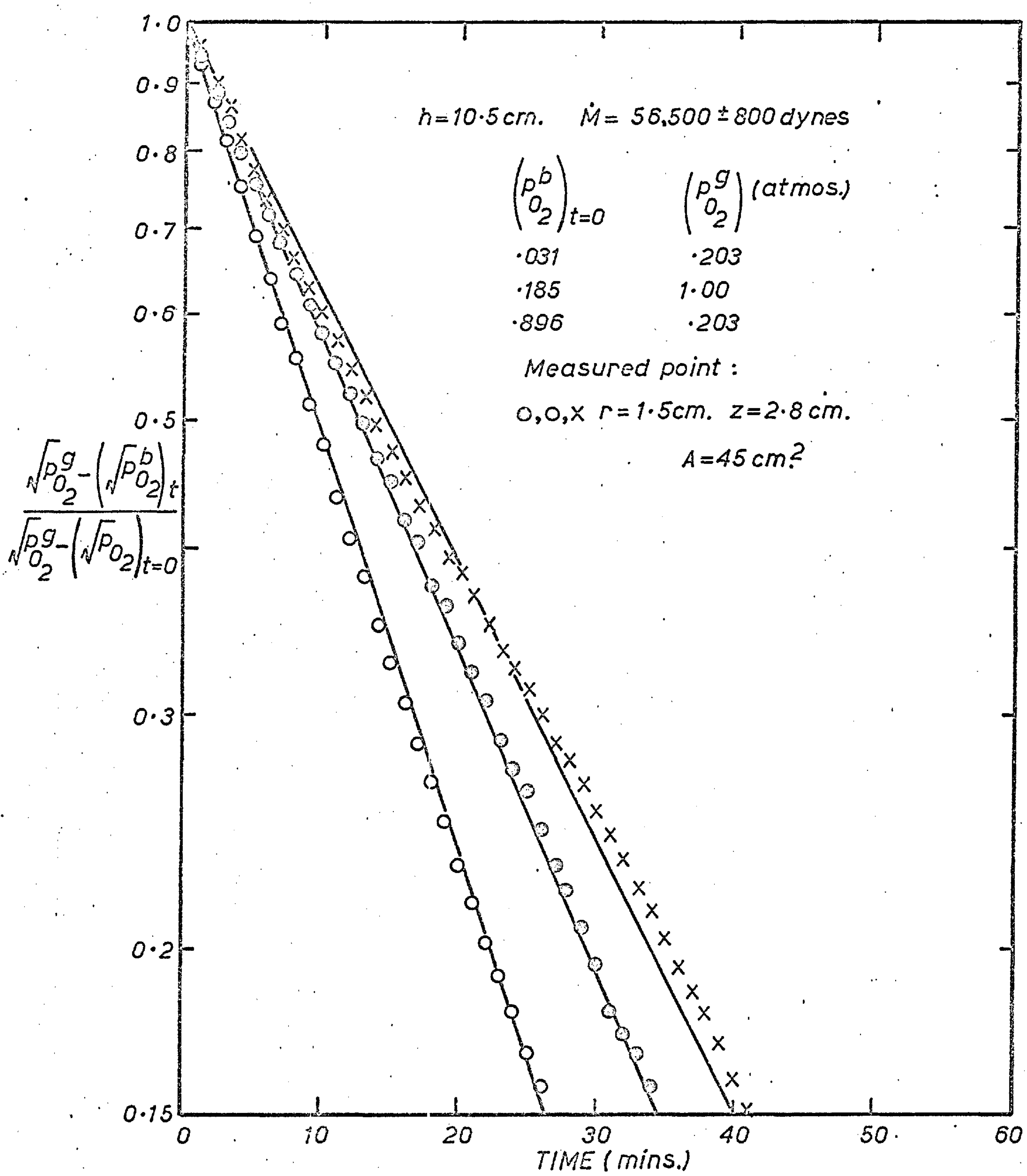

FIG.A.3-4c MASS TRANSFER OF OXYGEN TO SILVER BULK (1010°C)

Table A.3 - 1

$V = 1840\ cm^3$

h (cm)	$\dot{M}$(dynes) $\times 10^{-4}$	A (cm^2)	$P^g_{O_2}$ (atm)	$(k_L)_{mean}$ A (cm^3/sec)	$(k_L)_{mean}$ (cm/sec$\times 10^3$)
10.6	2.18	182	.192	1.67	9.2
"	"	"	1.00	2.05	11.3
"	"	"	.192	1.91	10.5
20.9	5.62	182	.203	1.99	10.9
"	"	"	1.00	2.42	13.3
"	"	"	.203	2.01	11.0
10.5	5.60	182	.203	2.15	11.8
"	"	"	1.00	2.66	14.6
"	"	"	.203	2.10	11.5
"	5.70	91	.203	1.95	21.4
"	"	"	1.00	2.40	26.4
"	"	"	.203	1.74	19.1
"	5.65	45	.203	1.62	36.0
"	"	"	1.00	2.13	47.4
"	"	"	.203	1.41	31.3

LIST OF SYMBOLS

a	distance of geometric origin of jet from nozzle plane (cm)
a_1, a_2	Lance cross-sectional area at planes 1 and 2 (cm^2) (Figure 1.1-1)
A	Plane area of still liquid interface (cm^2)
A_d	Projected area of depression on still liquid surface (cm^2)
C	Concentration (moles/cm^3)
C_a	Concentration of species "a" (moles/cm^3)
C_d	Coefficient of discharge of nozzle
d	Throat diameter of nozzle (cm)
D	Diffusion coefficient (cm^2/sec)
h	Nozzle - water distance (cm)
k_L	Liquid side mass transfer coefficient (cm/sec)
K	Jet constant of velocity decay
l	Lip height (cm)
m	Diameter of depression across lip (cm)
m^*	" " " at free liquid surface (cm)
$\dot{M}$	Jet momentum (dynes)
$\dot{m}$	Mass flow in jet (g./sec)
m_e	Partition coefficient at the interface
n	Depth of depression at radius r (cm)
n_c	" " at commencement of splashing (cm)
n_o	" " at $r = 0$ (cm)

$\dot{n}_a$	Rate of transfer of species "a" across interface (moles/sec)
p_1, p_2	Gas pressure at planes 1 and 2 in nozzle (atmos)
q	Solubility, constant, concentration of dissolved species at one atmosphere pressure (moles/cm^3)
r	Radius from centreline of jet (cm)
R	Radius of tank (cm)
T	Temperature (^oK)
t	Time (secs)
u_r	Liquid velocity in r direction (cm/sec)
u_s	" " " " at surface (cm/sec)
V	Volume of liquid bulk (cm^3)
$V_{(r,x)}$	Velocity of jet at point (r,x) (cm/sec)
V_1	Upstream velocity of jet (cm/sec)
V_J	Exit velocity of jet (cm/sec)
V_o	Centre-line velocity of jet (cm/sec)
x	Distance from plane of nozzle (cm)
x'	" " geometric origin of jet (cm)
z	Depth below free liquid surface (cm)
Z	Total bath depth (cm)

Re

Subscripts & Superscripts

i	Interface
b	Bulk
L	Liquid phase
g	Gaseous phase
β	Jet constant for velocity profile
γ	Ratio of specific heats
σ	Surface tension (dynes/cm)
μ	Viscosity (poise or centipoise)
ρ	Density (g/cm^3)
ρ_1, ρ_2	Gas density at planes 1 and 2 of nozzle (g/cm^3)

REFERENCES

1. F.D. Richardson, Iron and Coal Trades Review, 1961, 183, 1105-1116.
2. D.G. Howden and D.R. Milner, British Welding Journal, 1963, 10 (8), 395-398.
3. L.S. Darken and R.W. Gurry, Phys. Chem. of Metals, 485-487, 1953, McGraw - Hill.
4. B.M. Larsen and L.O. Sordall, Phys. Chem. of Proc. Met. 5, AIME Met.Soc. Conf.,1961, 8,1141-79.
5. T. Kootz, J.I.S.I., 1960, 196 (3), 253-259.
6. T. Kootz and H. Neuhaus, Stahl Eisen, 1961, 81 (26), 1810-15.
7. Kun Li, D.A. Dukelow and G.C. Smith, trans. Met. Soc. AIME, 1964, 230, 71-76.
8. G.C. Smith and D.A. Dukelow, J. of Metals, 1964, 16 (4), 352-361.
9. C. Holden and A. Hogg, J.I.S.I., 1960, 196 (3), 318-332
10. J. Szekely, Proc. of Joint Meeting A.I.Ch.E.- I.Ch.E., London,1965, Symposium No.2, 1-7.
11. B.S. Holmes and M.W. Thring, J.I.S.I., 1960, 196 (3),259-261.
12. H. Hasimoto, Tetsu - to - Hagane, 1958, 44 (3), 222-3.
13. H. Hasimoto and Y. Nagano, Tetsu - to - Hagane, 1958, 44 (3), 1055-56.
14. J. Maatsch, Techn. Mitt. Krupp. F.-B., 1963, 21 (1), 1-4.
15. V.I. Baptizmanskii, Izvest. Vuz-Chem. Met., 1962, 10, 31-41.
16. F. Mathieu, Rev. Univ. des Mines, 1962, 18 (7), 482-499.
17. J. Chedaille and M. Horvais, Centre Doc. Sid. Circ. Inf. Techn., 1962, 19 (2), 361-366.
18. R.B. Banks and D.V. Chandrasekhara, J. of F.Mech., 1963, 15, 13-34.

19. Kun Li, J.I.S.I., 1960, 196 (3), 275-280.

20. K.H. Kluth and J. Maatsch, Techn. Mitt. Krupp F.B., 1964, 22 (3), 1-8.

21. J.M. van Langen, J.I.S.I., 1960, 196 (3), 262-264.

22. E. Dubrawka, Open Hearth Proc., 1961, 44, 388-390.

23. G. Hoyle, J.I.S.I., 1962, 200, 605-610.

24. M.L. Albertson et al., 1950, Trans. Amer. Soc. Civ. Engrs., 115, 639-664.

25. S. Corrsin and M.S. Uberoi, 1949, N.A.C.A., TN No. 1865.

26. M. Poreh and J.E. Cermak, Proc. Sixth Midwest Con . Fluid Mech., 1959, 198-213.

27. D. Citrini, 1950, Trans. Amer. Soc. Civ. Engrs., 115, 674.

28. J.O. Hinze, Turbulence, 1959, McGraw-Hill.

29. W.D. Baines, 1950, Trans. Amer. Soc. Civ. Engrs., 115, 677.

30. F.P. Ricou and D.B. Spalding, J. Fluid Mech., 1961, 2, 21-32.

31. C.H. Bosanquet, G. Horn and M.W. Thring, Proc. Roy. Soc., 1961, A263 (1314), 340-352.

32. G. Abraham, Publication No.29, 1963, Delft Hydraulics Lab.

33. J. Maatsch, Tech. Mitt. Krupp, 1961, 19 (1), 17-31.

34. P. Bradshaw and E.M. Love, Aeronautical Research Council, 1959, R.& M. No. 3205.

35. G.C. Huang, J. of Heat Transfer, 1962, Paper No. 62 HT-31, 1-7.

36. K. Sagawa, S. Maehara, M. Shimada and M. Ishibashi, Tetsu-to-Hagane, 1958, 44 (9), 1056-58.

37. F. Mathieu, Rev. Univ. des Mines, 1960, 16 (7), 309-321.

38. R.D. Collins and H. Lubanska, Brit. J. of Applied Physics, 1954, 5, 22-26.

39. J. Maatsch, Techn. Mitt. Krupp F.-B., 1962, 20 (1), 1-9.

40. E. Denis, Rev. Univ. des Mines, 1963, 19 (9), 367-383.

41. T.W. van der Lingen, J.I.S.I., 1966, 204 (4), 320-325.

42. R.B. Banks and A. Bhavamai, J. Fluid Mech., 1965, 23, 229-240.

43. W.E. Olmstead and S. Raynor, J. Fluid Mech., 1964, 19, 561-576.

44. W.G. Davenport, Ph.D. Thesis Lond. Univ. 1964.

45. W.G. Whitman, Chem. and Met. Eng., 1923, 29, 146.

46. W.K. Lewis and W.G. Whitman, Ind. Eng. Chem., 1924, 16, 1215.

47. R. Higbie, Trans. Amer. Inst. Chem. Engrs., 1935, 31, 365.

48. P.V. Danckwerts, Ind. Eng. Chem., 1951, 43, 1460.

49. W.J. Beek and H. Kramers, Chem. Eng. Sc., 1962, 16, 909-921.

50. Thresh, Suckling and Beale, Examination of waters and water supply, 1949, Churchill.

51. J.F. Davidson & E.J. Cullen, trans. Inst. Chem. Engrs., 1957, 35, 51.

52. C.D. Hodgman, Handbook of Chemistry and Physics, 1959, Chem. Rubber Pub. Co.

53. L.J. Kastner, T.J. Williams and R.A. Sowden, J. Mech. Eng. Sci., 1964, 6, 88-98.

54. G. Birkhoff and E.H. Zarantonello, Jets, Wakes, and Cavities, 1957, Academic Press.

55. D. Berg and A. Patterson, J. Am. Chem. Soc., 1953, 75, 5197-5200.

56. C.J. Smithells, Metals Reference Book, 1962, Butterworth.

57. E.A. Mizikar, R.E. Grace and N.A.D. Parlee, Trans. A.S.M, 1963, 56, 103.

58. C. Diaz, C.R. Masson and F.D. Richardson, to be published.

59. B.C.H. Steele, Private Communication.

60. A. Sieverts and J. Hagenacker, Z. physick Chem., 1909, 68, 115.

61. S.L. Bragg, J. Mech. Eng. Sci., 1960, 2 (1), 35-44.

62. J.S. Holdhusen, Trans. Amer. Soc. Civ. Engrs., 1950, 115, 665-671.

63. K. Kinkkola and C. Wagner, J. Electrochem. Soc., 1957, 104, 379.

64. H. Peters and H.H. Mobius, Z. Phys. Chem. (Leipzig), 1958, 209, 298.

65. R. Littlewood, Steel Times, 1964, Sept. 25, 423-424.

66. B. Rosenberg, David Taylor Model Basin Report No. 727, 1950.

67. W.L. Haberman and R.K. Morton, David Taylor Model Basin Report No. 802, 1953.